THE GIANT DIPOLE RESONANCE REGION OF ^{31}P POLARIZED AND UNPOLARIZED PROTON CAPTURE MEASUREMENTS

by

Christopher Paul Cameron

Department of Physics
Duke University

Date: _____

Approved:

_____
N. Russell Roberson, Supervisor

_____

_____

_____

_____

A dissertation submitted in partial fulfillment of the requirements for the degree of Doctor of Philosophy in the Department of Physics in the Graduate School of Arts and Sciences of Duke University

1977

ABSTRACT

(Physics)

THE GIANT DIPOLE RESONANCE REGION OF ^{31}P POLARIZED AND UNPOLARIZED PROTON CAPTURE MEASUREMENTS

by

Christopher Paul Cameron

Department of Physics
Duke University

Date: _____

Approved:

_____
N. Russell Roberson, Supervisor

_____

_____

_____

_____

An abstract of a dissertation submitted in partial fulfillment of the requirements for the degree of Doctor of Philosophy in the Department of Physics in the Graduate School of Arts and Sciences of Duke University

1977

THE GIANT DIPOLE RESONANCE REGION

OF ^{31}P

POLARIZED AND UNPOLARIZED PROTON CAPTURE MEASUREMENTS

by

Christopher Paul Cameron

The 90° excitation functions have been measured for the $^{30}Si(p,\gamma_0)^{31}P$ and $^{30}Si(p,\gamma_1)^{31}P$ reactions for incident proton energies from 5 to 28 MeV. The total strength of γ_0 integrated from 12 to 35 MeV excitation energy exhausts approximately 5.4% of the classical dipole sum rule. For γ_1, 7.5% of the sum rule is exhausted in the region from 10.8 to 33.8 MeV excitation energy. The results for the ground state excitation function are compared to the results of the previously measured $^{31}P(\gamma,n_0)^{30}P$ reaction, and the isospin splitting of the giant dipole resonance is discussed.

Angular distributions of cross section and analyzing power were measured at twelve energies in the region of the giant dipole resonance. Seven angles were measured within the range of 42° to 142°. The $^{30}Si(p,\gamma_0)^{31}P$ reaction was analyzed to extract transition matrix elements and cross sections for electric dipole (E1), magnetic dipole (M1), and electric quadrupole (E2) radiation. The results are compared with observa-

tions by inelastic scattering experiments of the isoscalar giant quadrupole resonance in this mass region. The $^{30}Si(p,\gamma_1)^{31}P$ reaction was also analyzed to obtain the transition matrix elements for E1 radiation.

The fore-aft asymmetry of the $^{30}Si(p,\gamma_1)^{31}P$ reaction was observed at 1 MeV intervals over the energy range of 17 to 27 MeV incident proton energy. The asymmetry measurements are observed to show strong interference effects near an excitation energy of 31 MeV, suggesting the presence of the isovector giant quadrupole resonance. The asymmetry and total cross section are analyzed to obtain the width and strength of the resonance.

ACKNOWLEDGEMENTS

I wish to express my appreciation to my advisor, Dr. N. R. Roberson, for his interest, encouragement, and support during my graduate career. I extend my gratitude to Dr. H. R. Weller for his advice and for his support of these experiments. I also wish to thank Dr. D. G. Rickel, Dr. D. R. Tilley, and Dr. E. A. Blue for their assistance in data collection.

I extend special thanks to Dr. R. D. Ledford for many helpful discussions as well as for his assistance in data collection. I also wish to thank Mr. R. C. McBroom for his spectrum analysis code and Mr. J. D. Turner for his excellent photographic work; I would also like to thank both of them for their aid in data collection. I wish to thank all who spent many hours in developing and maintaining the polarized ion source. I extend my appreciation to the technical staff for assistance with the accelerator and electronics systems. I especially wish to thank Mr. S. E. Edwards for his help with the computers. Special thanks are extended to Mrs. M. Bailey for her assistance and patience in preparing the illustrations. I am grateful to Dr. H. W. Newson and Dr. E. G. Bilpuch for providing me with the research assistantship.

A very special thanks is extended to my parents for their continuing encouragement and support.

This work was supported in part by the U. S. Energy Research and Development Administration.

C. P. C.

CONTENTS

ABSTRACT iii

ACKNOWLEDGEMENTS v

LIST OF FIGURES ix

LIST OF TABLES xi

I. INTRODUCTION 2

II. EXPERIMENTAL APPARATUS AND TECHNIQUES 5

A. Beam Parameters 5
B. Targets 7
C. Detectors 8
D. Electronics and Data Collection 12

III. DATA REDUCTION 22

A. Fitting and Stripping Procedures 22
B. Normalization to Monitor Detectors 26

IV. EXCITATION FUNCTIONS 27

A. The $^{30}Si(p,\gamma_0)^{31}P$ and $^{30}Si(p,\gamma_1)^{31}P$ Reactions 27

B. Structural Details of the Giant Dipole Resonance 30

C. Isospin Splitting of the Giant Dipole Resonance 36

V. ANGULAR DISTRIBUTIONS 43

A. Fits to Legendre Polynomials 43
B. Transition Matrix Analysis 72
C. Comparison to Sum Rules 119

VI. THE ISOVECTOR QUADRUPOLE RESONANCE 125

A. Theoretical Predictions and Historical Background 125

B. Analysis of Data 126

C. Results 130

VII. SUMMARY OF RESULTS AND CONCLUSIONS 134

APPENDIX A. Target Preparation 137

APPENDIX B. Giant Resonances in $^{55, 57, 59}$Co Using Polarized Proton Capture 141

LIST OF REFERENCES 152

LIST OF FIGURES

1. Schematic Diagram of the Gamma Ray Spectrometer 10

2. Block Diagram of Electronics 14

3. Typical Gamma Ray Spectrum for D. C. Beam 18

4. Typical Gamma Ray Spectrum for Pulsed Beam 20

5. Spectrum with Fitted Line Shape 24

6. Excitation Functions for $^{30}Si(p,\gamma_0)^{31}P$ and $^{30}Si(p,\gamma_1)^{31}P$ 29

7. Excitation Functions for $^{31}P(\gamma,p_0)^{30}Si$, $^{31}P(\gamma,n_0)^{30}P$, and $^{31}P(\gamma,n)^{30}P$ 32

8. Excitation Functions for $^{31}P(p,\gamma_0)^{32}S$, $^{27}Al(p,\gamma_0)^{28}Si$, and $^{30}Si(p,\gamma_0)^{31}P$ 35

9. $^{30}Si(p,\gamma_0)^{31}P$ Angular Distributions for Proton Energies 6.36, 7.46, 8.4, 8.81, 8.85, and 10.225 MeV 45

10. $^{30}Si(p,\gamma_0)^{31}P$ Angular Distributions for Proton Energies 11.01, 12.0, 12.85, 13.775, 14.625, and 14.95 MeV 47

11. $^{30}Si(p,\gamma_0)^{31}P$ Angular Distributions for Proton Energies 8.25, 8.55, 8.65, 8.925, and 12.8 MeV 49

12. The a_κ Coefficients Obtained from the Angular Distributions of the $^{30}Si(p,\gamma_0)^{31}P$ Reaction 52

13. The b_κ Coefficients Obtained from the Angular Distributions of the $^{30}Si(p,\gamma_0)^{31}P$ Reaction 57

14. The a_κ and b_κ Coefficients Obtained from the Angular Distributions of the $^{30}Si(p,\gamma_0)^{31}P$ and $^{31}P(p,\gamma_0)^{32}S$ Reactions 61

15. The Fore-aft Asymmetry and Total Cross Section Obtained from the $^{30}Si(p,\gamma_0)^{31}P$ Reaction 64

16. $^{30}Si(p,\gamma_1)^{31}P$ Angular Distributions for Proton Energies 8.25, 8.65, 10.225, 11.01, 12.0, and 12.8 MeV 69

17. $^{30}Si(p,\gamma_1)^{31}P$ Angular Distributions for Proton Energies 12.85, 13.775, 14.625, and 14.95 MeV 71

18. The a_κ and b_κ Coefficients Obtained from the Angular Distributions of the $^{30}Si(p,\gamma_1)^{31}P$ Reaction 74

19. The Fore-aft Asymmetry and Total Cross Section Obtained from the $^{30}Si(p,\gamma_1)^{31}P$ Reaction 78

20. The Solutions Obtained from an E1 Analysis of the $^{30}Si(p,\gamma_0)^{31}P$ Reaction 84

21. The Solutions Obtained from an E1 Analysis of the $^{30}Si(p,\gamma_1)^{31}P$ Reaction 90

22. The Solutions Obtained from an E1-E2 Analysis of the Third Order Fits to the Angular Distributions of the $^{30}Si(p,\gamma_0)^{31}P$ Reaction 96

23. The Solutions Obtained from an E1-E2 Analysis of the Fourth Order Fits to the Angular Distributions of the $^{30}Si(p,\gamma_0)^{31}P$ Reaction 100

24. The Solutions Obtained from an E1-E2 Analysis of the Fourth Order Fits, neglecting a_1 and b_1, to the Angular Distributions of the $^{30}Si(p,\gamma_0)^{31}P$ Reaction 105

25. The Solutions Obtained from an E1-E2-M1 Analysis of the Fourth Order Fits to the Angular Distributions of the $^{30}Si(p,\gamma_0)^{31}P$ Reaction 110

26. The E1-E2-M1 Cross Sections Obtained from a T-matrix Analysis of the $^{30}Si(p,\gamma_0)^{31}P$ Reaction 114

27. The Cross Section and Fore-Aft Asymmetry in the Region of the Isovector Giant Quadrupole Resonance of ^{31}P 132

LIST OF TABLES

I. The Integrated Yields of the Proposed Isospin Components of the Giant Dipole Resonance of ^{31}P 38

II. The a_k Coefficients Obtained from the Angular Distributions of the $^{30}Si(p,\gamma_0)^{31}P$ Reaction 53

III. The b_k Coefficients Obtained from the Angular Distributions of the $^{30}Si(p,\gamma_0)^{31}P$ Reaction 58

IV. The Fore-aft Asymmetry and Total Cross Section Obtained from the $^{30}Si(p,\gamma_0)^{31}P$ Reaction 65

V. The a_k Coefficients Obtained from the Angular Distributions of the $^{30}Si(p,\gamma_1)^{31}P$ Reaction 75

VI. The b_k Coefficients Obtained from the Angular Distributions of the $^{30}Si(p,\gamma_1)^{31}P$ Reaction 76

VII. The Fore-aft Asymmetry and Total Cross Section Obtained from the $^{30}Si(p,\gamma_1)^{31}P$ Reaction 79

VIII. The Solutions obtained from an E1 Analysis of the $^{30}Si(p,\gamma_0)^{31}P$ Reaction 85

IX. The Solutions Obtained from an E1-E2 Analysis of the Third Order Fits to the Angular Distributions of the $^{30}Si(p,\gamma_0)^{31}P$ Reaction 97

X. The Solutions Obtained from an E1-E2 Analysis of the Fourth Order Fits to the Angular Distributions of the $^{30}Si(p,\gamma_0)^{31}P$ Reaction 101

XI. The Solutions Obtained from an E1-E2 Analysis of the Fourth Order Fits, Neglecting a_1 and b_1, to the Angular Distributions of the $^{30}Si(p,\gamma_0)^{31}P$ Reaction 106

XII. The Solutions Obtained from an E1-E2-M1 Analysis of the Fourth Order Fits to the Angular Distributions of the $^{30}Si(p,\gamma_0)^{31}P$ Reaction 111

XIII. The E1-E2-M1 Cross Sections Obtained from a T-matrix Analysis of the $^{30}Si(p,\gamma_0)^{31}P$ Reaction 115

XIV. The Energy Integrated Cross Sections Compared with the Dipole Sum Rule 120

XV. The Integrated E2 Cross Section Compared with the Quadrupole Sum Rules 123

THE GIANT DIPOLE RESONANCE REGION

OF ^{31}P

POLARIZED AND UNPOLARIZED PROTON CAPTURE MEASUREMENTS

Chapter I

INTRODUCTION

The giant dipole resonance (GDR) appears as a broad maximum in the photon absorption cross section of nuclei. For the A=30 mass region, the resonance is observed to be centered near an excitation energy of $E_x = 63/A^{1/3}$ MeV (Hayward, 1970). The GDR has been studied by photonuclear reactions as well as radiative capture reactions and elastic and inelastic scattering. In the present work, the giant resonance region of ^{31}P has been studied via the $^{30}Si(p,\gamma)^{31}P$ reaction for incident proton energies from 5 to 28 MeV, which corresponds to an excitation energy of 12 to 35 MeV. The GDR of some nuclei in the A~30 mass region have been investigated in previous proton capture experiments; these nuclei include ^{28}Si (Singh et al., 1965) and ^{32}S (Dearnaley et al., 1965). Particular attention was paid in these experiments to the nature of the fine structure that is a feature of this mass region.

In recent years, there has been widespread interest in the isospin composition of the GDR, particularly in regard to the question of isospin splitting of the GDR. Only the T =1 component of the GDR of self-conjugate nuclei, such as ^{28}Si and

^{32}S, is allowed. These nuclei have been studied via the isospin forbidden reactions $^{24}Mg(\alpha,\gamma_0)^{28}Si$ and $^{28}Si(\alpha,\gamma_0)^{32}S$ (Meyer-Schutzmeister et al., 1968), as well as by the previously mentioned isospin allowed proton capture reactions. A comparison of the results of these experiments suggests the possibility of both isospin splitting and isospin mixing in these nuclei.

The giant resonance of ^{31}P may be composed of T=1/2 and T=3/2 components, both of which may be observed by proton emission. Decay by neutron emission to the ground state of ^{30}P, however, is only isospin allowed from the T=1/2 component. Gellie et al. (1973) have observed the $^{31}P(\gamma,p_0)^{30}P$ reaction and their data are compared in this work to the reaction $^{31}P(\gamma,p_0)^{30}Si$ as seen by proton capture. The results of the comparison tend to support the theory of isospin splitting.

Polarized proton capture has been shown to be a useful tool for not only studying the composition of the GDR (Glavish et al., 1972; Hanna et al., 1972) but also for measuring the E2 strength in the region of the GDR (Hanna et al., 1974; Weller et al., 1974). Measurements of the angular distributions of cross section and analyzing power are particularly valuable where, as in the present case, the spins of the target and residual nuclei are 0 and 1/2 (or 1/2 and 0); then, it is feasible to obtain the total E2 strength from a transition matrix analysis (Glavish, 1973; Weller et al., 1976). Bohr and Mottelson (1975) have predicted the existence of an isoscalar

giant quadrupole resonance (GQR) near $E_x = 58A^{1/3}$. In this mass region, the GQR has been reported near the predicted location by inelastic proton scattering in ^{27}Al (Lewis and Bertrand, 1972), and by inelastic alpha scattering on ^{32}S (Youngblood et al., 1976) and on $^{24,25,26}Mg$ and ^{27}Al (Kiss et al., 1976). Glavish et al. (1974) have also studied ^{32}S, using the $^{31}P(\vec{n},\gamma_0)^{32}S$ reaction. The results of their T-matrix analysis are compared with the results of the present work.

Additionally, the ambiguities which arise from the limited angular range of a large detector system and from the question of M1 strength in the energy region studied are considered in some detail. The T-matrix technique is also used to investigate the GQR built upon the first excited state of ^{31}P.

The giant quadrupole resonance is predicted to have an isovector component centered near $E_x = 135/A^{1/3}$ MeV in medium mass nuclei (Bohr and Mottelson, 1975). Such resonances were first observed by inelastic electron scattering on ^{90}Zr (Fukuda and Torizuka, 1972) and ^{208}Pb (Nagao and Torizuka, 1972). Snover et al. (1974) have used measurements of the fore-aft asymmetry of the proton capture cross section to search for this resonance in ^{209}Bi. Their method is applied to ^{31}P and the possible observation of the isovector quadrupole resonance is discussed.

Chapter II

EXPERIMENTAL APPARATUS AND TECHNIQUES

A. Beam Parameters

Unpolarized proton beams of 5 to 16.1 MeV were provided by the Triangle Universities Nuclear Laboratory tandem Van de Graaff accelerator. After acceleration, the beam was momentum analyzed by a pair of 90 degree bending magnets and by a 30 degree switching magnet. The beam was defined and limited in size and intensity by slits throughout the system. At the exit of the switching magnet, a pair of horizontal and vertical slits defined the final beam image. These slits were shielded from the gamma ray spectrometer by a housing of approximately 20 cm of lead, 20 cm of concrete, and 30 cm of paraffin. The beam was directed to the target chamber by two pairs of magnetic steerers and focused by a magnetic quadrupole lens. The brass scattering chamber is 15.5 cm in diameter and 8 cm deep and was electrically insulated from the remainder of the beam line. The beam was collimated in the chamber by a tantalum collimator assembly with a 4 mm hole placed about 5 cm from the target. The beam on the collimator was generally maintained at less than one nanoampere to reduce the background counting rate

in the gamma ray spectrometer. The beam was collected 3 m downstream from the chamber in a tantalum lined Faraday cup. The Faraday cup was shielded from the spectrometer by 10 cm of lead and 30 cm of paraffin loaded with lithium carbonate.

The polarized proton beam was provided by the TUNL Lamb-shift polarized ion source (Clegg, et al., 1970), and was accelerated and transported as described above. Beam currents of 20 to 60 nA were obtained on target. The beam polarization was determined at the end of every run (before the spin was flipped or the detector angle changed) by the quench-ratio technique (Trainor et al., 1974). The beam was quenched by applying a strong d. c. electric field and the ratio of quenched to unquenched beam was observed on target by the computer, or, when the beam was unstable because of the low intensity of the quenched beam, the ratio was measured manually on a Faraday cup located before the control slits between the two 90 degree bending magnets. A magnetic quench was performed every few hours to check for charged background beam. The polarization was essentially constant during a run, but varied from a low of 75% to a high of 85% over the course of the experiment. The error in the polarization was assumed to be less than 5%.

Beams of unpolarized protons of energies from 16.8 to 28 MeV were obtained from the TUNL cyclograaff accelerator (Purser et al., 1969). The 15 MeV pulsed beam of negative hydrogen ions was injected from the fixed energy cyclotron into the tandem Van de Graaff accelerator. The beam was analyzed and trans-

ported as described above. The high background created by the large neutron flux at these high energies was reduced by utilizing the pulsed beam and time-of-flight techniques.

B. Targets

The silicon oxide targets were prepared by evaporation of enriched (>95%) $^{30}SiO_2$, obtained from Oak Ridge National Laboratory. The silicon dioxide powder was mixed with graphite powder and evaporated through a small hole in a closed tantalum boat (see Appendix A). The purpose of the graphite was to reduce the silicon dioxide to silicon monoxide. The targets were mounted on aluminum target rings which had 7 mm diameter holes.

Since it was not possible to make targets of the thickness desired, the targets were used in pairs with the two targets mounted 1.6 mm apart on the target rod. Two different pairs of targets were used during the experiment. The targets used in the early part of the experiment were each made from two or three layers of self-supporting foils floated individually from glass slides. A second pair of targets was made by evaporation directly onto 10 $\mu g/cm^2$ carbon foils; these targets were considerably thicker than the others. The target thicknesses were obtained from elastic scattering of 1.88 MeV protons at 135°. The cross section for $^{30}Si(p,p)$ at this energy is essentially Rutherford (Outlaw, et al., 1976). Only the thinner targets

were measured by this technique; the thicknesses of the other targets were obtained from a comparison of elastic scattering of 10.9 MeV protons at 160°. The observations of the ^{16}O elastic scattering cross section at these energies and measurements of the energy loss of alpha particles in the targets suggests that the targets contained mostly silicon dioxide and were not reduced to silicon monoxide as expected. The overall target thickness for the thin pair of targets is 0.505 mg/cm² with 55% of that being ^{30}Si. The thickness of the other pair is 1.150 mg/cm², 53% ^{30}Si by mass. The error in these measurements is estimated to be less than 20%, with part of the error due to the inability to resolve the ^{28}Si peak in the elastic scattering spectra at low energies. Although the targets were made from enriched isotope, some ^{28}Si contamination from pump oil is expected to occur during evaporation and use.

C. Detectors

The gamma ray spectrometer used in this experiment is shown in fig. 1. The center detector is a 25.4 by 25.4 cm NaI crystal which is viewed by six RCA-8575 photomultiplier tubes. The crystal is enclosed on the front and sides by an anticoincidence shield of NE110 plastic (Suffert et al., 1968). The shield is in the form of a cylindrical well, 7.6 cm thick at the front and 12.7 cm at the sides. It is viewed by eight XP1031 photomultiplier tubes, two of which are mounted on the

Figure 1. Schematic diagram of the gamma ray spectrometer.

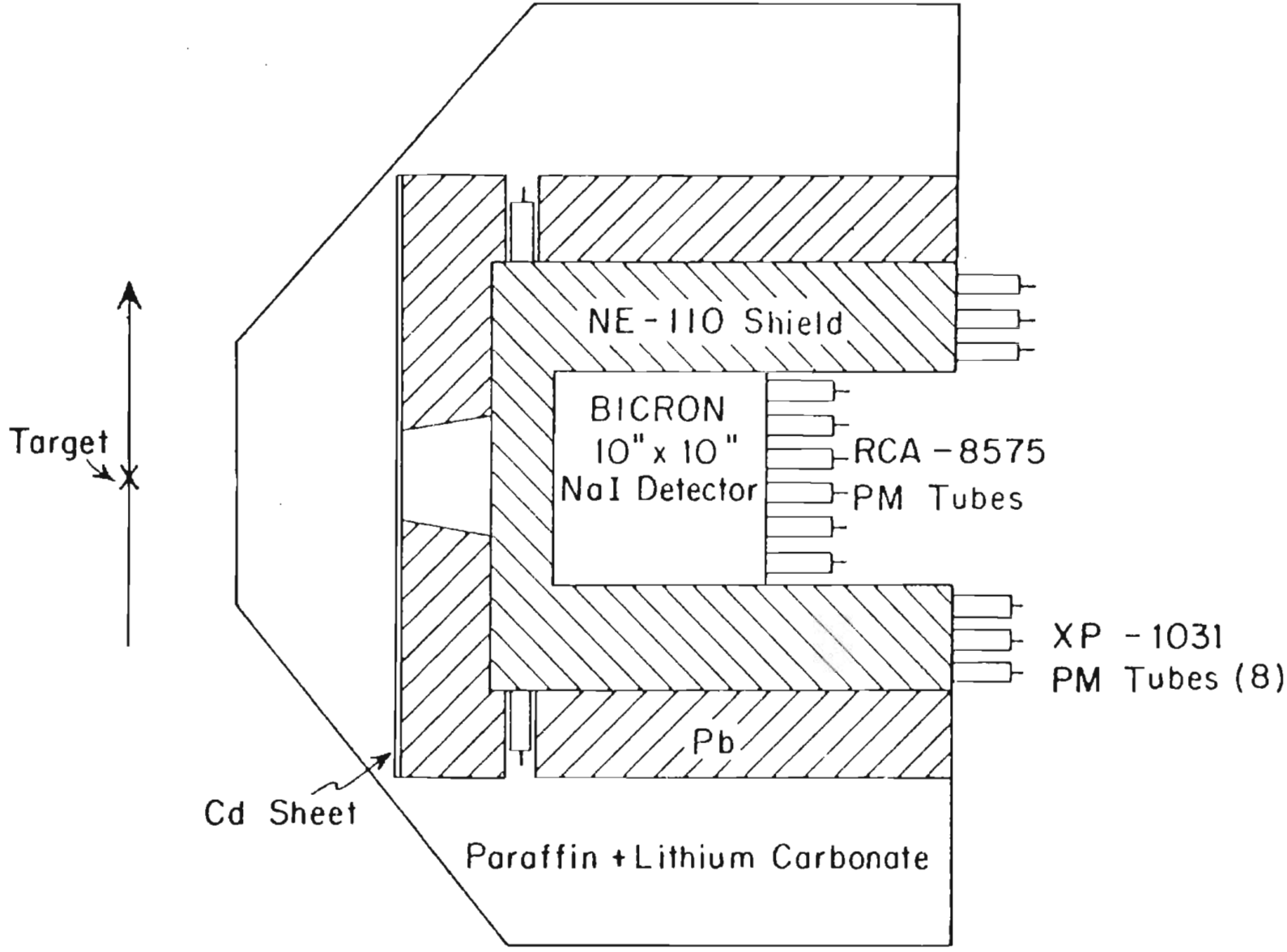
Target
NE-110 Shield
BICRON
10" x 10"
NaI Detector
RCA-8575
PM Tubes
XP-1031
PM Tubes (8)
Pb
Cd Sheet
Paraffin + Lithium Carbonate

front as shown in the figure. The entire assembly is physically shielded to reduce the background counting rate. This shielding consists of 10 cm of lead and 20 cm of paraffin doped with Li_2CO_3 (50% by weight). The back of the assembly is also shielded with 20 cm of doped paraffin (not shown in the figure). In addition, the front contains cadmium sheet between the paraffin and lead shielding.

The back face of the NaI crystal is fully illuminated through the use of a tapered lead collimator which is 20 cm thick and is filled with paraffin. The detector may be placed in either of two positions, each of which has an appropriate size collimator. For the measurement of excitation functions and fore-aft asymmetries, the back face of the detector was positioned 92 cm from the target, corresponding to an angular acceptance of 17.6°. For the measurement of angular distributions, the detector was rolled back to allow an angular range of 42 to 142 degrees. The back face of the NaI crystal was then 102 cm from the target and the angular acceptance was 14.2°.

Two 2000 micron silicon surface barrier detectors were placed in the scattering chamber to monitor both the beam polarization and the integrated charge. The detectors were mounted at 160° to the left and right of the beam direction. The collimation systems for the detectors consisted of a 3.2 mm diameter tantalum collimator which was 4.3 cm from the target and a 1.6 mm diameter collimator which was 6.8 cm from the tar-

get, providing each detector with a solid angle of 0.4 msr.

D. Electronics and Data Collection

There are two major sections of the electonics system; one provides processing of the linear signal from the NaI detector, and the other provides rejection of coincidence events, such as cosmic or escape radiation. A block diagram of the electronics is shown in fig. 2. High current tube bases were used on the 8575 photomultiplier tubes on the center crystal. The purpose of these bases was to improve the gain stability under changes in count rate. The gains of the tubes were matched by adjusting the individual high voltages while observing a source spectrum. The anode signals were summed with a fan-in circuit located in the target room, and the output of the fan-in was clipped by a 160 nanosecond, 50 ohm clipping line which was terminated with a 12 ohm resistor. The use of a partially terminated clipping line produces a clean linear signal which is about 350 nsec wide at the base. The signal was transmitted to the control room by 5G-8 cable where it was fanned out for use in the coincidence circuit as well as for amplification. After amplification by a fast amplifier, one of the signals was used to trigger a fast discriminator. The output of the discriminator triggered a fast linear gate which was opened for 400 nanoseconds to allow the unamplified linear signal to pass into an integrating amplifier. The linear gate was then held closed

Figure 2. Block diagram of electronics. Additional electronics used to measure dead time, accidental rate, time of flight, and charged particles are not shown.

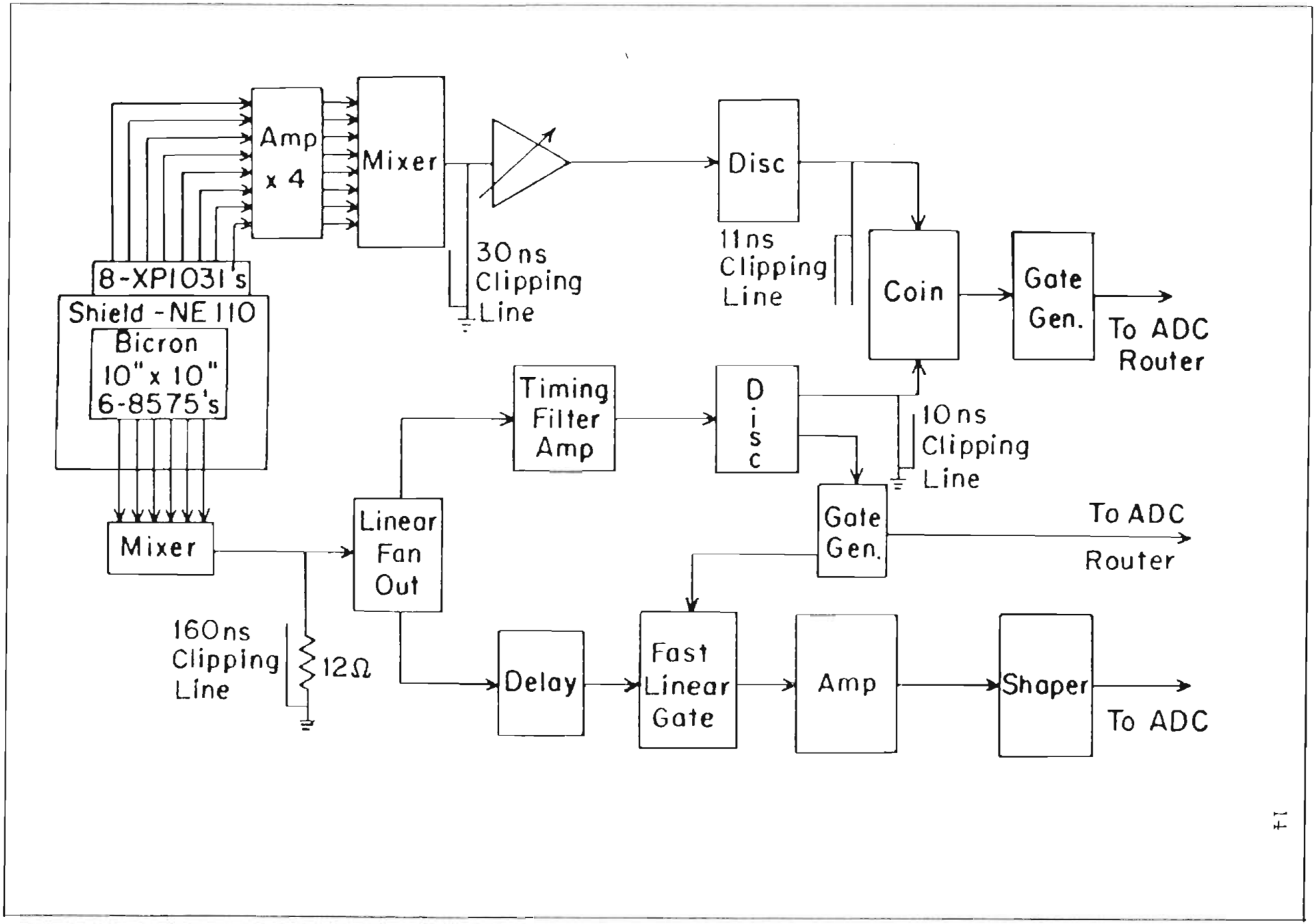
Amp
x 4
Mixer
Disc
30 ns
Clipping
Line
11ns
Clipping
Line
Coin
Gate
Gen.
To ADC
Router
8-XP1031's
Shield - NE 110
Bicron
10" x 10"
6-8575's
Timing
Filter
Amp
D
i
s
c
10ns
Clipping
Line
Gate
Gen.
To ADC
Router
Mixer
Linear
Fan
Out
160ns
Clipping
Line
12Ω
Delay
Fast
Linear
Gate
Amp
Shaper
To ADC

for 10 microseconds to allow processing of the signal and to prevent pulse pile-up in the integrating amplifier.

The signals from the shield photomultiplier tubes were amplified before summing. The output of the fan-in was clipped by a 30 nansecond, 50 ohm, shorted cable and the signal was transmitted by RG-8 cable to the control room. The signals were further amplified by a factor of sixty four before being sent to a fast discriminator. The outputs of the discriminator were clipped, as shown in fig. 2, before entering the fast coincidence module. An additional fast coincidence module (not shown) with a long delay before one input was used to determine the accidental coincidence count rate.

The pulsed beam of the cyclotron was utilized to improve rejection of the neutron background by time-of-flight. A wire loop in the cyclotron vault picked up the radio frequency field of the cyclotron, and a zero crossing discriminator provided a stop signal for a time to amplitude converter. The start signal, indicating an event in the NaI crystal, was obtained from a constant fraction discriminator. The TAC output was then sent to an ADC.

A DDP-224 computer was used to collect and process the data. The linear signal was stored in a true event spectrum if there was no coincident event detected in the shield and was routed to a rejected spectrum if a coincidence was detected. The shield gain and discriminator could be adjusted to provide various rejection rates of the first and second escape peaks.

In general, the discriminator was set to provide clear resolution of the decays to the ground and first excited states without lowering the discriminator into the noise. A typical spectrum is shown in fig. 3. Under ideal conditions, the system has achieved resolution of 2.4% (Weller et al., 1976); however, under normal running conditions, the resolution was 3-4% as in the spectrum shown in the figure.

When polarized beam was used, the events were routed into separate arrays for each spin state measurement. Similarly, the charged particle events were amplified, routed, and stored according to the spin state. When the pulsed beam of the cyclotron was used, the time of flight was stored in coincidence with the energy of the observed gamma ray. A window was placed in the TAC spectrum, and the energy events were sorted into one of six spectra according to whether or not there was a coincidence between the shield and the crystal and whether the associated time event was below, in, or above the TAC window. A spectrum which was taken with the cyclograaff beam is shown in fig. 4.

The beam current from the Faraday cup was integrated and scaled in three scalers. One counted all units of charge, and the other two were gated off when the gamma ray or particle systems were busy. The dead time correction for the gamma rays was obtained from the computer interface and from the previously mentioned dead time of the linear gate. All spectra, scalers, and the quench-ratio measurements mentioned previously

Figure 3. The $^{30}Si(p,\gamma)^{31}P$ spectrum at 90° for a 15 MeV d. c. proton beam. The transitions to the ground, first, and second excited states are indicated by arrows. Also indicated are energies corresponding to groups of higher energy states.

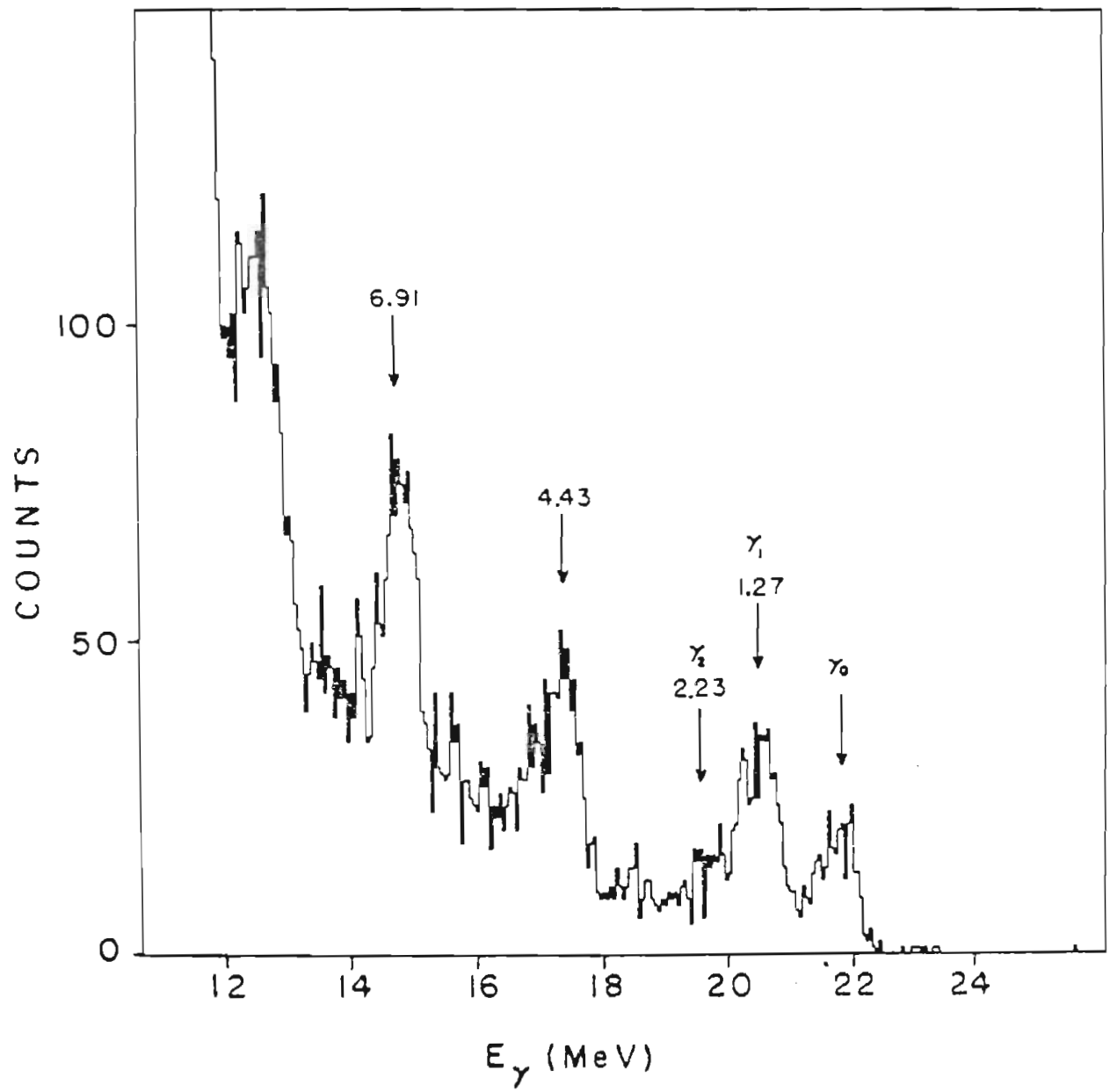
6.91
4.43
γ_1
1.27
γ_2
2.23
γ_0
100
50
0
COUNTS
12
14
16
18
20
22
24
E_γ (MeV)

Figure 4. The $^{30}Si(p,\gamma)^{31}P$ spectrum at 125° for a 19 MeV pulsed proton beam. The transitions to the ground and first excited states are indicated.

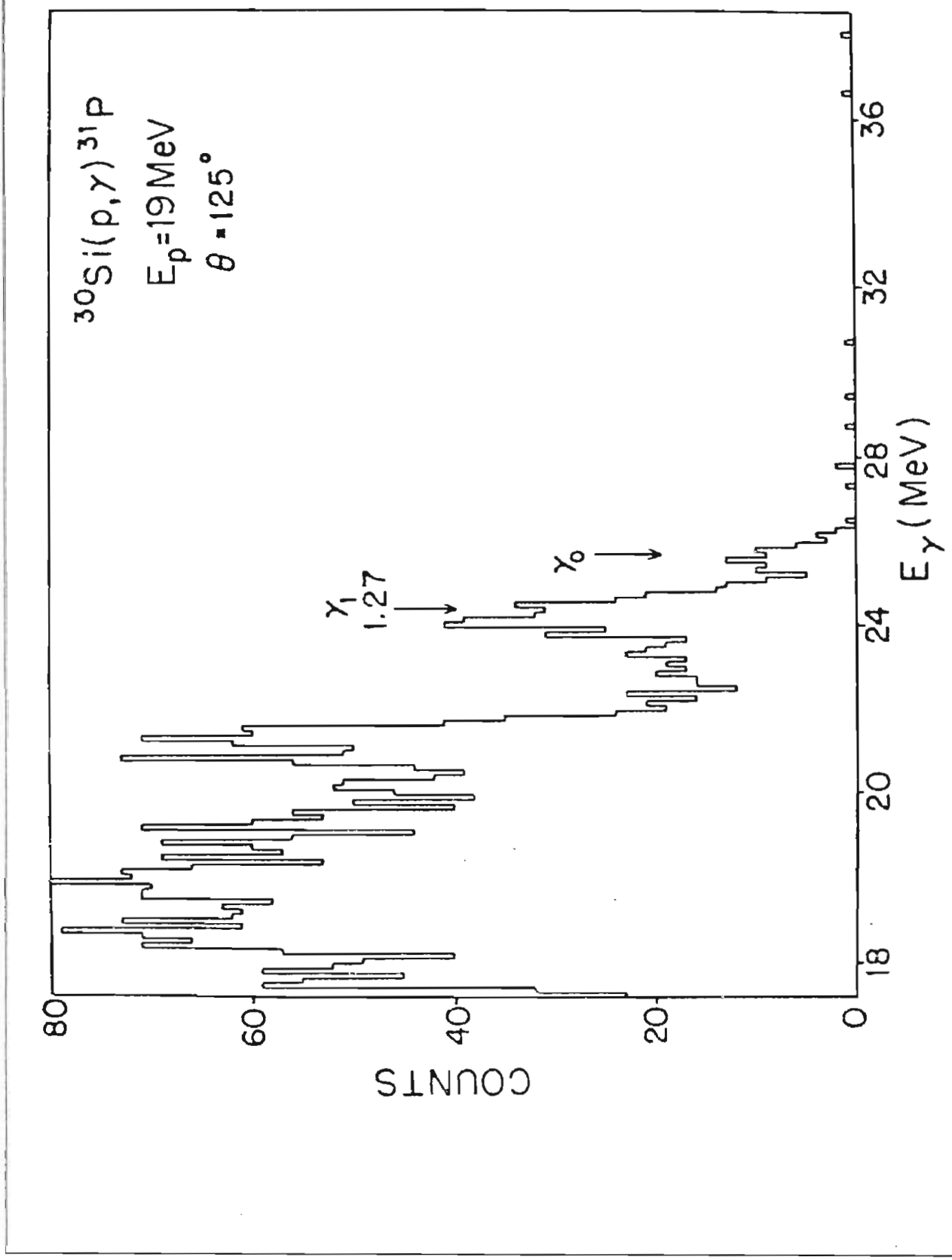
$^{30}Si(p,\gamma)^{31}P$
E_p=19 MeV
θ = 125°
γ_1
1.27
γ_0
COUNTS
E_γ (MeV)
0
20
40
60
80
18
20
24
28
32
36

were recorded on magnetic tape for later analysis off-line.

Chapter III

DATA REDUCTION

A. Fitting and Stripping Procedures

The various spectra were analyzed with the TUNL off-line computer. A standard line shape, as determined from the $^{3}H(p,\gamma)^{4}He$ reaction, was used to fit the gamma ray peaks of interest. The $^{3}H+p$ reaction was used to obtain the standard line shape because of the high Q value and the large separation of the excitation energies of the ground and first excited states in ^{4}He. The details of the fitting parameters and line shape are given by McBroom (1977).

A fitted spectra is shown in fig. 5. The widths of the gamma ray peaks were first obtained as a function of energy from those spectra for which the γ_0 yield was large. It was found that the widths increased with energy in a smooth and sytematic way over the energy region studied. All of the spectra were fit with a fixed width; the width was set to correspond to the energy of the gamma ray.

The yield in the peak from γ_1 was obtained by subtracting off the fit for γ_0 and fitting the remaining peak. At energies below 16 MeV, the peaks were separated clearly enough for this

Figure 5. Spectrum with fitted line shape. Line shapes fitted to the individual peaks of fig. 4 are shown as dashed lines. The solid line represents the sum of the fits.

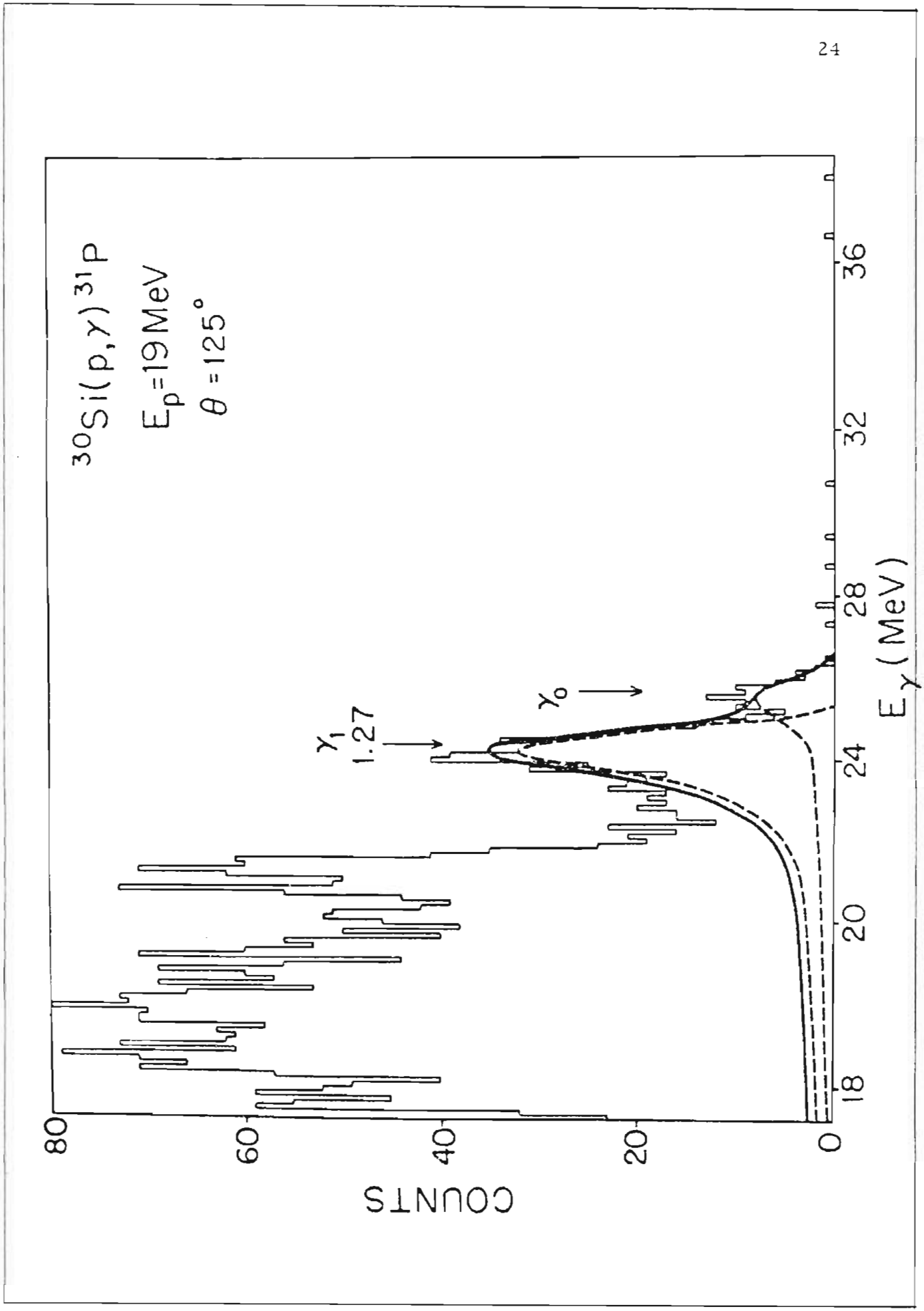
$^{30}Si(p,\gamma)^{31}P$
E_p=19 MeV
θ = 125°
γ_1
1.27
γ_0
COUNTS
0
20
40
60
80
18
20
24
28
32
36
E_γ (MeV)

to be done easily. Peaks corresponding to decays to higher excited states are shown in fig. 3; however, in practice, they could not be summed reliably at all angles and energies.

For spectra at higher bombarding energies like that shown in fig. 5, the leading edge of the γ_1 peak begins to contaminate the peak due to γ_0. Since the γ_0 yield becomes less at even higher energies, this effect becomes increasingly important. By fixing the separation of the two peaks as well as the widths, more satisfactory fits could be obtained. The peaks were fit simultaneously by an iterative procedure which required stripping γ_0 from the spectrum, fitting γ_1, then stripping γ_1 from the original spectrum and refitting γ_0 and so on until the sums under each of the peaks no longer changed. Since the yield in γ_1 is fairly strong relative to γ_0 above 16 MeV proton energy, it is believed to have been summed accurately, but the γ_0 data may contain some systematic errors.

The efficiency of the spectrometer system depends upon the portion of the spectra that is summed as well as upon the fraction of the escape peaks that are rejected. In this experiment, the total area beneath the line shape is believed to give the best sums of the yields, independent of the relative yields of γ_0 and γ_1. A comparison with well resolved peaks summed by including only the region from the minimum on the low energy side of the γ_0 peak to the high energy edge was very favorable. The absolute efficiency of the detector system was determined by means of the $^{12}C(p,\gamma_0)^{13}N$ reaction (Mans et al., 1968) as

described in Weller et al. (1978). When the data are fit with the line shape described, the efficiency is 33±8%.

B. Normalization to Monitor Detectors

During most of the measurements of the angular distributions of gamma rays, the elastically scattered protons were observed in the charged particle monitor detectors at 160°. The angular distribution data were normalized to the proton yield due to elastic scattering from ^{30}Si. In general, the corrections were small and were probably due as much to thickness variations over the target face as to uncertainities in the charge collection.

The asymmetry as well as the total yield of the $^{30}Si(p,p)$ reaction was obtained in the left-right pair of detectors for each spin state. The fluctuations in the asymmetry were compared to the fluctuations in the polarization as determined by the quench ratio and the differences were found to be within the error of the quench ratio. The analyzing power, which is the assymetry divided by the polarization determined from the quench ratio, was averaged for each angular distribution. The beam polarization for each angle was then determined by comparing the average analyzing power to the assymetry measured by the particle detectors.

Chapter IV

EXCITATION FUNCTIONS

A. The $^{30}Si(p,\gamma_0)^{31}P$ and $^{30}Si(p,\gamma_1)^{31}P$ Reactions

Excitation functions were measured for the reaction $^{30}Si(p,\gamma)^{31}P$ where both γ_0, the decay to the ground state, and γ_1, the decay to the first excited state, were observed. The 90 degree differential cross section was measured in 50 keV steps up to 16.1 MeV. The pair of targets used in these measurements had a combined energy loss of less than 20 keV for 10 MeV protons. The cyclograaff beam was used to measure the cross section at 16.8 MeV and in 1 MeV steps from 18 to 28 MeV. The pair of targets used in these measurements were approximately 22 keV thick for 20 MeV protons. The results of these measurements are shown in fig. 6.

The resonance observed by detecting γ_1 is usually described as a resonance built upon the first excited state. Thus, the excitation energy of the resonance seen in the (p,γ_1) reaction is the excitation energy above the first excited state, which corresponds to the gamma ray energy shown in the upper scale of the figure. Decay by E1 radiation to the $3/2^+$ first excited state may come from either $1/2^-$, $3/2^-$, or $5/2^-$ states in the

Figure 6. The excitation functions for $^{30}Si(p,\gamma_0)^{31}P$ and $^{30}Si(p,\gamma_1)^{31}P$ measured at a laboratory angle of 90°. The error bars represent the statistical errors associated with the data points. The solid lines are composed of straight lines connecting the data points.

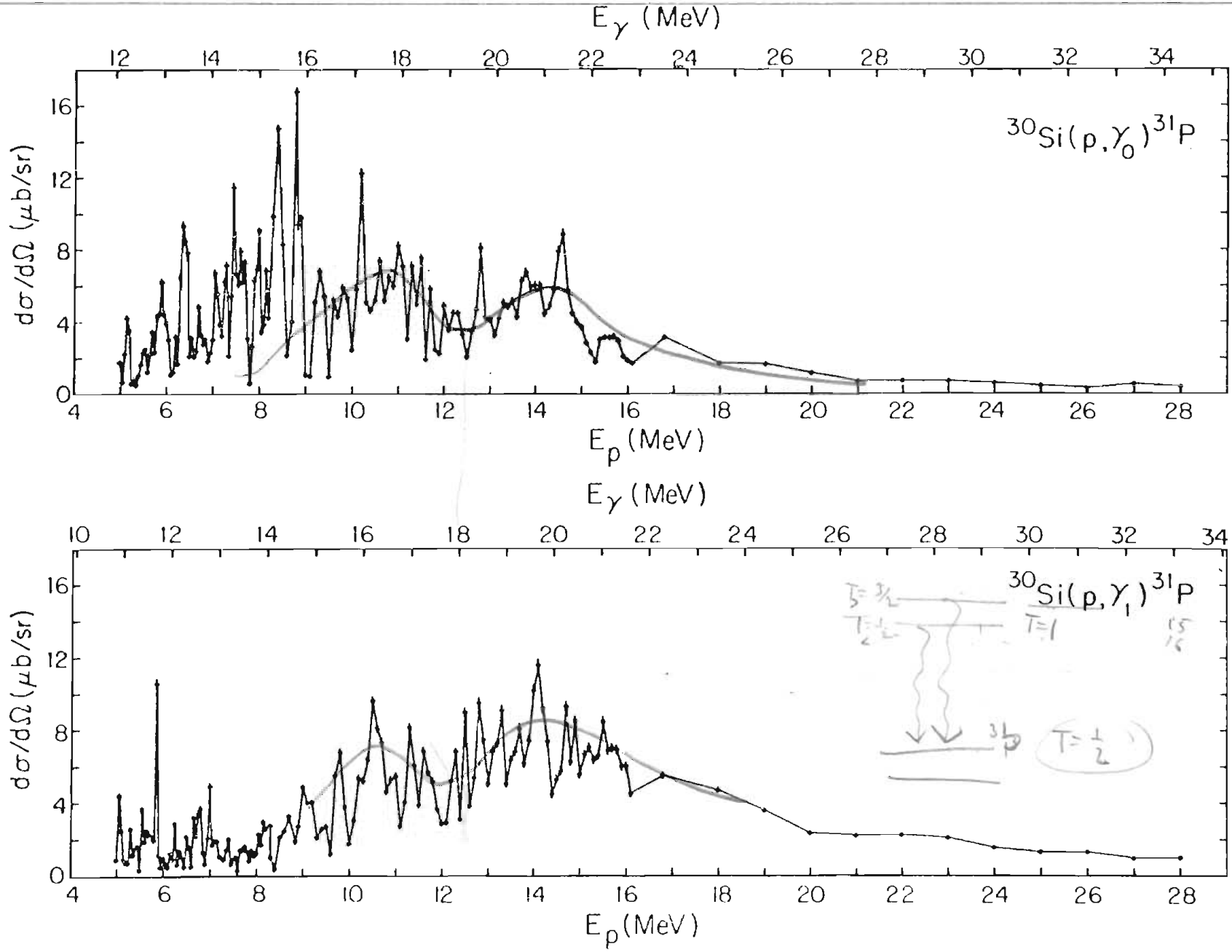
E_γ (MeV)
12 14 16 18 20 22 24 26 28 30 32 34
$^{30}Si(p,\gamma_0)^{31}P$
$d\sigma/d\Omega$ (μb/sr)
0 4 8 12 16
4 6 8 10 12 14 16 18 20 22 24 26 28
E_p (MeV)
E_γ (MeV)
10 12 14 16 18 20 22 24 26 28 30 32 34
$^{30}Si(p,\gamma_1)^{31}P$
T=1
^{31}P
$T=\frac{1}{2}$
$d\sigma/d\Omega$ (μb/sr)
0 4 8 12 16
4 6 8 10 12 14 16 18 20 22 24 26 28
E_p (MeV)

resonance. Decay by E1 radiation to the ground state may also come from $1/2^-$ and $3/2^-$ states, so the possibility of decay to either the ground or first excited states is possible from a single state. However, to the extent to which the resonance is coupled, in terms of the (γ,p) reaction, to the initial state, the resonances observed via (p,γ_0) and (p,γ_1) would be two separate resonances.

B. Structural Details of the Giant Dipole Resonance

The photodisintegration reaction $^{31}P(\gamma,n)^{30}P$ has been investigated by Gellie et al. (1973) and the results from the detection of the ground state photoneutrons and from the total photoneutron cross section are shown in fig. 7. For the purpose of comparison, the (p,γ_0) cross section has been converted to (γ,p_0) by the process of detailed balance. The location of the centroid of the giant dipole resonance is empirically predicted for this mass region to be near $E_x=63/A^{1/3}$ MeV = 20 MeV for ^{31}P (Hayward, 1970). The (γ,n) cross section is seen to peak just below this energy, as does the (p,γ_1) cross section (fig. 6). Both the (γ,n_0) and (γ,p_0) cross sections show considerable strength in the region from 13 to 16 MeV excitation while the (p,γ_1) cross section and the remainder of the (γ,n) cross section are just beginning to build in that region. Dearnaley et al. (1965) have studied the giant dipole resonance of ^{32}S via radiative capture of protons by ^{31}P and their data is shown in

Figure 7. The excitation function for $^{30}Si(p,\gamma_0)^{31}P$ presented as $^{31}P(\gamma,p_0)^{30}Si$ by the process of detailed balance. Also shown are the excitation functions for $^{31}P(\gamma,n_0)^{30}P$ and $^{31}P(\gamma,n)^{30}P$ (Gellie et al., 1973). The lower scale [E_γ(MeV)] applies to the lower edge of the upper portion of the figure as well.

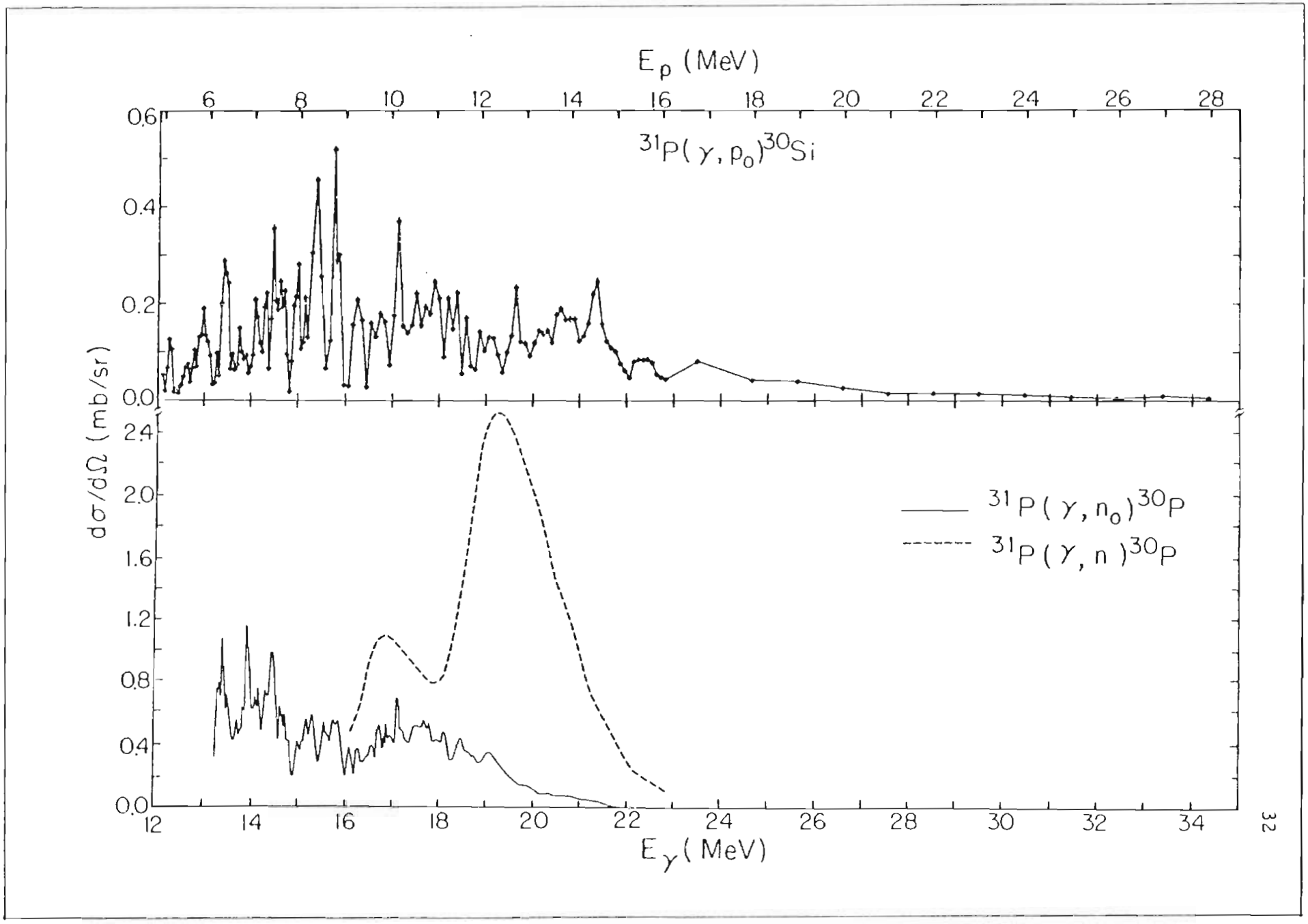
E_p (MeV)
6
8
10
12
14
16
18
20
22
24
26
28
$^{31}P(\gamma, p_0)^{30}Si$
0.6
0.4
0.2
0.0
$d\sigma/d\Omega$ (mb/sr)
2.4
2.0
1.6
1.2
0.8
0.4
0.0
$^{31}P(\gamma, n_0)^{30}P$
$^{31}P(\gamma, n)^{30}P$
12
14
16
18
20
22
24
26
28
30
32
34
E_γ (MeV)

fig. 8. The giant resonance of ^{31}P could be expected to be similar to that of ^{32}S if ^{31}P may be thought of as ^{32}S with a spectator $s_{1/2}$ hole. The excitation functions show similar behavior; especially noticeable is the strength that appears in the region from 13 to 16 MeV. Singh et al. (1965) have observed the reaction $^{27}Al(p,\gamma)^{28}Si$ and their results for the ground state excitation function are also shown in fig. 8. The region above 16 MeV excitation is quite similar in general appearance to the excitation functions of ^{31}P and ^{32}S; however, relatively little yield is observed below 16 MeV. The absence of yield below the GDR of ^{28}Si indicates the phenomenon is not a general feature of the mass region. The origin of the phenomenon is not understood.

In their discussion of ^{32}S, Dearnaley et al. (1965) interpret the fine structure observed in ^{32}S to be due to resonances rather than fluctuations; however, Singh et al. (1965) observed both the reactions $^{27}Al(p,\gamma_0)^{28}Si$ and $^{27}Al(p,\gamma_1)^{28}Si$ in 15 keV steps over the resonance region, and they concluded from a statistical analysis that the structure in ^{28}Si is due to fluctuations. They also suggest the possibility of intermediate structure, which is at least partially supported by some calculations which couple particle-hole states to collective states through the use of the intermediate coupling model (Malik and Mustafa, 1970). No such detailed analyses have been performed in the present work, and no conclusion is drawn about the nature of the observed structure in the giant dipole resonance.

Figure 8. The excitation functions for $^{31}P(p,\gamma_0)^{32}S$ (Dearnaley et al., 1965), $^{27}Al(p,\gamma_0)^{28}Si$ (Singh et al., 1965), and the $^{30}Si(p,\gamma_0)^{31}P$ data of fig. 6.

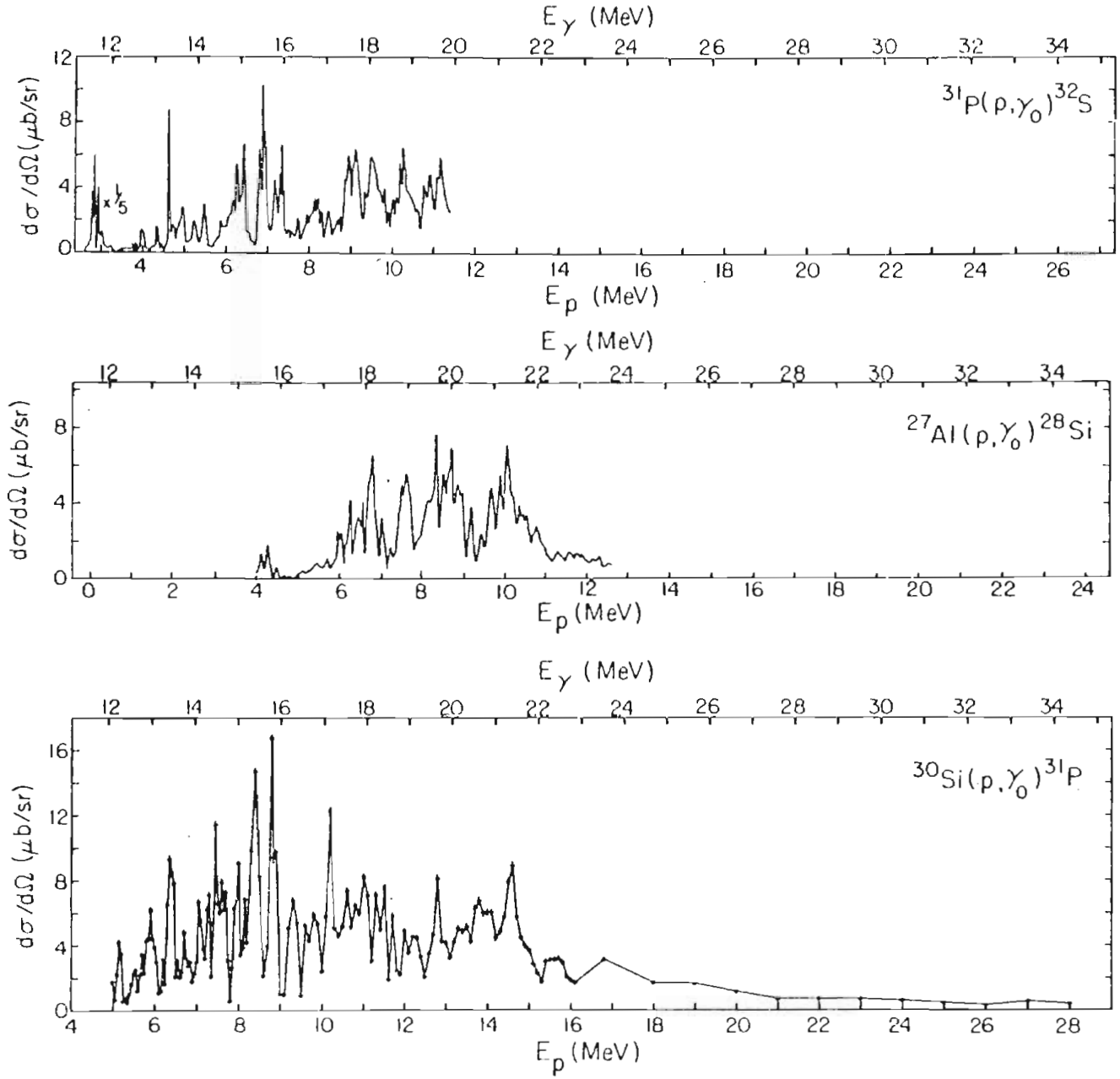
E_γ (MeV)
$^{31}P(p,\gamma_0)^{32}S$
$d\sigma/d\Omega(\mu b/sr)$
x 1/5
E_p (MeV)
E_γ (MeV)
$^{27}Al(p,\gamma_0)^{28}Si$
$d\sigma/d\Omega$ (μb/sr)
E_p (MeV)
E_γ (MeV)
$^{30}Si(p,\gamma_0)^{31}P$
$d\sigma/d\Omega$ (μb/sr)
E_p (MeV)

C. Isospin Splitting of the Giant Dipole Resonance

The implications of the isovector nature of the electric dipole operator have been widely discussed, particularly in terms of the possibility of isospin splitting of the giant dipole resonance (see, for example, Akyuz and Fallieros; 1971, and the summaries by Hayward, 1970; and Paul, 1973). The isospin selection rule for the dipole operator requires that $\Delta T=0\pm1$ for $T_z\neq0$, and $\Delta T=1$ for $T_z=0$; therefore, for a nucleus with a $T=1/2$ ground state like ^{31}P, the giant resonance built upon the ground state may be split into two components: $T=1/2$ and $T=3/2$. The $T_<$ and $T_>$ components may both decay by proton emission to (or be excited by proton capture from) ^{30}Si, but only the $T_<$ component is allowed to decay by neutron emission to the $T=0$ ground state of ^{30}P. $T=3/2$ states may, however, decay by neutron emission to the $T=1$ first excited state as well as higher $T=1$ states of ^{30}P.

Simple expressions have been given for the relative strengths and splitting of the $T_<$ and $T_>$ components of the giant dipole resonance. The estimated splitting between the $T_<$ and $T_>$ components for ^{31}P is (Akyuz and Fallieros, 1971)

$$\Delta E = \frac{60(T_0+1)}{A}\ MeV = 2.9\ MeV$$

where T_0 is the isospin of the ground state, and the estimate of the relative strengths is (Fallieros and Goulard, 1970)

$$\frac{S(T_0+1)}{S(T_0)} \cong \frac{1}{T_0}\left[\frac{1-3/2\,(T_0/A^{2/3})}{1+3/2\,(1/A^{2/3})}\right] = 2.5 \quad .$$

An alternative estimate of the strengths may be obtained from the isospin Clebsch Gordon coefficients alone. If the (γ,p) and (γ,n) reactions take up all of the reaction cross section, then, for the (γ,p) reaction alone, the relative strengths for ^{31}P are (Maher et al., 1974)

$$\frac{S(T_>)}{S(T_<)} = \frac{4T_0+3}{T_0(2T_0+1)} = 5.$$

Above 16 MeV excitation energy, the yield from the $^{30}Si(p,\gamma_0)^{31}P$ reaction suggests the presence of two broad peaks centered at 17.7 MeV and 21 MeV excitation energy. These regions may be integrated and compared with the same regions for $^{31}P(\gamma,n_0)^{30}P$. The results are summarized in Table I. The excitation function of $^{31}P(\gamma,p_0)^{30}Si$ has been integrated assuming an average value of 0.9 for a_2 and 0.0 for a_4 (see Chapter V). The excitation function for $^{31}P(\gamma,n_0)^{30}P$ was integrated under the assumption that the angular dependence of the yield is $\sin^2\theta$. The results are also given for the decay to the first excited state of ^{31}P, also T=1/2; in this case, a_2 and a_4 were assumed to have an average value of 0. If we associate these two regions with the $T_<$ and $T_>$ components of the GDR, the integrated proton strength, which is observed to be approximately the same in the two regions, is in contrast to the predictions. However, the predictions of Akyuz and Fallieros are for the total photon absorption cross section and may not apply to the (γ,p_0) channel alone. In agreement with the selection

Table I. Comparisons of yields from proposed $T_<$ and $T_>$ components of the GDR. The energy region integrated extends from 16 to 23 MeV excitation with the division between the $T_<$ and $T_>$ components assumed to occur at 19.4 MeV.

	$\int\sigma dE$ (mb-MeV)		
	$T_<$	$T_>$	$T_</T_>$
$^{31}P(\gamma,p_0)^{30}Si$	4.5	3.9	0.86
$^{31}P(\gamma,n_0)^{30}P$[a]	10.9	1.7	0.16
$^{31}P^*(\gamma_1,p_0)^{30}Si$	8.8	8.5	0.96
$^{31}P(\gamma,n_1+n_2)^{30}P$[a]	4.4	11.8	2.7

[a]Gellie et al., 1973

rules, the (γ,n_0) strength in the isospin forbidden $T_>$ region is observed to drop off sharply. Thus, the proposed identification of the $T_<$ and $T_>$ regions seems reasonable, and the separation of the two components is in accord with the theoretical predictions.

Further evidence for isospin splitting may be found in the data of Gellie et al. (1973) for the $^{31}P(\gamma,n_1+n_2)^{30}P$ reaction. The first and second excited states of ^{30}P have T=1 and T=0, respectively. As indicated earlier, the decay from the $T_>$ component to T=1 states is allowed, and if the identification of the 21 MeV region as $T_>$ is correct, than the yield from (γ,n_1) should not drop off as sharply as the (γ,n_0) yield does above 19 MeV. The 90° differential cross section for (γ,n_1+n_2) in fact is observed to rise at about 18.5 MeV to a peak at 20 MeV and then decreases to half the peak value at 23 MeV. The $T_<$ and $T_>$ regions have been integrated under the assumption that the yield from the reaction is isotropic, and the results are given in Table I.

The reactions $^{31}P(p,\gamma_0)^{32}S$ and $^{27}Al(p,\gamma_0)^{28}Si$ show distributions of strengths which are similar to that observed for $^{30}Si(p,\gamma_0)^{31}P$. Both of these nuclei are self-conjugate nuclei, and only the $T_>$ portion of the resonance is allowed by the isospin selection rules, thus seeming to contradict the earlier supposition that the $T_<$ portion of the resonance is centered near 17.7 MeV. In a study of the reactions $^{24}Mg(\alpha,\gamma_0)^{28}Si$ and $^{28}Si(\alpha,\gamma_0)^{32}S$, Meyer-Schutzmeister et al., (1968) conclude that

the giant dipole resonance of ^{28}Si may be heavily mixed with nearby 1$^-$ T=0 states. The alpha particle may be captured into a T=0 state of an excited self-conjugate nuclei, but the subsequent decay by E1 radiation to the ground state is isospin forbidden. Since the gamma rays from these alpha capture reactions were observed from angular distribution measurements to be E1, mixing of the T=1 dipole states with T=0 states is implied. The cross section for ^{24}Mg$(\alpha,\gamma_0)^{28}$Si is observed to be smaller than and centered on the low side of the ^{27}Al$(p,\gamma_0)^{28}$Si cross section, consistent with a picture in which alpha capture, through isospin mixing, excites the T=0 component of the GDR of ^{28}Si. The strength observed in the $T_<$ portion of the proton cross section could also be due to mixing, and so the data for ^{28}Si, because of the mixing, does not necessarily contradict the description of isospin splitting proposed for ^{31}P.

For non-self-conjugate nuclei, one of the techniques used by investigators to study isospin splitting is a comparison of the excitation functions of the (p,γ_0) and (α,γ_0) reactions. On the basis of the selection rules, the (α,γ_0) reaction should populate only $T_<$ states while the (p,γ_0) reaction may populate both $T_<$ and $T_>$ states. However, while such effects are observed (Paul, 1973; Rickel et al., 1976), such comparisons for non-self-conjugate nuclei do not offer as firm support for isospin theory as once thought. The work of Rickel et al. on the giant dipole resonance of ^{56}Fe shows that the high energy

side of the yield curve of the (α, γ_0) reaction should decrease relative to the (p, γ_0) yield simply because of the energy dependence of the transmission coefficients. In addition, Meyer-Schutzmeister et al. (1968) have suggested that if the GDP is assumed to consist of one-particle-one-hole states, then the emission of an alpha particle should be strongly inhibited, thus complicating the comparison of (γ, p_0) and (γ, α_0) yields.

A comparison of the (γ, n_0) and (γ, p_0) yields is preferable, but has usually not been possible. In the present case, however, such a comparison has been possible and the results are in reasonable accord with the theory of isospin.

Another possible cause of splitting of the giant dipole resonance is deformation splitting, which is calculated from the ground state quadrupole moment, Q_0 (Danos, 1958). The resonance energies E_a and E_b are related to the major and minor axes, a and b, by

$$\frac{E_b}{E_a} = 0.911 \frac{a}{b} + 0.089$$

where d=a/b is obtained from Q_0 as follows (Hayward, 1970):

$$Q_0 = \frac{2}{5} (r_0)^2 A^{2/3} Z \frac{d^2 - 1}{d^{2/3}} .$$

The ground state quadrupole moment for ^{31}P is not known; however, in this mass region, Q_0 tends to be larger than 0.5 or less than -0.4 (Hauser et al., 1971). If the two components of the resonance are assumed to be split around 18 MeV, the predicted splitting is 3.6 MeV if Q =0.5 and -4.0 MeV if Q =-0.4. These

values are somewhat larger than those predicted by isospin, but are reasonable in comparison with the data.

Chapter V

ANGULAR DISTRIBUTIONS

A. Fits to Legendre Polynomials

Angular distributions of cross section and analyzing power of the $^{30}Si(p,\gamma_0)^{31}P$ reaction were measured at twelve energies, and the results are shown in figs. 9 and 10. In addition, angular distributions of cross section were observed with unpolarized beam at six other energies and the results are shown in fig. 11. The measurements were made at seven angles: 42°, 55°, 70°, 90°, 110°, 125°, and 142°.

The angular distributions of cross section are plotted as $\sigma(\theta)/a_0$ where, for polarized beam,

$$\sigma(\theta) = N_+ + N_-$$

and N_+ is the yield observed for the spin up measurement, N_- is the yield observed for spin down and a_0 is given below. The angular distributions of analyzing power are plotted as $\sigma(\theta)A(\theta)/a_0$ where

$$A(\theta) = \left(\frac{N_+ - N_-}{N_+ + N_-}\right)\frac{1}{P}$$

and P is the beam polarization. The error bars on the data

Figure 9. Angular distributions of cross section and analyzing power from the $^{30}Si(p,\gamma_0)^{31}P$ reaction for incident proton energies of 6.36, 7.46, 8.4, 8.81, 8.85, and 10.225 MeV. The error bars represent the statistical error associated with the data points. The solid curves indicate the fits to the data including all polynomials up to order 4 as described in the text, while the dashed curves indicate the fits to the data including all polynomials up to order 3.

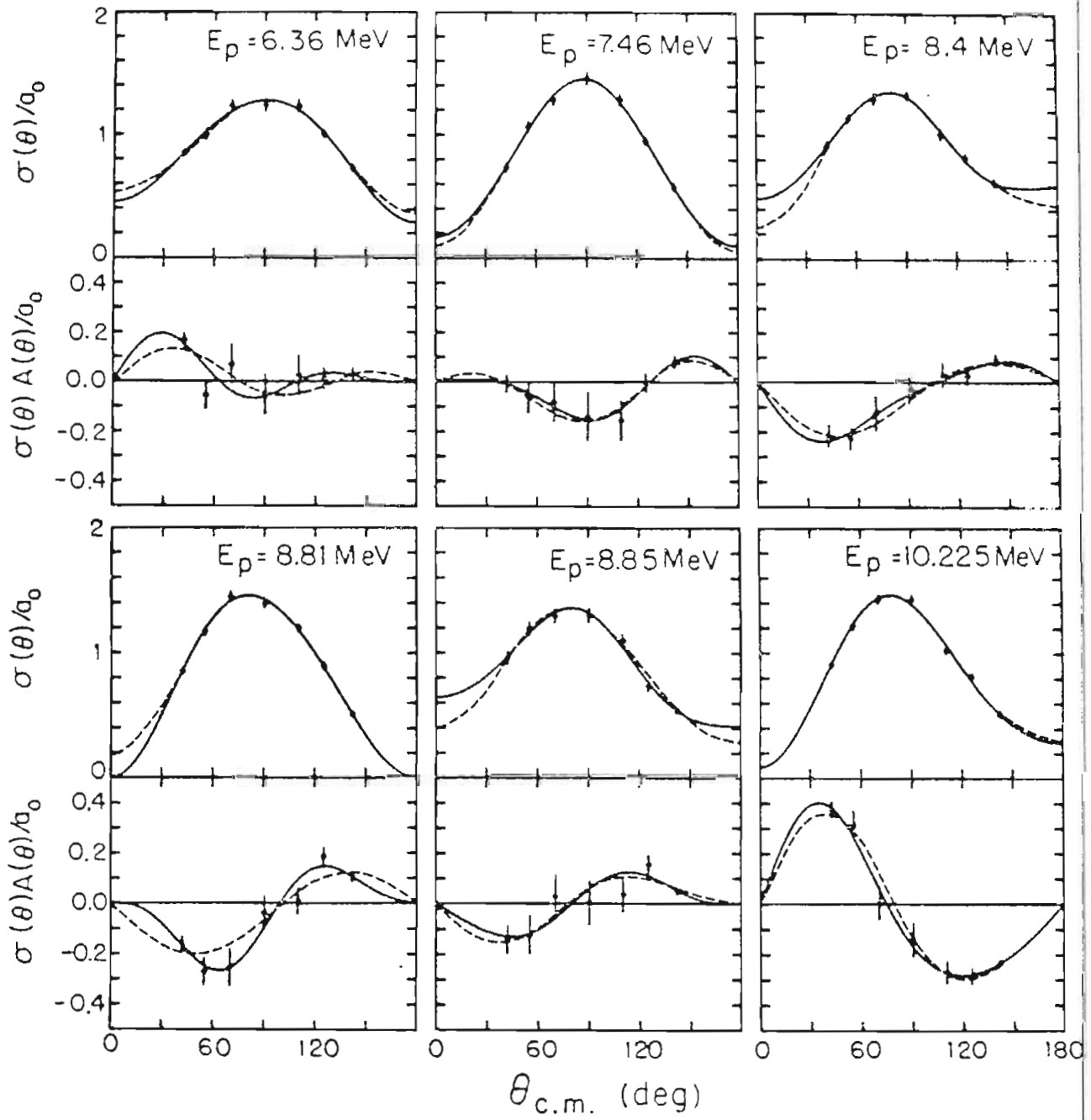
E_p = 6.36 MeV
E_p = 7.46 MeV
E_p = 8.4 MeV
E_p = 8.81 MeV
E_p = 8.85 MeV
E_p = 10.225 MeV
$\sigma(\theta)/a_0$
$\sigma(\theta)A(\theta)/a_0$
$\theta_{c.m.}$ (deg)

Figure 10. Angular distributions of cross section and analyzing power from the $^{30}Si(p,\gamma_0)^{31}P$ reaction for incident proton energies of 11.01, 12.0, 12.85, 13.775, 14.625, and 14.95 MeV. The error bars represent the statistical error associated with the data points. The solid curves indicate the fits to the data including all polynomials up to order 4 as described in the text, while the dashed curves indicate the fits to the data including all polynomials up to order 3.

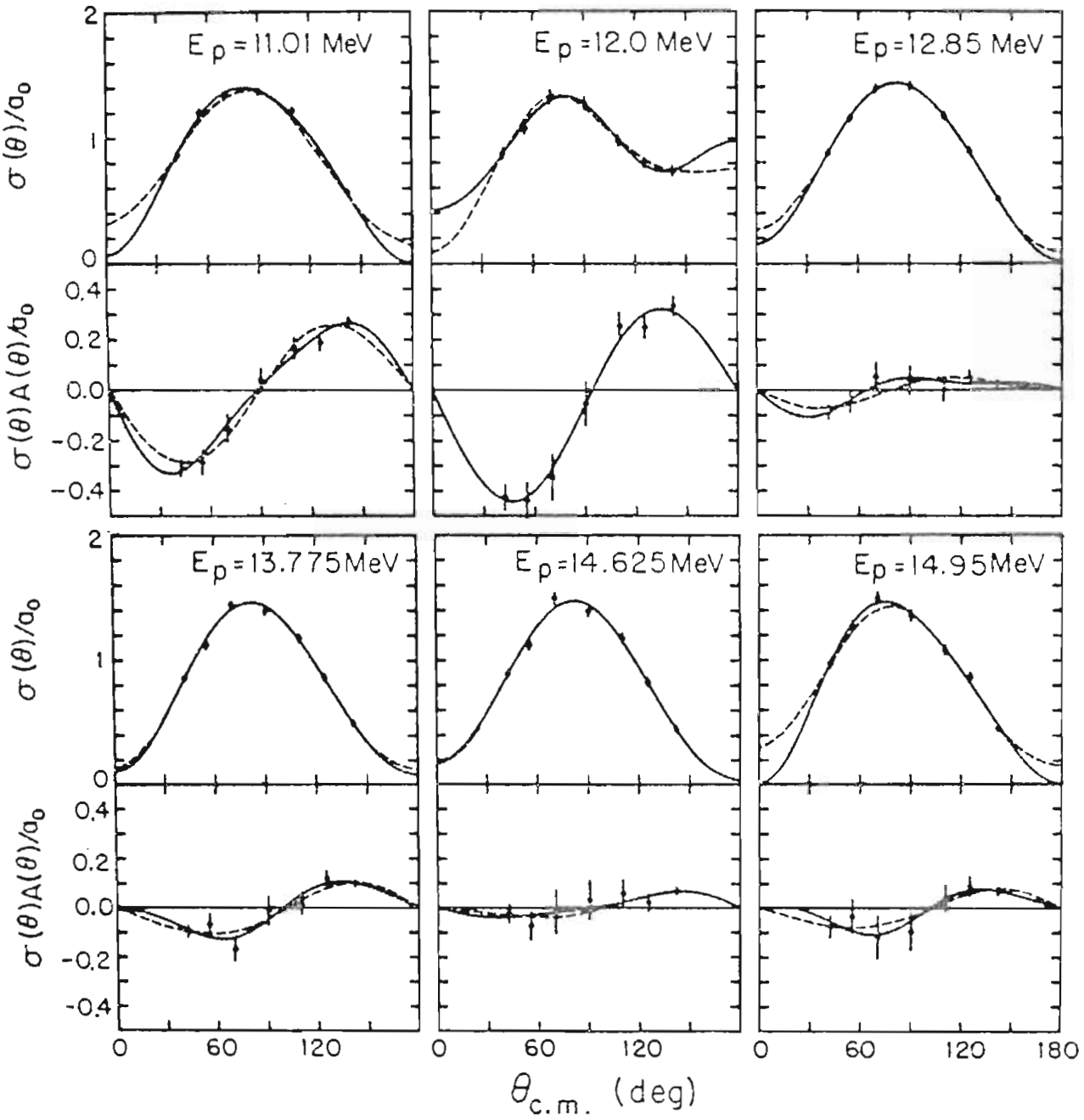
E p = 11.01 MeV
E p = 12.0 MeV
Ep = 12.85 MeV
E p = 13.775 MeV
E p = 14.625 MeV
Ep = 14.95 MeV
σ(θ)/σ₀
σ(θ)A(θ)/σ₀
θc.m. (deg)

Figure 11. Angular distributions of cross section from the $^{30}Si(p,\gamma_0)^{31}P$ reaction for incident proton energies of 8.25, 8.5, 8.55, 8.65, 8.925, and 12.8 MeV. The error bars represent the statistical error associated with the data points. The solid curves indicate the fits to the data including all polynomials up to order 4 as described in the text, while the dashed curves indicate the fits to the data including all polynomials up to order 3.

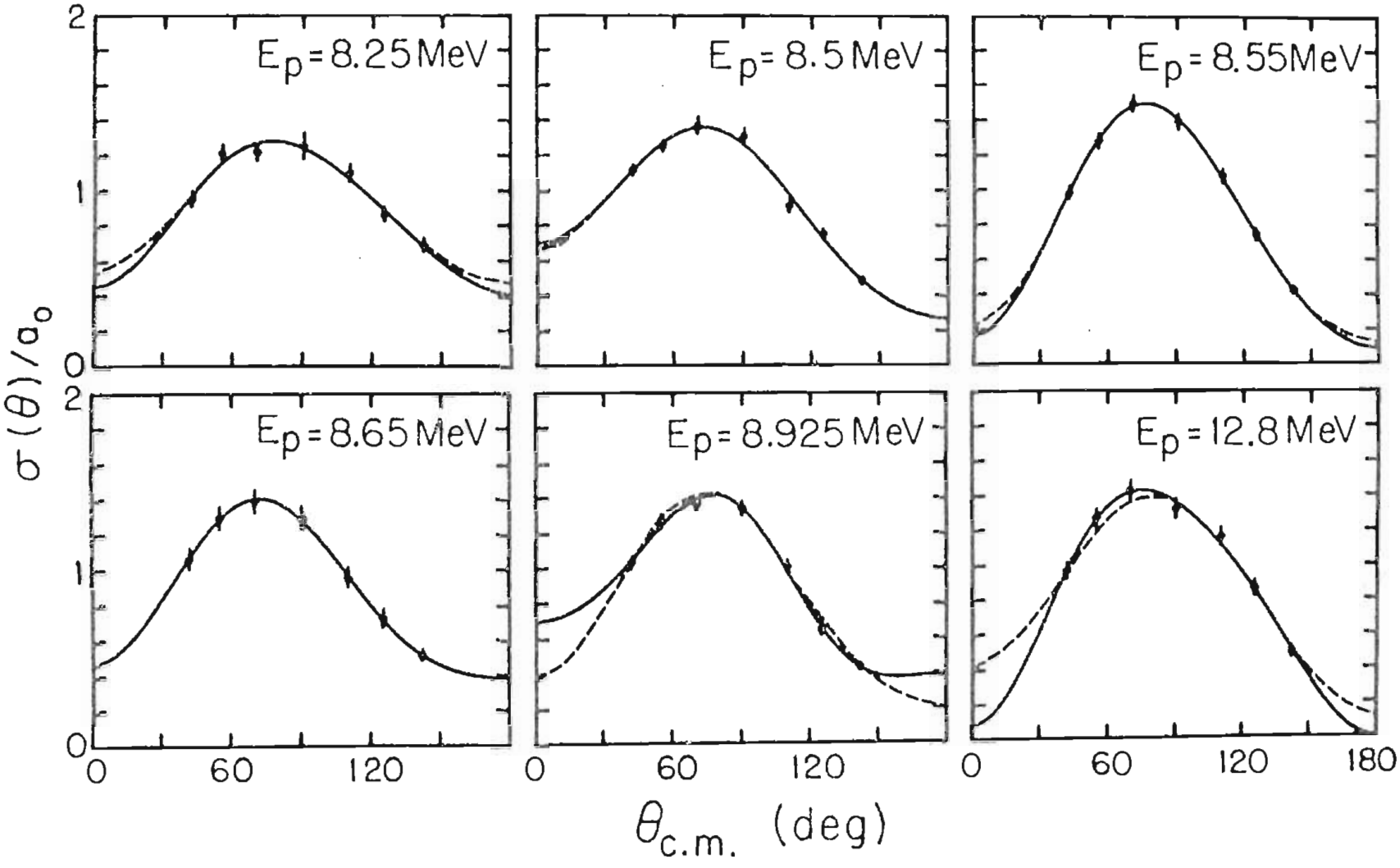
E_p = 8.25 MeV
E_p = 8.5 MeV
E_p = 8.55 MeV
E_p = 8.65 MeV
E_p = 8.925 MeV
E_p = 12.8 MeV
$\sigma(\theta)/a_0$
$\theta_{c.m.}$ (deg)
0
1
2
60
120
180

include the statistical error of the data and the possible error in the beam polarization. In addition, the expression for $A(\theta)$ was corrected for those cases where the polarization of the spin up and spin down beams were not the same.

The angular distributions of cross section may be described by a linear least squares fit to Legendre polynomials where

$$\sigma(\theta) = \sum_k a_k Q_k P_k(\cos\theta)$$

The geometrical correction factors, Q_k, are due to the finite detector size. The center of mass corrections and the statistical errors have been included in the fit. Fits were made including all polynomials up to P_4, shown by the solid curves in the figures, and up to P_3, as shown by the dashed curves. The a_k coefficients, normalized by dividing by a_o, are given in Table II along with the chi-square per degree of freedom and the probability of exceeding chi-square. The normalized a coefficients for the fits through P_4 are shown plotted in fig. 12. The coefficients for the fits through P_3 are not shown, but are within the error bars of the coefficients that are shown.

The angular distributions of analyzing power may be described by a linear least squares fit to the associated Legendre polynomials where

$$\frac{\sigma(\theta) A(\theta)}{a_o} = \sum_k b_k Q_k P_k'(\cos\theta)$$

Figure 12. The a_k coefficients for the $^{30}Si(p,\gamma_0)^{31}P$ reaction obtained from fitting the data shown in figs. 9, 10, and 11. The error bars represent the statistical errors. Only the coefficients obtained from the fourth order fits are shown. The set of coefficients obtained from the third order fits fall within the error bars shown. The coefficients are tabulated in Table II.

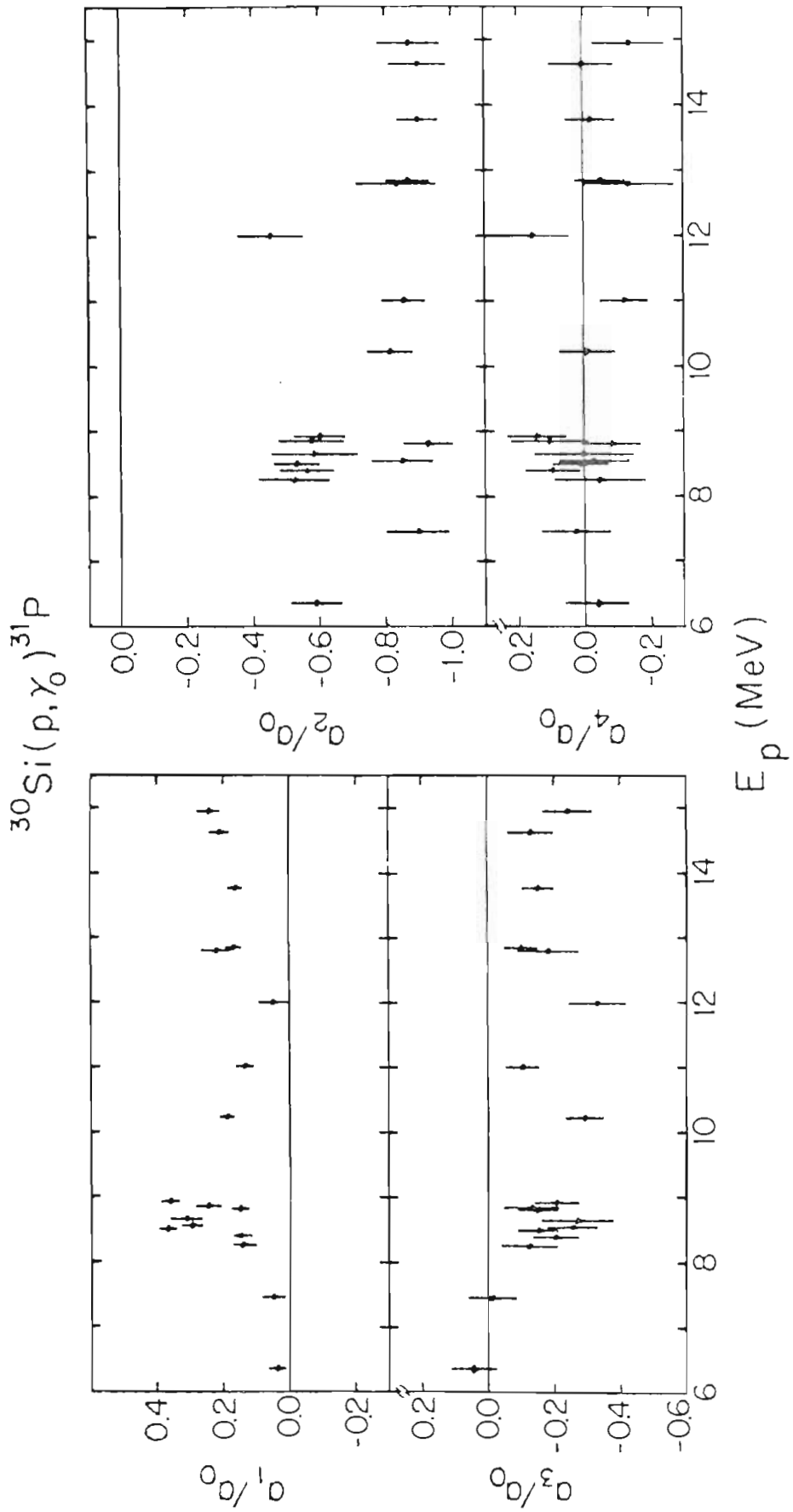
$^{30}Si(p,\gamma_0)^{31}P$
E_p (MeV)
a_1/a_0
a_2/a_0
a_3/a_0
a_4/a_0

Table II. The a_k coefficients for the $^{30}Si(p,\gamma_0)^{31}P$ reaction. For each energy, the coefficients obtained from the fourth order fits are given on the first line, and the coefficients from the third order fits are given on the second line.

E_p(MeV)	a_1	a_2	a_3	a_4	χ^2	P
6.36	0.04±0.03	-0.59±0.08	0.05±0.07	-0.05±0.10	1.10	0.33
6.36	0.04±0.03	-0.56±0.04	0.06±0.06		0.80	0.49
7.46	0.05±0.04	-0.90±0.09	-0.02±0.07	0.03±0.10	0.60	0.55
7.46	0.05±0.03	-0.92±0.05	-0.02±0.07		0.42	0.74
8.25	0.14±0.04	-0.52±0.11	-0.13±0.09	-0.05±0.14	1.64	0.19
8.25	0.15±0.04	-0.49±0.06	-0.11±0.08		1.14	0.33
8.4	0.15±0.04	-0.56±0.08	-0.21±0.07	0.10±0.08	0.59	0.55
8.4	0.13±0.03	-0.64±0.05	-0.23±0.07		0.82	0.48
8.5	0.37±0.03	-0.53±0.07	-0.15±0.06	0.01±0.09	2.52	0.08
8.5	0.37±0.03	-0.54±0.04	-0.16±0.06		1.69	0.17
8.55	0.29±0.03	-0.85±0.09	-0.26±0.08	-0.03±0.11	0.20	0.82
8.55	0.30±0.03	-0.83±0.05	-0.25±0.07		0.16	0.92
8.65	0.31±0.05	-0.58±0.13	-0.27±0.11	0.00±0.15	0.08	0.92
8.65	0.31±0.04	-0.59±0.07	-0.27±0.10		0.05	0.98
8.81	0.15±0.03	-0.93±0.07	-0.15±0.06	-0.03±0.09	0.86	0.43
8.81	0.16±0.02	-0.87±0.04	-0.13±0.05		1.16	0.32
8.85	0.25±0.04	-0.58±0.10	-0.13±0.09	0.10±0.12	1.43	0.24
8.85	0.23±0.03	-0.65±0.06	-0.17±0.08		1.21	0.31

Table II. (continued)

E_p (MeV)	a_1	a_2	a_3	a_4	χ^2	P
8.925	0.36±0.03	-0.60±0.08	-0.21±0.07	0.14±0.09	0.90	0.41
8.925	0.34±0.03	-0.71±0.05	-0.26±0.06		1.41	0.24
10.225	0.19±0.02	-0.82±0.07	-0.29±0.06	-0.01±0.08	1.86	0.16
10.225	0.19±0.02	-0.81±0.03	-0.29±0.05		1.24	0.29
11.01	0.13±0.03	-0.86±0.07	-0.11±0.05	-0.12±0.07	2.22	0.11
11.01	0.15±0.02	-0.76±0.03	-0.07±0.05		2.43	0.06
12.0	0.05±0.04	-0.45±0.10	-0.33±0.08	0.16±0.11	0.37	0.69
12.0	0.03±0.04	-0.57±0.06	-0.38±0.08		0.85	0.47
12.8	0.22±0.04	-0.84±0.12	-0.18±0.10	-0.14±0.14	0.69	0.50
12.8	0.25±0.04	-0.73±0.06	-0.10±0.08		1.10	0.35
12.85	0.17±0.02	-0.87±0.07	-0.10±0.05	-0.05±0.08	0.10	0.90
12.85	0.17±0.02	-0.83±0.03	-0.09±0.05		0.23	0.87
13.775	0.16±0.02	-0.90±0.06	-0.15±0.05	-0.02±0.08	2.64	0.07
13.775	0.16±0.02	-0.89±0.03	-0.15±0.05		1.79	0.15
14.625	0.21±0.03	-0.90±0.09	-0.13±0.07	0.01±0.10	3.14	0.04
14.625	0.21±0.03	-0.91±0.05	-0.13±0.06		2.10	0.10
14.95	0.24±0.03	-0.87±0.10	-0.24±0.08	-0.14±0.11	1.49	0.23
14.95	0.27±0.03	-0.78±0.05	-0.17±0.07		2.29	0.08

As before, the geometrical correction factors, center of mass corrections, and statistical errors were taken into account. The fits including all polynomials up to P_4^1 are indicated by the solid lines in the figures while the fits through P_3^1 are represented by the dashed lines. The b_K coefficients are given in Table III and those for the fits through P_4^1 are plotted in fig. 12. The coefficients for the fits through P_3^1 are not plotted but are within the error bars of those shown.

In general, fits to polynomials of order larger than four were not statistically justified by the data (using the normalized chi-square and probability of exceeding chi-square as the statistical criteria). Such high order contributions could only come from radiation of multipolarity higher than two, so their absence is not surprising. However, the statistical criteria does not clearly indicate whether or not P_4 or P_4^1 need to be included in the fits. The analysis of these results must therefore be done with these ambiguities in mind.

Glavish et al. (1974) have made studies of the reaction $^{31}P(\vec{p},\gamma_o)^{32}S$ with a phosphine gas target. The energy spread from the target washed out the fine structure observed by Dearnaley et al. and discussed in the previous chapter. The results of their polarized beam measurements are shown together with the results for this work in fig. 14. The dashed lines are those of Glavish et al. for ^{32}S, while the points show the data of figs. 12 and 13 on a more compressed scale. The dashed lines are seen to be basically symmetric about 17.5 MeV excita-

Figure 12. The b_k coefficients for the $^{30}Si(p,\gamma_0)^{31}P$ reaction obtained from fitting the data shown in figs. 9 and 10. The error bars represent the statistical errors. Only the coefficients obtained from the fourth order fits are shown. The set of coefficients obtained from the third order fits fall within the error bars shown. The coefficients are tabulated in Table III.

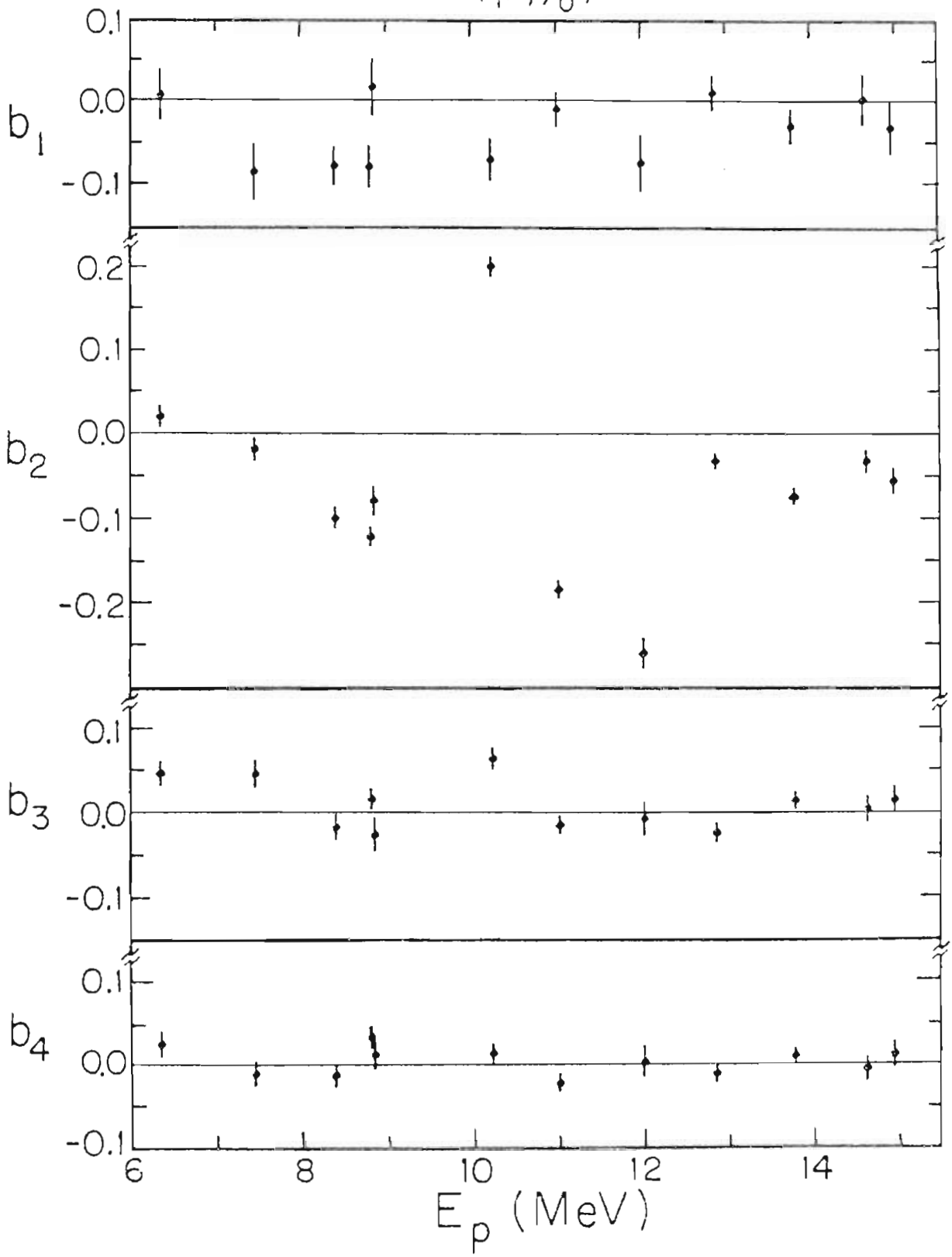
$^{30}Si(p,\gamma_0)^{31}P$
b_1
b_2
b_3
b_4
0.1
0.0
-0.1
0.2
-0.2
6
8
10
12
14
E_p (MeV)

Table III. The b_k coefficients for the $^{30}Si(p,\gamma_0)^{31}P$ reaction. For each energy, the coefficients obtained from the fourth order fits are given on the first line, and the coefficients from the third order fits are given on the second line.

E (MeV)	b_1	b_2	b_3	b_4	χ^2	P
6.36	0.01±0.03	0.02±0.01	0.05±0.01	0.03±0.01	2.19	0.09
6.36	0.02±0.03	0.04±0.01	0.04±0.01		2.39	0.05
7.46	-0.08±0.03	-0.02±0.01	0.05±0.02	-0.01±0.01	0.21	0.89
7.46	-0.09±0.03	-0.02±0.01	0.05±0.02		0.31	0.87
8.4	-0.08±0.02	-0.10±0.01	-0.02±0.01	-0.01±0.01	0.53	0.66
8.4	-0.08±0.02	-0.10±0.01	-0.01±0.01		0.66	0.62
8.81	-0.08±0.03	-0.12±0.01	0.02±0.01	0.03±0.01	1.72	0.16
8.81	-0.06±0.02	-0.11±0.01	0.00±0.01		3.09	0.01
8.85	0.02±0.03	-0.08±0.02	-0.03±0.02	0.01±0.02	1.54	0.20
8.85	0.02±0.03	-0.07±0.02	-0.03±0.01		1.29	0.27
10.225	-0.07±0.02	0.20±0.01	0.07±0.01	0.01±0.01	0.59	0.82
10.225	-0.06±0.02	0.21±0.01	0.06±0.01		0.81	0.52
11.01	-0.01±0.02	-0.18±0.01	-0.01±0.01	-0.02±0.01	0.92	0.43
11.01	-0.01±0.02	-0.19±0.01	-0.01±0.01		1.72	0.14

Table III. (continued)

E_p (MeV)	b_1	b_2	b_3	b_4	χ^2	P
12.0	-0.07±0.03	-0.26±0.02	-0.01±0.02	0.00±0.02	1.13	0.33
12.0	-0.07±0.03	-0.26±0.02	-0.01±0.02		0.86	0.49
12.85	0.01±0.02	-0.03±0.01	-0.02±0.01	-0.01±0.01	0.55	0.65
12.85	0.01±0.02	-0.03±0.01	-0.02±0.01		0.73	0.57
13.775	-0.03±0.02	-0.07±0.01	0.02±0.01	0.01±0.01	1.35	0.26
13.775	-0.02±0.02	-0.07±0.01	0.01±0.01		1.29	0.27
14.625	0.01±0.03	-0.03±0.01	0.01±0.02	-0.01±0.01	0.64	0.59
14.625	0.00±0.03	-0.03±0.01	0.01±0.01		0.52	0.72
14.95	-0.03±0.03	-0.05±0.02	0.02±0.02	0.01±0.02	0.52	0.67
14.95	-0.02±0.03	-0.05±0.01	0.01±0.01		0.56	0.69

Figure 14. A comparison of the a_k and b_k coefficients obtained from the angular distributions of the $^{30}Si(p,\gamma_0)^{31}P$ and $^{31}P(p,\gamma_0)^{32}S$ reactions. The points indicate the coefficients for the $^{30}Si(p,\gamma_0)^{31}P$ reactions as shown in figs. 12 and 13, but on a compressed scale. The dashed lines indicate the results of the measurements of the angular distributions of the reaction $^{31}P(p,\gamma_0)^{32}S$ (Glavish et al., 1974).

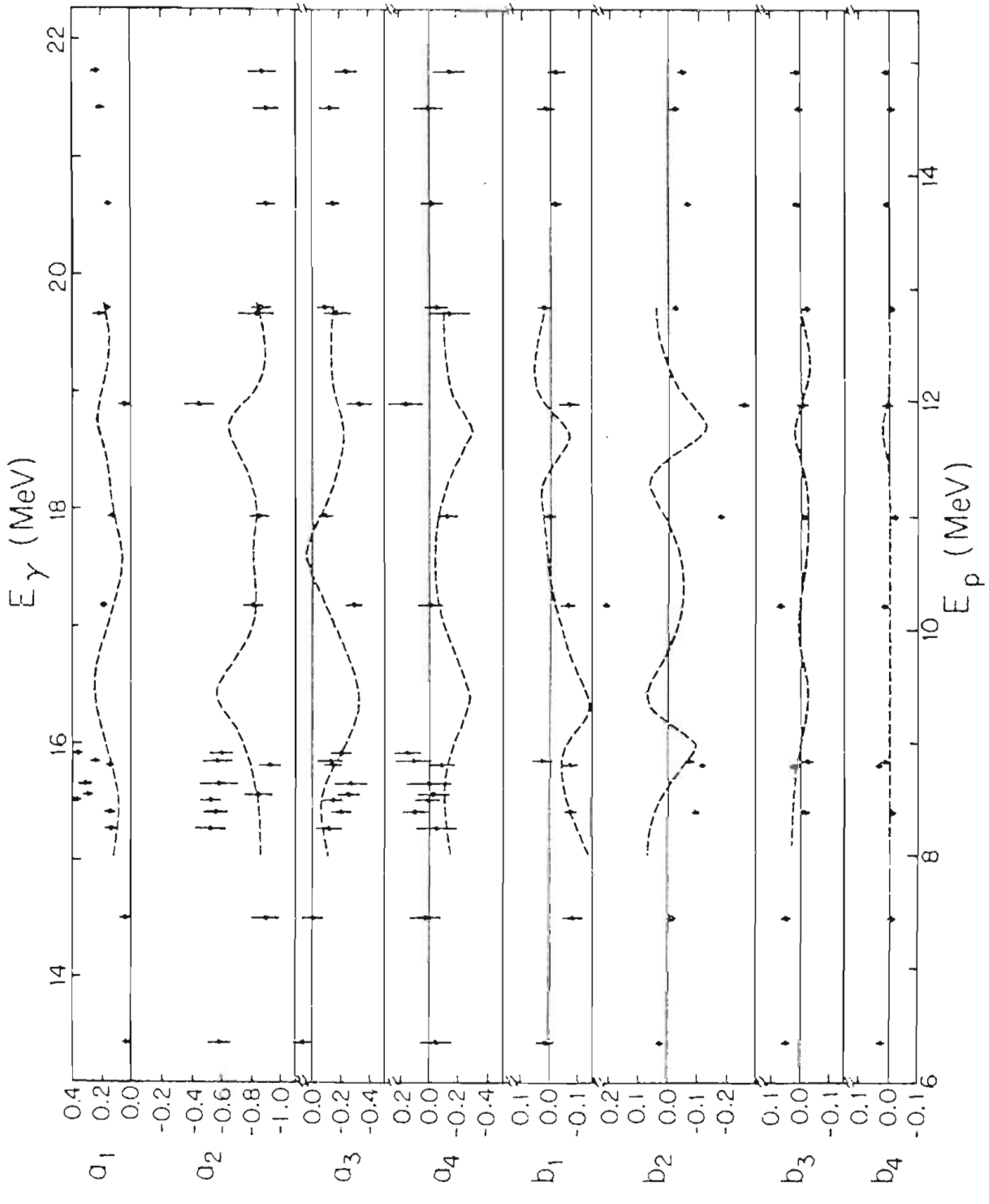
E_γ (MeV)
E_p (MeV)
a_1
a_2
a_3
a_4
b_1
b_2
b_3
b_4

tion, with the exception of b_1 and b_3, which are antisymmetric. The results for the two reactions appear to be similar in trend, with the possible exception of b_2 at 10.225 MeV proton energy. As may be seen in fig. 10, the analyzing power for this peak in the cross section is opposite in sign to the others observed for the $^{30}Si(p,\gamma_0)^{31}P$ reaction. This peak at 17.2 MeV excitation also seems to appear in both the 90° excitation functions for $^{31}P(\gamma,p_0)^{30}P$ and $^{31}P(p,\gamma_0)^{32}S$; however, no angular distribution was measured at that energy by Glavish et al. The results of this comparison suggest that the structure of the giant resonances of ^{31}P and ^{32}S are quite similar. This may imply that the giant resonance of ^{31}P is basically the same as that of ^{32}S, but with a spectator $s_{1/2}$ hole.

Another quantity of interest in these experiments is the fore-aft asymmetry

$$A = \frac{\sigma(55°) - \sigma(125°)}{2\,P_1(\cos 55°)} = A_1 - 0.67A_3$$

where 55° and 125° are the zeroes of $P_2(\cos\theta)$. This quantity is indicative of the E1-E2 (or E1-M1) interference, as will be discussed later. The fore-aft asymmetry, A, and the normalized fore-aft asymmetry $a=A/A_0$, as well as A_0 (the total cross section $\sigma=4\pi A_0$) are shown in fig. 15 and are tabulated in Table IV. For the seven point angular distributions, A and A_0 were obtained from the fits. The angular distributions of cross

Figure 15. The fore-aft asymmetry, A; normalized asymmetry A/A_o; and the total cross section, A_o; obtained from angular distributions of the $^{30}Si(p,\gamma_0)^{31}P$ reaction, as described in the text. The error bars indicate the statistical error associated with the data.

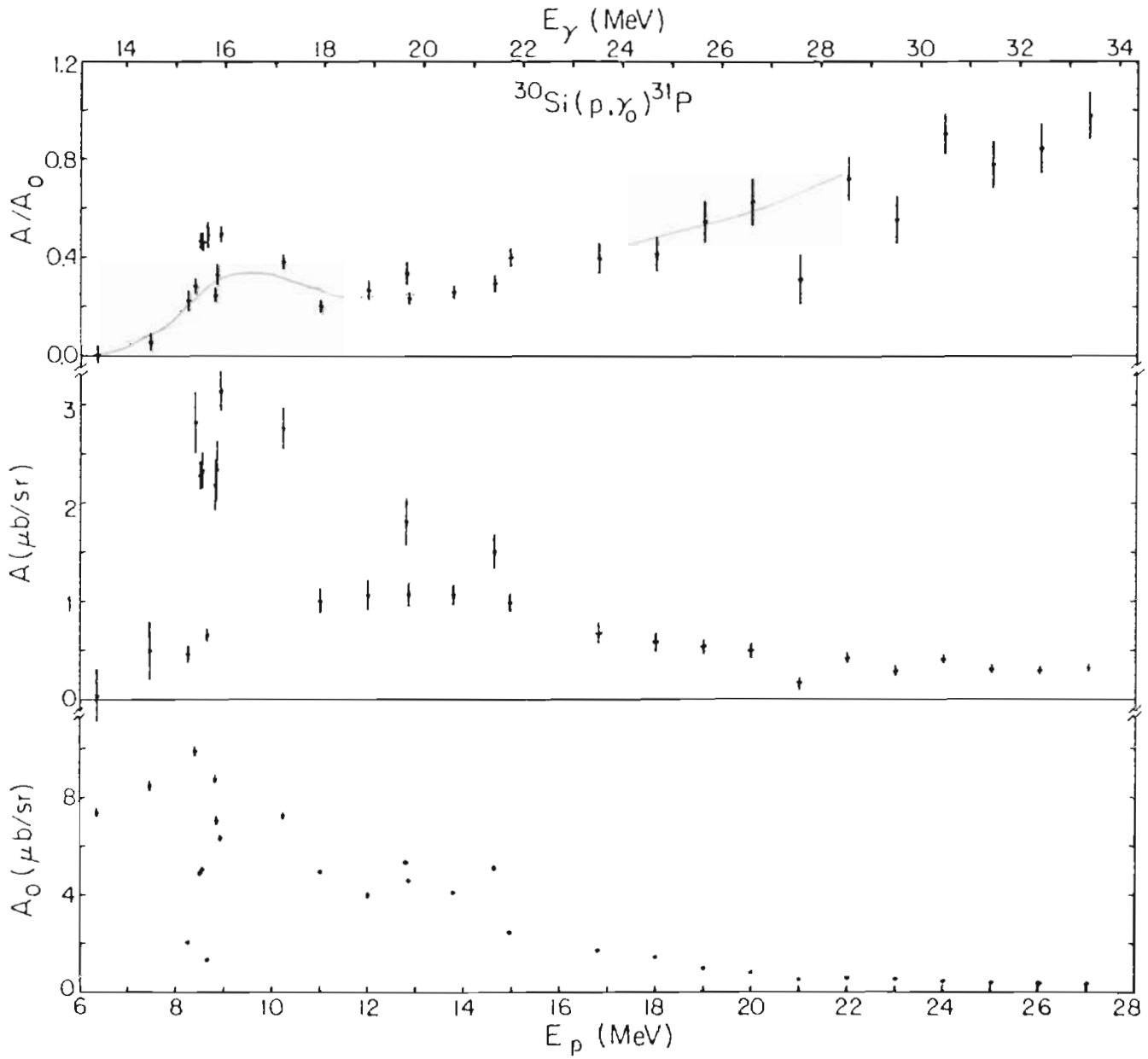
E_γ (MeV)
14 16 18 20 22 24 26 28 30 32 34
$^{30}Si(p,\gamma_0)^{31}P$
A/A_0
1.2
0.8
0.4
0.0
$A\ (\mu b/sr)$
3
2
1
0
$A_0\ (\mu b/sr)$
8
4
0
6 8 10 12 14 16 18 20 22 24 26 28
E_p (MeV)

Table IV. The total cross section A_o; the fore-aft asymmetry, A; and the normalized fore-aft asymmetry, A/A_o for the $^{30}Si(p,\gamma_o)^{31}P$ reaction.

E_p (MeV)	A_o (μb)	A (μb)	A/A_o
6.36	7.38±0.17	0.05±0.27	0.01±0.04
7.46	8.48±0.22	0.50±0.30	0.06±0.04
8.25	2.06±0.07	0.47±0.09	0.23±0.04
8.4	9.98±0.21	2.83±0.31	0.29±0.03
8.5	4.87±0.11	2.29±0.14	0.47±0.03
8.55	5.04±0.12	2.34±0.19	0.47±0.04
8.65	1.34±0.05	0.66±0.07	0.49±0.05
8.81	8.75±0.17	2.19±0.26	0.25±0.03
8.85	7.04±0.20	2.35±0.29	0.33±0.04
8.925	6.32±0.14	3.15±0.20	0.50±0.03
10.225	7.23±0.13	2.77±0.21	0.38±0.03
11.01	4.94±0.08	1.01±0.12	0.20±0.03
12.0	3.97±0.11	1.07±0.16	0.27±0.04
12.8	5.30±0.16	1.80±0.24	0.34±0.05
12.85	4.57±0.08	1.07±0.12	0.24±0.03
13.775	4.10±0.07	1.07±0.10	0.26±0.03
14.625	5.10±0.12	1.51±0.17	0.30±0.03
14.95	2.46±0.06	0.99±0.09	0.40±0.04

Table IV. (continued)

E_p (MeV)	A_o (μb)	A (μb)	A/A_o
16.8	1.68±0.06	0.67±0.11	0.40±0.06
18.0	1.39±0.06	0.58±0.10	0.42±0.07
19.0	0.95±0.05	0.52±0.08	0.55±0.08
20.0	0.77±0.05	0.49±0.08	0.63±0.10
21.0	0.51±0.03	0.16±0.05	0.32±0.10
22.0	0.57±0.03	0.41±0.05	0.73±0.09
23.0	0.50±0.03	0.28±0.05	0.56±0.10
24.0	0.44±0.03	0.40±0.05	0.91±0.08
25.0	0.39±0.03	0.30±0.04	0.78±0.10
26.0	0.34±0.03	0.29±0.04	0.85±0.10
27.0	0.32±0.02	0.31±0.04	0.98±0.10

section were observed at three angles, 55°, 90°, and 125° at 16.8 MeV and in 1 MeV steps from 17 to 27 MeV incident proton energy. For these energies, A was obtained directly from the 55° and 125° data, while A_0 was obtained by assuming that a_4 was zero. Then,

$$A_0 = \frac{\sigma(55°) + \sigma(125°)}{2}$$

As discussed in Chapter III, the yield from γ_0 becomes much smaller than the yield from γ_1 at higher energies and becomes difficult to extract reliably, thus the γ_0 data may contain systematic errors which may exceed the error bars above 19 MeV proton energy.

The angular distributions of the $^{30}Si(p,\gamma_1)^{31}P$ reaction were also observed at these same energies. The energies studied, however, usually corresponded to a peak in the 90° cross section of γ_0. Since the γ_1 cross section tends to be smaller than the γ_0 cross section below 9 MeV proton energy, the yield could be reliably extracted at only two of the lower energies. The angular distributions observed for γ_1 are shown in figs. 16 and 17.

The angular distributions were fit as described for γ_0, however, the statistical criteria indicated that the inclusion of P_4 was not justified and only the fit through P_3 is shown. The statistical criteria again did not clearly indicate whether or not the inclusion of P_4 was justified. The fits through P_4 are those shown. Only a simple analysis may be applied for γ_1,

Figure 16. Angular distributions of cross section and analyzing power from the $^{30}Si(p,\gamma_1)^{31}P$ reaction for incident proton energies of 8.25, 8.65, 10.225, 11.01, 12.0, and 12.8 MeV. The error bars represent the statistical error associated with the data points. The solid curves indicate the fits to the data including all polynomials up to order 3 for the cross section fits, and up to order 4 for the fits to the analyzing power.

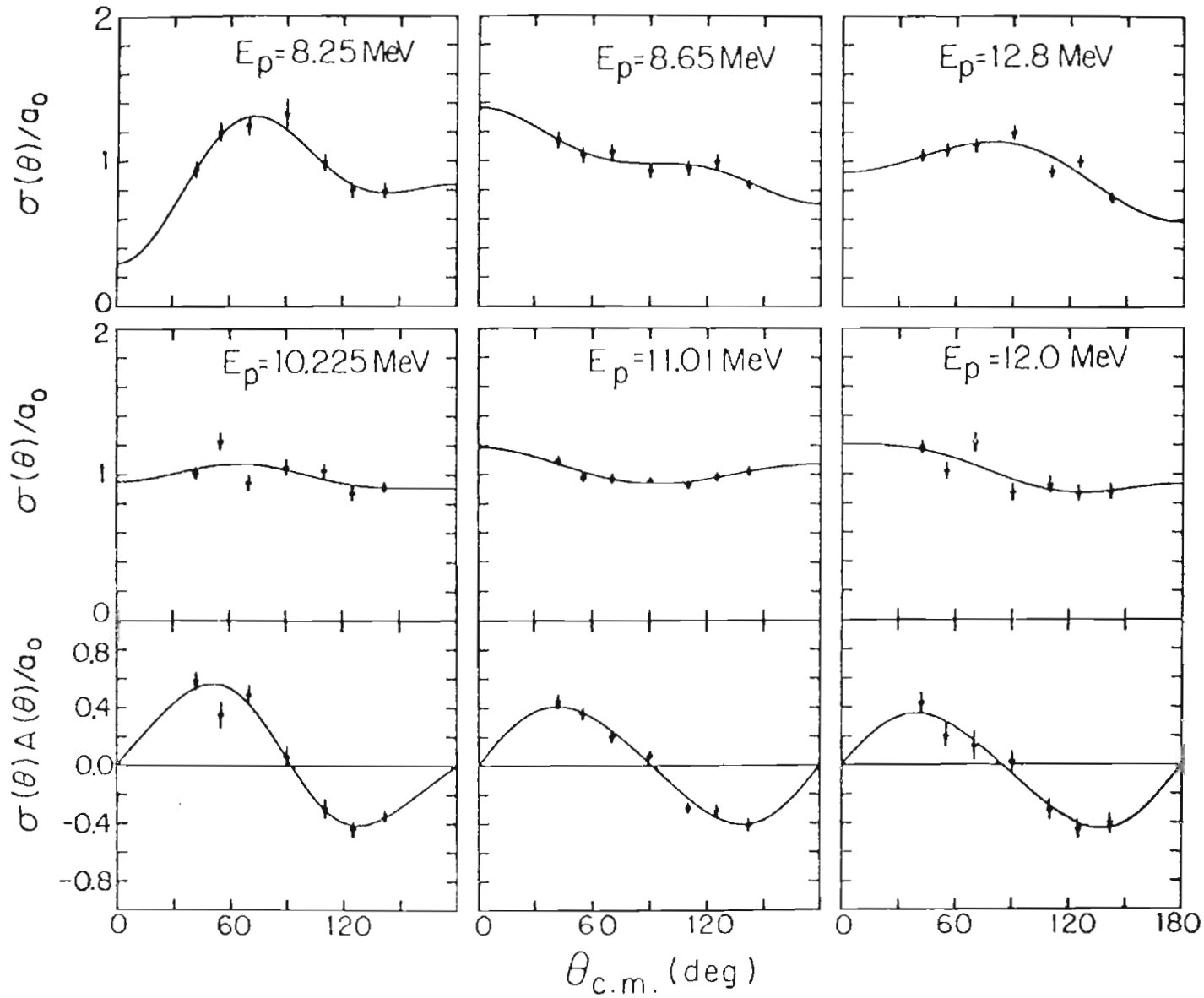
E_p=8.25 MeV
E_p=8.65 MeV
E_p=12.8 MeV
E_p=10.225 MeV
E_p=11.01 MeV
E_p=12.0 MeV
$\sigma(\theta)/a_0$
$\sigma(\theta)A(\theta)/a_0$
$\theta_{c.m.}$ (deg)
0
60
120
180
2
1
0
0.8
0.4
0.0
-0.4
-0.8

Figure 17. Angular distributions of cross section and analyzing power from the $^{30}Si(p,\gamma_0)^{31}P$ reaction for incident proton energies of 12.85, 13.775, 14.625, and 14.95 MeV. The error bars represent the statistical error associated with the data points. The solid curves indicate the fits to the data including all polynomials up to order 3 for the cross section fits, and up to order 4 for the fits to the analyzing power.

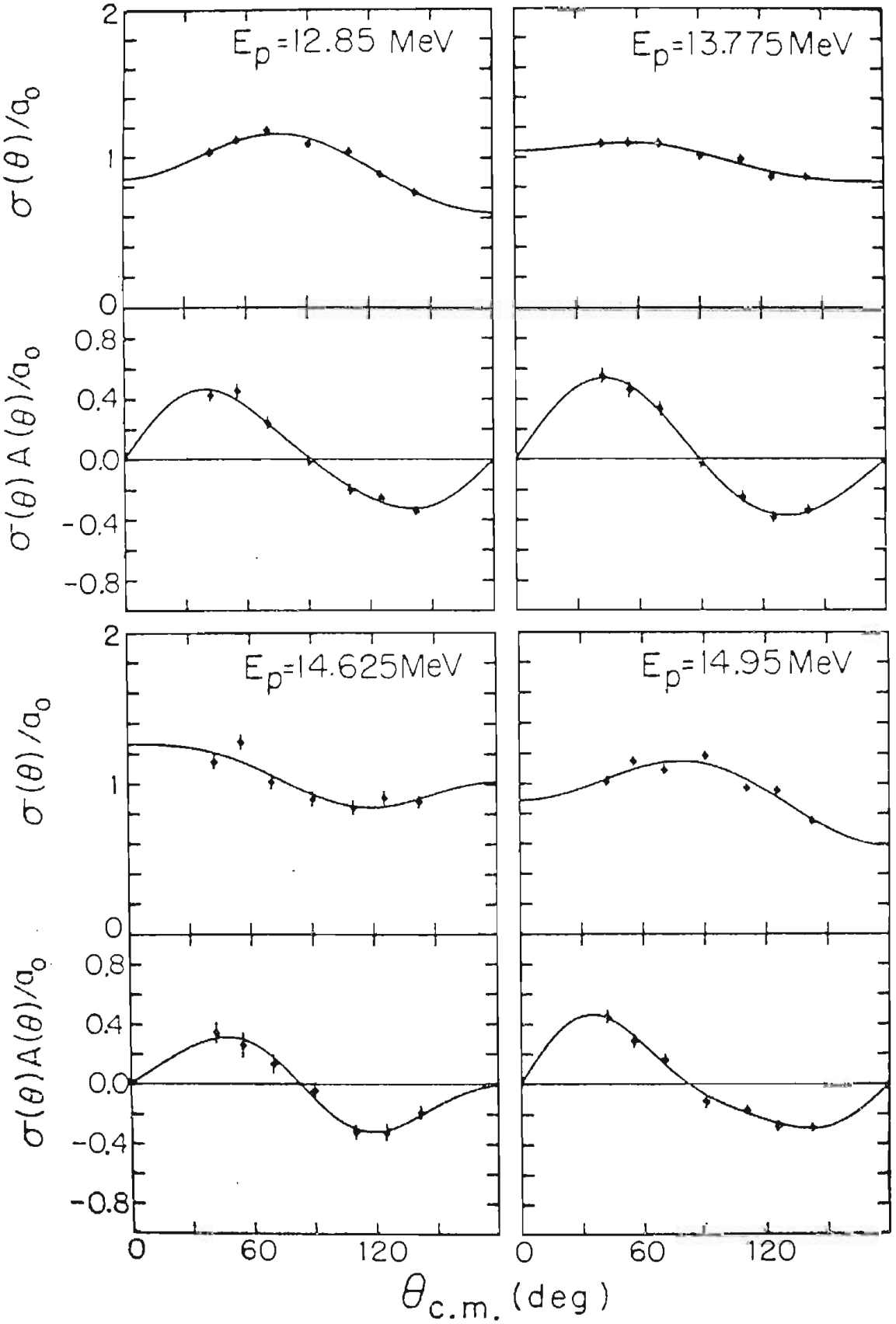
E_p=12.85 MeV
E_p=13.775MeV
E_p=14.625MeV
E_p=14.95 MeV
$\sigma(\theta)/a_0$
$\sigma(\theta)A(\theta)/a_0$
2
1
0
0.8
0.4
0.0
-0.4
-0.8
0
60
120
$\theta_{c.m.}$ (deg)

however, so this ambiguity will not be important in the analysis. The values of the a_k and b_k coefficients are given in Tables V and VI, respectively, and are plotted in figure 18. While the angular distributions of cross section are observed to be much flatter than those for γ_0, the analyzing powers are in general larger. This result will be discussed in the next section.

The fore-aft asymmetry is again of interest and will be discussed in detail in Chapter VI. The results are shown in fig. 19 and tabulated in Table VII.

B. Transition Matrix Analysis

With the use of polarized beams has come the possibility of obtaining more detailed structural information about the giant dipole resonance region. Specifically, the angular distributions of cross section and analyzing power may be expressed in terms of transition matrix elements (Glavish, 1973). The radiative capture of a particle and the subsequent decay by gamma ray emmission is described schematically in the j-representation by the following picture:

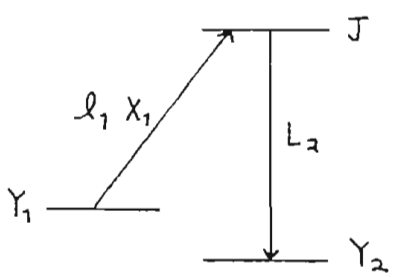

Figure 18. The a_k and b_k coefficients for the $^{30}Si(p,\gamma_1)^{31}P$ reaction obtained from fitting the data shown in figs. 16 and 17. The error bars represent the statistical errors. The coefficients are tabulated in Tables V and VI.

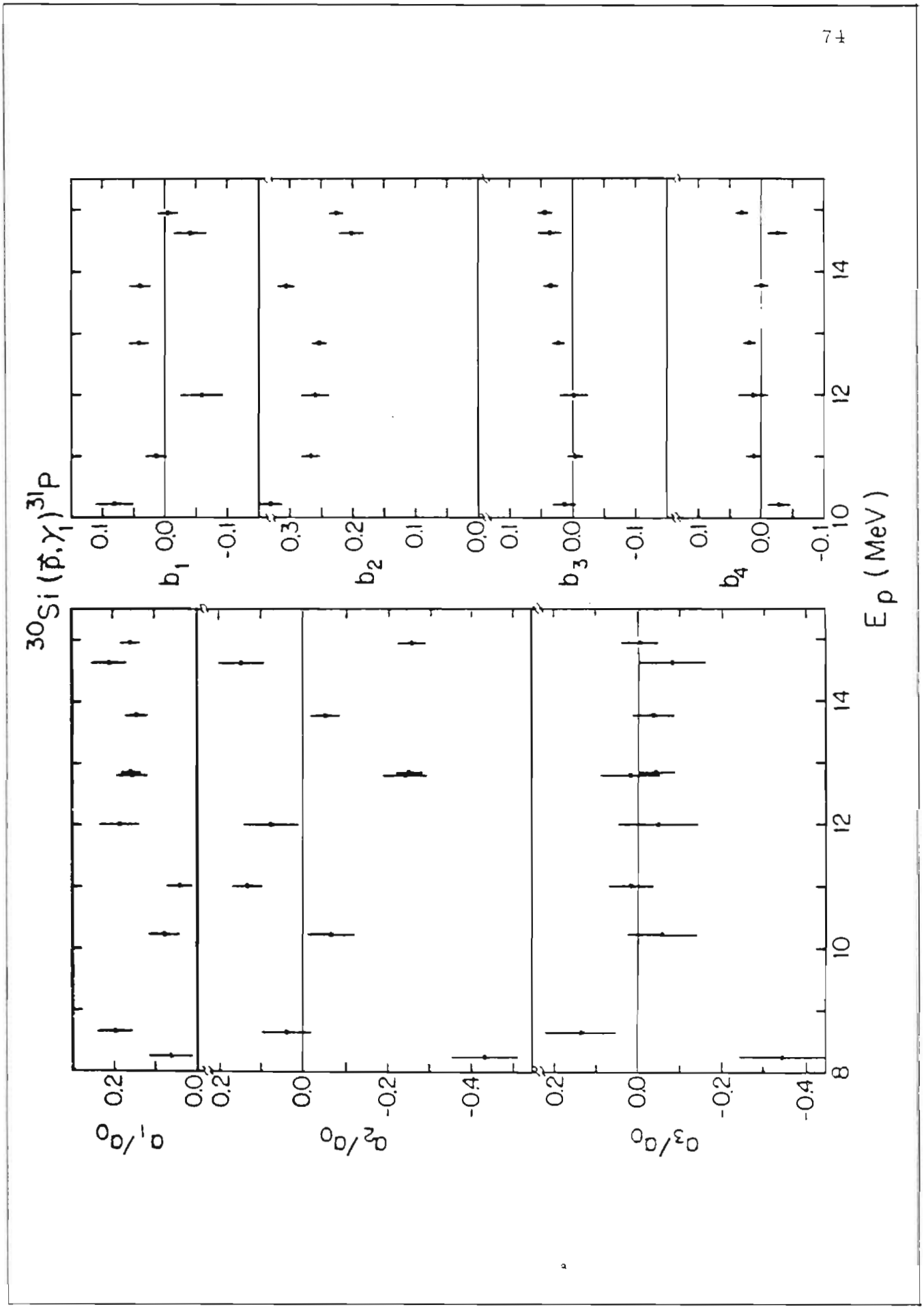
$^{30}Si(\vec{p},\gamma_1)^{31}P$
b_1
b_2
b_3
b_4
a_1/a_0
a_2/a_0
a_3/a_0
E_p (MeV)

Table V. The a_k coefficients for the $^{30}Si(p,\gamma_1)^{31}P$ reaction.

E_p(MeV)	a_1	a_2	a_3	χ^2	P
8.25	0.07±0.05	-0.44±0.08	-0.35±0.10	1.01	0.39
8.65	0.20±0.04	0.04±0.06	0.14±0.08	1.34	0.26
10.225	0.08±0.04	-0.07±0.06	-0.06±0.08	5.35	0.00
11.01	0.04±0.03	0.13±0.04	0.01±0.05	1.06	0.01
12.0	0.19±0.05	0.07±0.07	-0.05±0.10	4.06	0.01
12.8	0.16±0.04	-0.25±0.05	0.02±0.07	4.34	0.01
12.85	0.16±0.02	-0.26±0.03	-0.05±0.04	1.66	0.17
13.775	0.15±0.03	-0.06±0.03	-0.04±0.05	1.21	0.30
14.625	0.21±0.04	0.14±0.05	-0.09±0.08	3.77	0.01
14.95	0.16±0.02	-0.27±0.03	-0.01±0.04	6.93	0.00

Table VI. The b_k coefficients for the $^{30}Si(p,\gamma_1)^{31}P$ reaction.

E_p(MeV)	b_1	b_2	b_3	b_4	χ^2	P
10.225	0.08±0.03	0.33±0.02	0.01±0.02	-0.03±0.02	2.41	0.07
11.01	0.01±0.02	0.27±0.01	0.00±0.01	0.01±0.01	3.68	0.01
12.0	-0.06±0.03	0.26±0.02	0.00±0.02	0.01±0.02	1.70	0.16
12.85	0.04±0.02	0.25±0.01	0.02±0.01	0.02±0.01	1.81	0.14
13.775	0.04±0.02	0.31±0.01	0.03±0.01	0.00±0.01	0.66	0.58
14.625	-0.04±0.03	0.20±0.02	0.04±0.02	-0.03±0.02	0.83	0.48
14.95	-0.01±0.02	0.23±0.01	0.04±0.01	0.03±0.01	1.19	0.31

Figure 16. The fore-aft asymmetry, A; normalized asymmetry A/A_o; and the total cross section, A_o; obtained from angular distributions of the $^{30}Si(p,\gamma_1)^{31}P$ reaction, as described in the text. The error bars indicate the statistical error associated with the data.

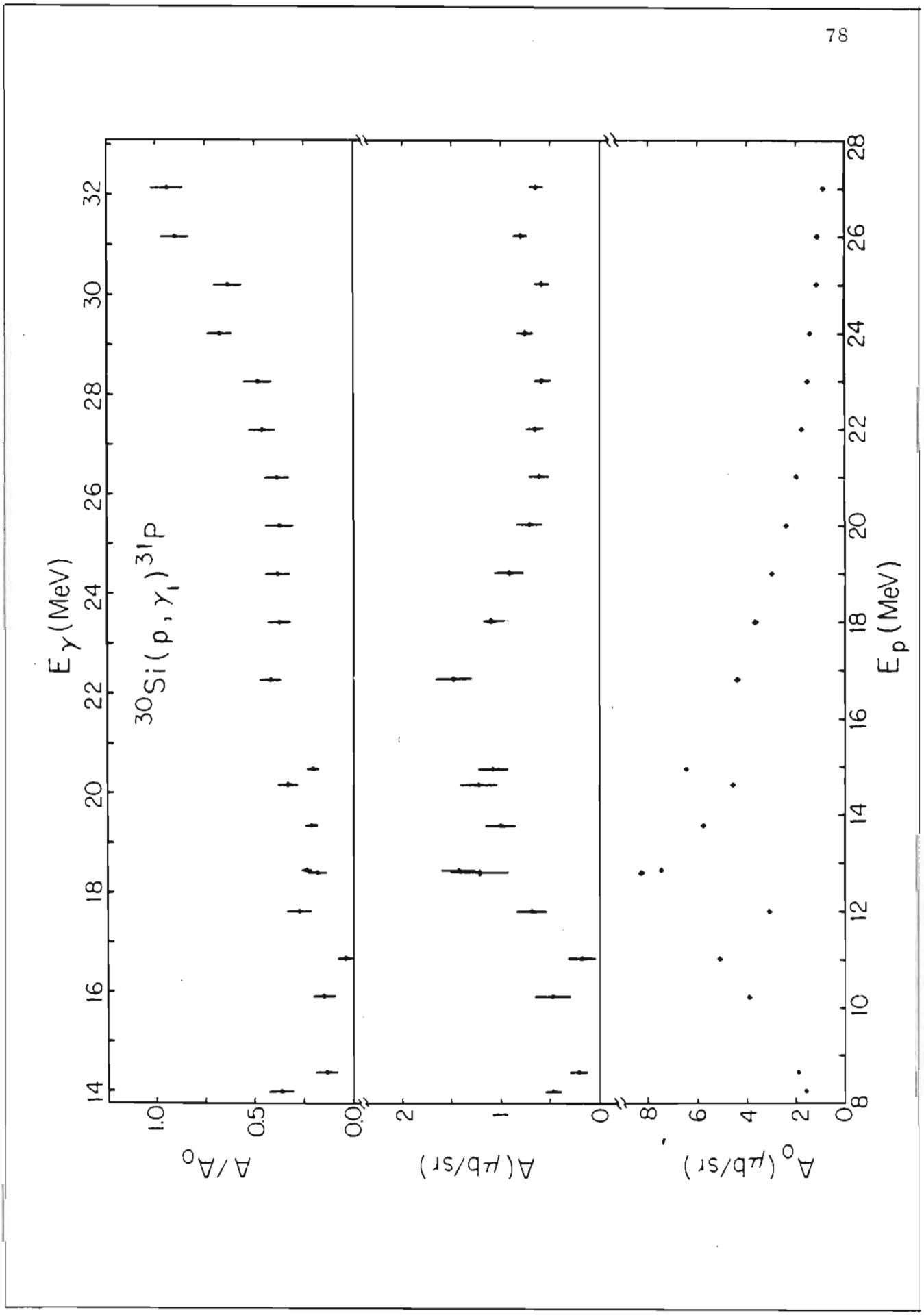
$^{30}Si(p,\gamma_1)^{31}P$
E_γ(MeV)
E_p(MeV)
A/A_0
$A(\mu b/sr)$
$A_0(\mu b/sr)$

Table VII. The total cross section A_o; the fore-aft asymmetry, A; and the normalized fore-aft asymmetry, A/A_o for the $^{30}Si(p,\gamma_1)^{31}P$ reaction.

E_p (MeV)	A_o (μb)	A (μb)	A/A_o
8.25	1.59±0.04	0.47±0.08	0.30±0.05
8.65	1.92±0.04	0.21±0.09	0.11±0.04
10.225	3.94±0.07	0.48±0.18	0.12±0.05
11.01	5.14±0.06	0.18±0.14	0.04±0.03
12.0	3.10±0.06	0.69±0.15	0.22±0.05
12.8	8.24±0.13	1.22±0.31	0.15±0.04
12.85	7.51±0.08	1.44±0.17	0.19±0.02
13.775	5.80±0.07	1.00±0.15	0.17±0.03
14.625	4.59±0.08	1.23±0.18	0.27±0.04
14.95	6.49±0.07	1.08±0.15	0.17±0.02
16.8	4.36±0.11	1.48±0.19	0.34±0.04
18.0	3.64±0.10	1.10±0.17	0.30±0.05
19.0	2.98±0.09	0.91±0.15	0.31±0.05
20.0	2.36±0.08	0.71±0.13	0.30±0.06
21.0	1.94±0.06	0.61±0.10	0.31±0.05
22.0	1.74±0.05	0.65±0.09	0.37±0.05
23.0	1.47±0.05	0.57±0.09	0.39±0.06
24.0	1.37±0.04	0.74±0.08	0.54±0.05
25.0	1.12±0.04	0.57±0.07	0.51±0.06
26.0	1.10±0.04	0.80±0.07	0.72±0.06
27.0	0.84±0.04	0.63±0.06	0.76±0.07

where a particle of spin X_1 and orbital angular momentum l_1 is captured by a target nucleus with spin Y_1. The reaction proceeds through an intermediate state, described by the total angular momentum of the system, J, and a gamma ray of multipolarity L_2 is emitted in the decay to the final state with spin Y_2. The total angular momentum of the projectile is $L_1 = l_1 + X_1$. The transition matrix element enters as a reduced matrix element $R=\langle L_2 J \| T \| l_1 L_1 J \rangle$.

Since levels in the giant dipole resonance may be overlapping, it is necessary to include interference terms. An additional matrix element, $R'=\langle L_2' J' \| T' \| l_1' L_1' J' \rangle$ is described by a set of primed quantum numbers. The angular distribution of cross section, $\sigma(\theta)$, expressed in terms of the Legendre polynomials, $P_k(\cos\theta)$, is given by Glavish (1973):

$$\sigma(\theta) = \sum_{\alpha} (-)^{\rho} f \frac{1}{\hat{X}_1^2} \frac{1}{\hat{Y}_1^2} \hat{J} \hat{J}' \hat{L}_2 \hat{L}_2' \hat{L}_1 \hat{L}_1' \hat{l}_1 \hat{l}_1' \langle k0 | l_1 l_1' 00 \rangle$$

$$\times \langle k0 | L_2 L_2' 1-1 \rangle W(L_2 J L_2' J', Y_2 k) W(L_1 J L_1' J', Y_1 k)$$

$$\times W(l_1 L_1 l_1' L_1', X_1 k) P_k(\cos\theta) \mathrm{Re}(R R'^*)$$

where $\rho = L_1' - L_1 + l_1 + l_1' + Y_1 - Y_2 - X_1 - 1$. The summation α is performed over the following: l_1, l_1', L_1, L_1', J, J', L_2', L_2, and k. If R and R' both correspond to electric multipole transitions or both correspond to magnetic multipole transitions, then

$$f = \tfrac{1}{2}\left\{1 + (-)^{L_2 + L_2' + k}\right\} .$$

If one of the matrix elements corresponds to a magnetic transition and one to an electric transition,

$$f = \tfrac{1}{2}\left\{1 - (-)^{L_2 + L_2' + k}\right\} .$$

The notation

$$\hat{X}_1 = (2X_1 + 1)^{1/2}$$

is also used.

The product of analyzing power and cross section is expressed in terms of the associated Legendre polynomials, $P_k^1(\cos\theta)$, as follows:

$$A(\theta)\,\sigma(\theta) = \sum (-)^q f \frac{1}{\hat{Y}_1^2}\, \hat{J}^2 \hat{J}'^2 \hat{L}_2 \hat{L}_2' \hat{L}_1 \hat{L}_1' \hat{l}_1 \hat{l}_1'$$

$$\cdot \left\{\frac{3(2k+1)}{k(k+1)}\right\}^{1/2} \langle k1|k101\rangle \langle k0|l_1 l_1' 00\rangle \langle k0|L_2 L_2' 1{-1}\rangle$$

$$\cdot W(L_2 J L_2' J', Y_2 k)\, W(L_1 J L_1' J', Y_1 k)$$

$$\cdot \begin{Bmatrix} l_1 & X_1 & L_1 \\ l_1' & X_1 & L_1' \\ k & 1 & k \end{Bmatrix} P_k^1(\cos\theta)\, \mathrm{Im}(R R'^*) .$$

Here $q = l_1' + L_1' + Y_1 - Y_2 - 2X_1$ and the remaining notation is as described above.

As mentioned previously, the giant dipole resonance region

may be made up of overlapping levels, and it is the interference terms due to the overlapping of levels which give rise to the analyzing power observed in the reaction. It may be also possible for states of the same J^{π} to overlap. In such a case, the individual amplitudes may be summed together and represented mathematically by a single amplitude. Thus, while the coupling performed does not depend on a particular model, the transition matrix elements described above may not be directly comparable to the results of a model calculation.

While the presence of finite coefficients other than a_2 and b_2 implies the presence of radiation of multipolarity other than E1, it is worthwhile to first analyze the data in terms of pure E1 radiation which is expected to be the major component. Only l=1 capture leads to states in ^{31}P that may decay by E1 radiation to the $1/2^+$ ground state. From the formalism above,

$$a_0 = P_{1/2}^2 + 2P_{3/2}^2$$

$$a_2 = -P_{3/2}^2 - 2P_{1/2}P_{3/2}\cos(p_1 - p_3)$$

$$b_2 = -P_{1/2}P_{3/2}\sin(p_1 - p_3)$$

where p_1 and p_3 indicate the phases associated with the T-matrix amplitudes $P_{1/2}$ and $P_{3/2}$, respectively. The remaining coefficients are zero for pure E1 radiation. Using the experimental values of a_2 and b_2, these two equations may be solved directly for the amplitudes and relative phase, and the results are given in fig. 20 and in Table VIII. The amplitudes are

Figure 20. The solutions obtained from an E1 analysis of the $^{30}Si(p,\gamma_0)^{31}P$ reaction. The two solutions obtained using the values of a_2 and b_2 from the third order fits are shown on the left, and the two solutions obtained from the fourth order fits are shown on the right. The transition matrix amplitudes are expressed in terms of the percentage of the cross section due to each amplitude. The dashed lines indicate the relative phase obtained from an optical model calculation.

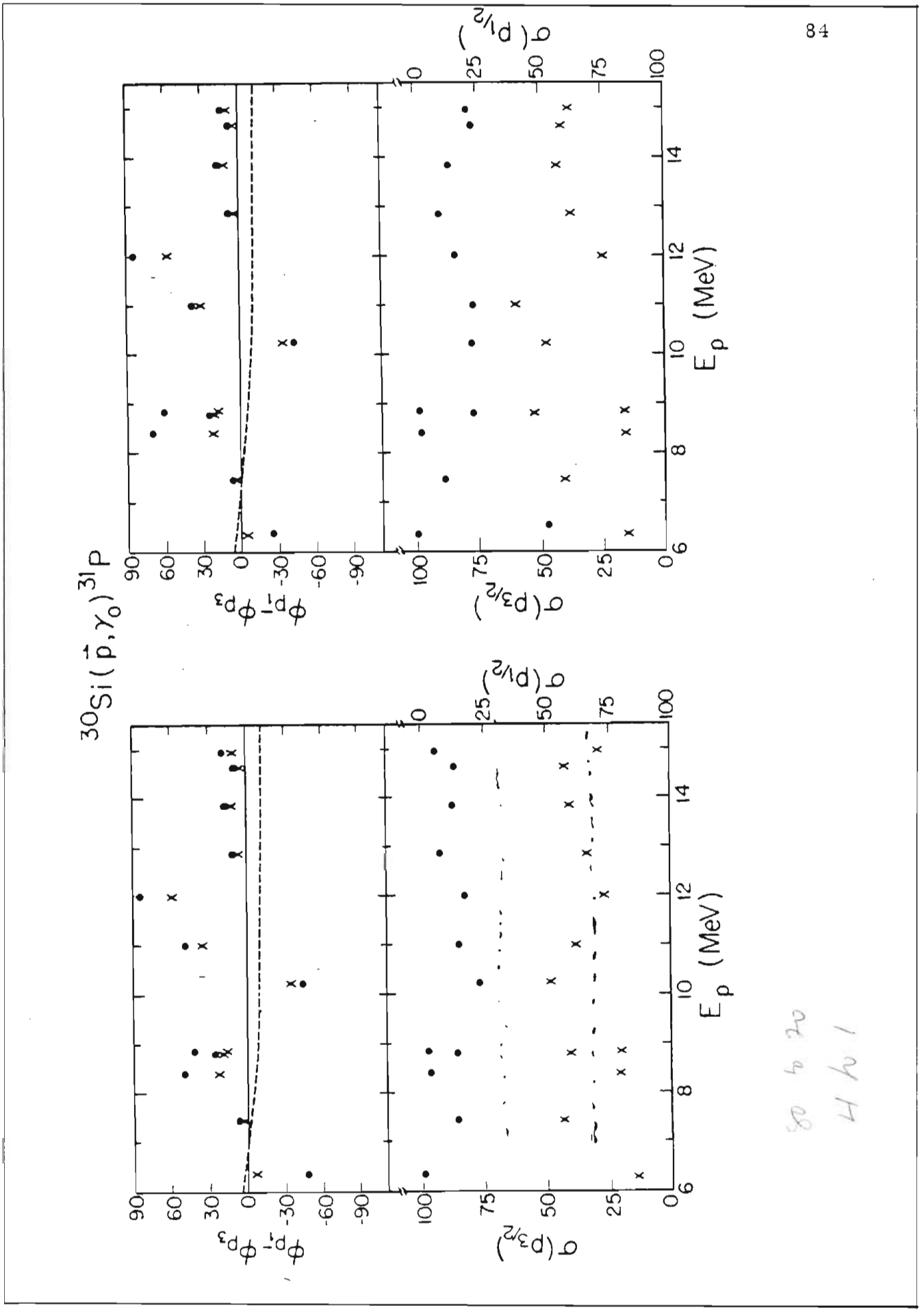
$^{30}Si(\vec{p},\gamma_0)^{31}P$
$\phi_{p_{\frac{1}{2}}} - \phi_{p_{\frac{3}{2}}}$
$\sigma(p_{3/2})$
$\sigma(p_{1/2})$
E_p (MeV)

Table VIII. The solutions obtained from an E1 analysis of the $^{30}Si(p,\gamma_0)^{31}P$ reaction. The two solutions obtained for each energy using the values of a and b from the fourth order fits are given in the top line, and the two solutions obtained from the third order fits are given in the lower line.

E_p (MeV)	$\sigma(p_{3/2})$ (%)	$\sigma(p_{1/2})$ (%)	$\phi_{p_1} - \phi_{p_3}$ (deg)	$\sigma(p_{3/2})$ (%)	$\sigma(p_{1/2})$ (%)	$\phi_{p_1} - \phi_{p_3}$ (deg)
6.36	16	84	-5	99	1	-27
	14	86	-8	99	1	-48
7.46	41	59	3	88	12	4
	43	57	3	86	14	5
8.4	16	84	22	98	2	70
	21	79	20	97	3	51
8.81	53	47	20	77	23	24
	42	58	18	86	14	26
8.85	16	84	17	98	02	61
	20	80	15	98	02	43
10.225	47	53	-35	78	22	-44
	48	52	-36	77	23	-45
11.01	50	50	31	77	23	38
	38	62	34	85	15	49
12.0	25	75	58	84	16	86
	27	73	58	83	17	85
12.85	38	62	5	90	10	8
	34	66	6	92	8	10
13.775	43	57	12	86	14	17
	41	59	11	88	12	17
14.625	41	59	5	88	12	7
	42	58	5	87	13	8
14.95	39	61	9	89	11	14
	29	71	9	95	05	18

shown in terms of the percentage of the cross section due to each amplitude. Two sets of solutions are shown, corresponding to the values of a_2 and b_2 obtained from the fits through $P_3(\cos\theta)$ and $P_{\frac{1}{3}}(\cos\theta)$ on the left, and from the fits through order 4 on the right. In each case the equations allow two solutions - one in which the $p_{1/2}$ amplitude dominates and one in which the $p_{3/2}$ amplitude dominates. The phase for the dominant $p_{1/2}$ solution is observed to be consistently larger in magnitude. At 10.2 MeV, the phase is opposite in sign, corresponding to the large positive assymetry observed for forward angles at this energy. The dashed line shows the optical model phase difference obtained from the global parameters of Becchetti and Greenlees (1969); this relative phase difference compares favorably with the phase difference calculated from specific parameters for this mass and energy region (Perey and Perey, 1974). The calculated phase difference, which is due only to spin-orbit splitting, is quite small. The observed phase difference is always less than 90°, but is quite scattered in value. The phase difference for the two solutions are quite similar, and thus the ambiguity of two solutions is not resolved by a comparison with the optical model. These results are similar to the results of previous experiments (Hanna et al., 1972, and Appendix B) in that the amplitudes remain essentially constant over the region of the GDR. This lack of change in structure across the GDR is one of the surprising results of polarized proton capture experiments. One might

expect to see one of the E1 amplitudes increase and the other decrease across the GDR, but in these experiments, only the phase is observed to show any dramatic change.

A T-matrix analysis of the decay to the $3/2^+$ first excited state is significantly more complicated than for the ground state transition because there are three E1 amplitudes which may contribute to the cross section. The equations for a_0, a_2, and b_2 are

$$a_0 = p_{1/2}^2 + 2\,p_{3/2}^2 + 3\,f_{5/2}^2$$

$$a_2 = 0.633\,p_{1/2}\,p_{3/2}\cos(p_1 - p_3) + 2.324\,p_{1/2}\,f_{5/2}\cos(p_1 - f_5) + 0.8\,p_{3/2}^2 - 1.47\,p_{3/2}\,f_{5/2}\cos(p_3 - f_5) - 1.2\,f_{5/2}^2$$

$$b_2 = 0.316\,p_{1/2}\,p_{3/2}\sin(p_1 - p_3) - 0.775\,p_{1/2}\,f_{5/2}\sin(p_1 - f_5) + 1.23\,p_{3/2}\,f_{5/2}\sin(p_3 - f_5)$$

where p_1, p_3, and f_5, are the phases associated with the T-matrix amplitudes. In previous works (Ledford, 1976 and Appendix B) for which three E1 amplitudes are possible because $Y_2 > 1/2$, the analysis was simplified by assuming that the contribution of the amplitude which corresponded to a spin-flip transition, which in this case would be the $p_{3/2}$ amplitude, is negligible. In this experiment, however, the measured b_2 coefficient was in most cases too large to be due to the interference of only two E1 amplitudes. The maximum value of b_2, 0.224, occurs if the $p_{1/2}$ and $f_{5/2}$ amplitudes each account for

50% of the cross section and the relative phase between them is 90°. Thus, all three amplitudes must be included in the analysis and the solutions.

The solutions to these equations that are in agreement with the experimentally determined coefficients were found by a computer search over the amplitudes and phases. The computer program is essentially the same as the one described in Appendix B. The $p_{1/2}$ and $p_{3/2}$ amplitudes were stepped over the allowed range of 0 to 1, and the $f_{5/2}$ amplitude was determined by the requirement that $a_0 = 1$. The step size was chosen so that the amplitude raised to the power $\sqrt{2}$ was incremented over 25 equal steps from 0 to 1 ; this power allows the contribution of both interference and squared terms to change nearly equally over the allowed range. The relative phases $(\phi_{P_3} - \phi_{P_1})$ and $(\phi_{f_5} - \phi_{P_1})$ were stepped in 10° increments from 0° to 350°. For each set of parameters the value of χ^2 was calculated using the expression

$$\chi^2 = \left(\frac{a_2(exp) - a_2(calc)}{\delta a_2(exp)}\right)^2 + \left(\frac{b_2(exp) - b_2(calc)}{\delta b_2(exp)}\right)^2$$

A solution was accepted and plotted by the computer if $\chi^2 \leq 1$. The results are shown in fig. 21. A wide range of possible solutions is observed, as may be expected since there are three equations and five unknowns. At 12.0, 14.625, and 14.95 MeV, both relative phases are undetermined, indicating an acceptable solution corresponding to $p_{1/2} = 0$, while at 14.625 MeV and 14.95

Figure 21. The solutions obtained from an E1 analysis of the $^{30}Si(p,\gamma_1)^{31}P$ reaction plotted as a function of the $p_{1/2}$ amplitude. Each solution, as represented by a solid dot, corresponds to a value of $\chi^2 \leq 1$. The amplitudes are expressed in terms of the percentage of the cross section due to each amplitude.

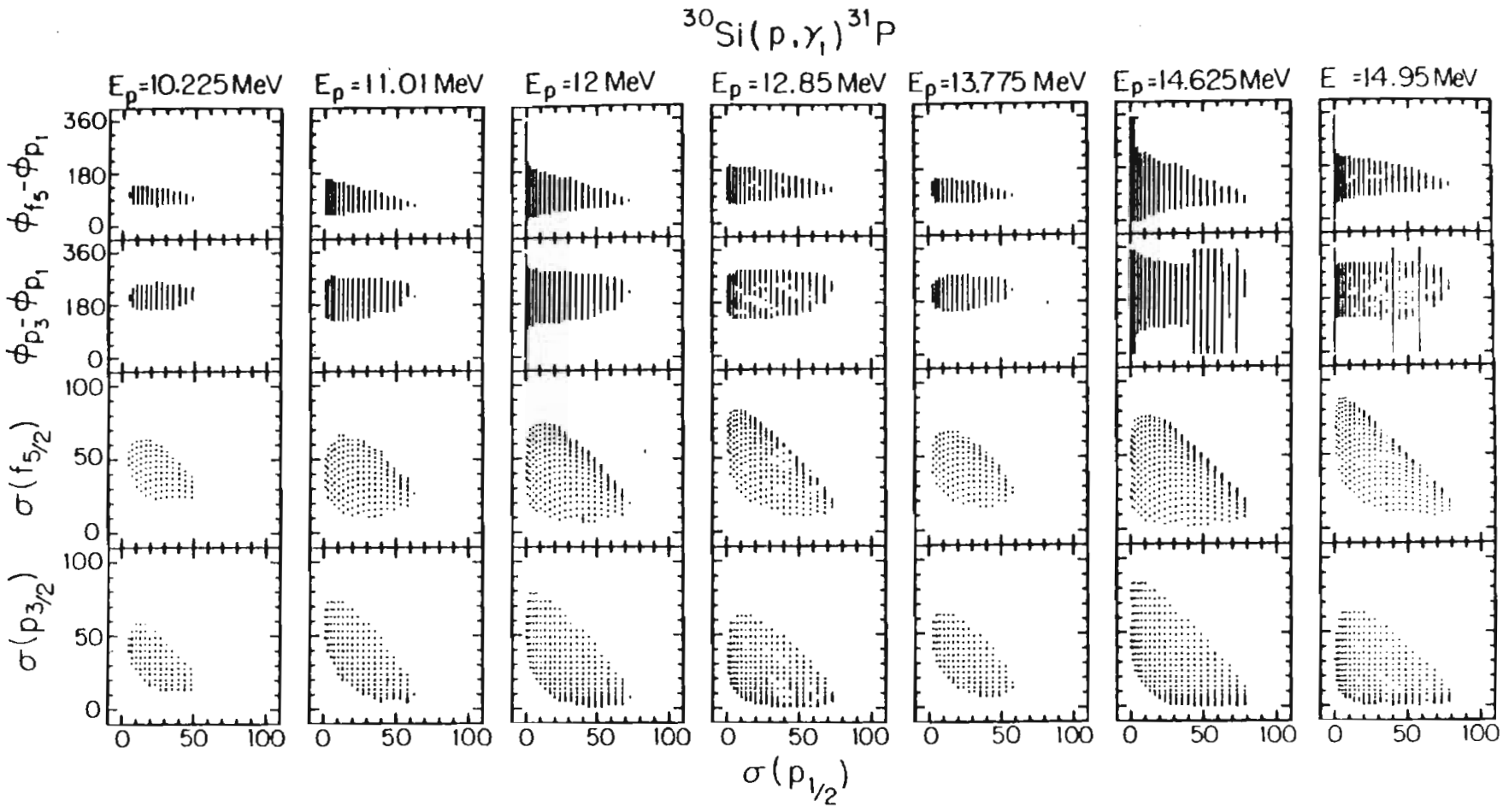
$^{30}Si(p,\gamma_1)^{31}P$
E_p=10.225 MeV
E_p=11.01 MeV
E_p=12 MeV
E_p=12.85 MeV
E_p=13.775 MeV
E_p=14.625 MeV
E =14.95 MeV
$\phi_{f_5}-\phi_{p_1}$
$\phi_{p_3}-\phi_{p_1}$
$\sigma(f_{5/2})$
$\sigma(p_{3/2})$
$\sigma(p_{1/2})$
360
180
0
100
50
0
0 50 100

MeV, the $(\phi_{P_3} - \phi_{P_1})$ phase is undetermined, corresponding to a solution for which $p_{3/2}=0$. For the remaining four energies, only solutions were found for which all three amplitudes were finite. Nevertheless upon examining these solutions, two important results may be noted. First, there are solutions at each energy for which the spin-flip amplitude can be relatively small, i. e. $\sigma(p_{3/2})<10\%$ of the cross section. In general, these solutions correspond to $\sigma(p_{1/2})\approx 50\%$ and $\sigma(f_{5/2})\approx 40\text{-}50\%$. As in the solutions for γ_0, these values show little change across the GDR. The second results is that the relative phase, is roughly 180° to 240°, quite different from the small phase predicted by the optical model as shown in fig. 20. There is an uncertainty of 180° in the phase obtained from the optical model, but the fact that the phase obtained for γ_0 is small and the fact that the phase difference, $(\phi_{P_3} - \phi_{P_1})$, is due to spin-orbit effects makes the large value observed surprising.

The T-matrix analysis may be extended to include E2 and M1 as well as E1 radiation. For γ_1, however, there are four E2 amplitudes and three M1 amplitudes that may contribute to the cross section, and thus there are too many unknowns. For γ_0, there are only two E2 and two M1 amplitudes possible, and it is reasonable to attempt to evaluate these parameters. Although E3 and M2 radiation is also possible, the contribution of these and higher multipoles is assumed to be negligible and is not considered in the present analysis. The a and b coefficients are then expressed in terms of the T-matrix amplitudes and

phases as follows:

$$a_0 = S^2_{1/2}(M1) + P^2_{1/2}(E1) + 2P^2_{3/2}(E1) + 2d^2_{3/2}(E2) + 2d^2_{3/2}(M1) + 3d^2_{5/2}(E2)$$

$$a_1 = -2S_{1/2}(M1)P_{1/2}(E1)\cos(s-p_1) + 2S_{1/2}(M1)P_{3/2}(E1)\cos(s-p_3)$$
$$+ 2P_{1/2}(E1)d_{3/2}(M1)\cos(p_1-d_{3M}) - 2P_{3/2}(E1)d_{3/2}(M1)\cos(p_3-d_{3M})$$
$$+ 3.464\,P_{1/2}(E1)d_{3/2}(E2)\cos(p_1-d_{3E}) + 0.693\,P_{3/2}(E1)d_{3/2}(E2)\cos(p_3-d_{3E})$$
$$+ 6.235\,P_{3/2}(E1)d_{5/2}(E2)\cos(p_3-d_5)$$

$$a_2 = -2S_{1/2}(M1)\,d_{3/2}(M1)\cos(s_1-d_{3M}) - P^2_{3/2}(E1) - d^2_{3/2}(M1)$$
$$- 2P_{1/2}(E1)P_{3/2}(E1)\cos(p_1-p_3) - 3.464\,S_{1/2}(M1)d_{3/2}(E2)\cos(s-d_{3E})$$
$$+ 3.464\,S_{1/2}(M1)d_{5/2}(E2)\cos(s-d_5) + 3.464\,d_{3/2}(M1)d_{3/2}(E2)\cos(d_{3M}-d_{3E})$$
$$- 3.464\,d_{3/2}(M1)d_{5/2}(E2)\cos(d_{3M}-d_5) + d^2_{3/2}(E2)$$
$$+ 0.857\,d_{3/2}(E2)d_{5/2}(E2)\cos(d_{3E}-d_5) + 1.714\,d^2_{5/2}(E2)$$

$$a_3 = -3.464\,P_{1/2}(E1)d_{5/2}(E2)\cos(p_1-d_5) - 4.157\,P_{3/2}(E1)d_{3/2}(E2)\cos(p_3-d_{3E})$$
$$- 2.771\,P_{3/2}(E1)d_{5/2}(E2)\cos(p_3-d_5)$$

$$a_4 = -6.857\,d_{3/2}(E2)d_{5/2}(E2)\cos(d_{3E}-d_5) - 1.714\,d^2_{5/2}(E2)$$

$$b_1 = 2S_{1/2}(M1)P_{1/2}(E1)\sin(s-p_1) + S_{1/2}(M1)P_{3/2}(E1)\sin(s,p_3)$$
$$- P_{1/2}(E1)d_{3/2}(M1)\sin(p_1-d_{3M}) + 4P_{3/2}(E1)d_{3/2}(M1)\sin(p_3-d_{3M})$$
$$- 1.732\,P_{1/2}(E1)d_{3/2}(E2)\sin(p_1-d_{3E}) - 1.386\,P_{3/2}(E1)d_{3/2}(E2)\sin(p_3-d_{3E})$$
$$+ 3.118\,P_{3/2}(E1)d_{5/2}(E2)\sin(p_3-d_5)$$

$$b_2 = S_{1/2}(M1)d_{3/2}(M1)\sin(s-d_{3M}) - P_{1/2}(E1)P_{3/2}(E1)\sin(p_1-p_3)$$
$$+ 1.732\,S_{1/2}(M1)d_{3/2}(E2)\sin(s-d_{3E}) + 1.155\,S_{1/2}(M1)d_{5/2}(E2)\sin(s-d_5)$$
$$- 2.887\,d_{3/2}(M1)d_{5/2}(E2)\sin(d_{3M}-d_5) + 0.714\,d_{3/2}(E2)d_{5/2}(E2)\sin(d_{3E}-d_5)$$

$$b_3 = -1.155\,P_{1/2}(E1)d_{5/2}(E2)\sin(p_1-d_5) + 1.386\,P_{3/2}(E1)d_{3/2}(E2)\sin(p_3-d_{3E})$$
$$- 0.231\,P_{3/2}(E1)d_{5/2}(E2)\sin(p_3-d_5)$$

$$b_4 = -1.714\,d_{3/2}(E2)\,d_{5/2}(E2)\sin(d_{3E}-d_5)$$

where d_{3M} and d_{3E} are the phases associated with the $d_{3/2}$(M1) and $d_{3/2}$(E2) amplitudes. As may be readily seen from these equations, the finite values of a_3 and b_3 observed experimentally imply the presence of one or both E2 amplitudes. Furthermore, finite a_4 coefficients would indicate the presence of the $d_{5/2}$(E2) amplitude, while finite b_4 coefficients would indicate the presence of both E2 amplitudes. Both E2 amplitudes have been included in the analysis presented here. In the initial analysis, the possibility of M1 radiation was ignored.

A grid search, similar to that used in the E1 analysis of the γ_1 data, was used to obtain solutions to the equations. A set of parameters was accepted if the values of a_k and b_k calculated from the above equations all fell within the experimental error. The results of the grid search were then used as initial values for a chi-square minimization procedure, following the method of Rosenbrock (1960), where

$$\chi^2 = \sum_{K=1}^{4} \left[\left(\frac{a_k(exp) - a_k(calc)}{\delta a_k(exp)} \right)^2 + \left(\frac{b_k(exp) - b_k(calc)}{\delta b_k(exp)} \right)^2 \right]$$

The curvature matrix of the chi-square space was evaluated analytically at the minimum obtained from the minimization procedure and was inverted to obtain the errors in the amplitudes and phases (Bevington, 1969). The results determined from the set of a and b coefficients obtained from the fits through P_3

and $P_{\frac{1}{3}}$ are given in fig. 22 and Table IX. a_4 and b_4 were taken to be zero within the errors obtained from the fits through P_4 and $P_{\frac{1}{4}}$. The E1 amplitudes and relative phases are not significantly different from those obtained from the simple E1 analysis, and, as before, two solutions are found. A crossing of the E1 amplitudes obtained from the two solutions near 10 MeV cannot be ruled out. This is in the area of the transition from the strength observed below 16 MeV excitation to the region of the giant dipole resonance. Two solutions are also obtained for the E2 amplitudes, and, at each energy, the dominant E2 amplitude corresponding to the dominant $p_{1/2}(E1)$ solution exchanges its strength with the other E2 amplitude for the dominant $p_{3/2}(E1)$ solution. However, the correspondence between dominant E1 and dominant E2 amplitudes changes with energy.

The analysis just described was repeated for the a and b coefficients obtained from the fits through P_4 and $P_{\frac{1}{4}}$. The results are given in Table X and fig. 23. The E2 strength obtained is considerably larger (there is a factor of four difference in the scale from the previous figure), and the E1 solutions have changed somewhat from the earlier E1 analysis. In addition, there are as many as four solutions at each energy. The ones corresponding to the most and least $\sigma(p_{3/2})$ are indicated by lines as before. Again, no particular correspondence between dominant E1 and dominant E2 amplitudes is observed.

Figure 22. The solutions obtained from an E1-E2 analysis of the $^{30}Si(p,\gamma_0)^{31}P$ reaction. The a_k and b_k coefficients from the third order fits are fit with two E1 and two E2 amplitudes. a_4 and b_4 are taken to be zero within the error determined from the fourth order fits. The T-matrix elements are expressed in terms of the percentage of the cross section due to each amplitude and the relative phase. The solid lines connect the solutions found at each energy for which the $p_{1/2}$ (E1) amplitude had its largest value, and the dashed lines indicate the solutions for which the $p_{3/2}$(E1) amplitude had its largest value. The error bars are discussed in the text. The results are tabulated in Table IX.

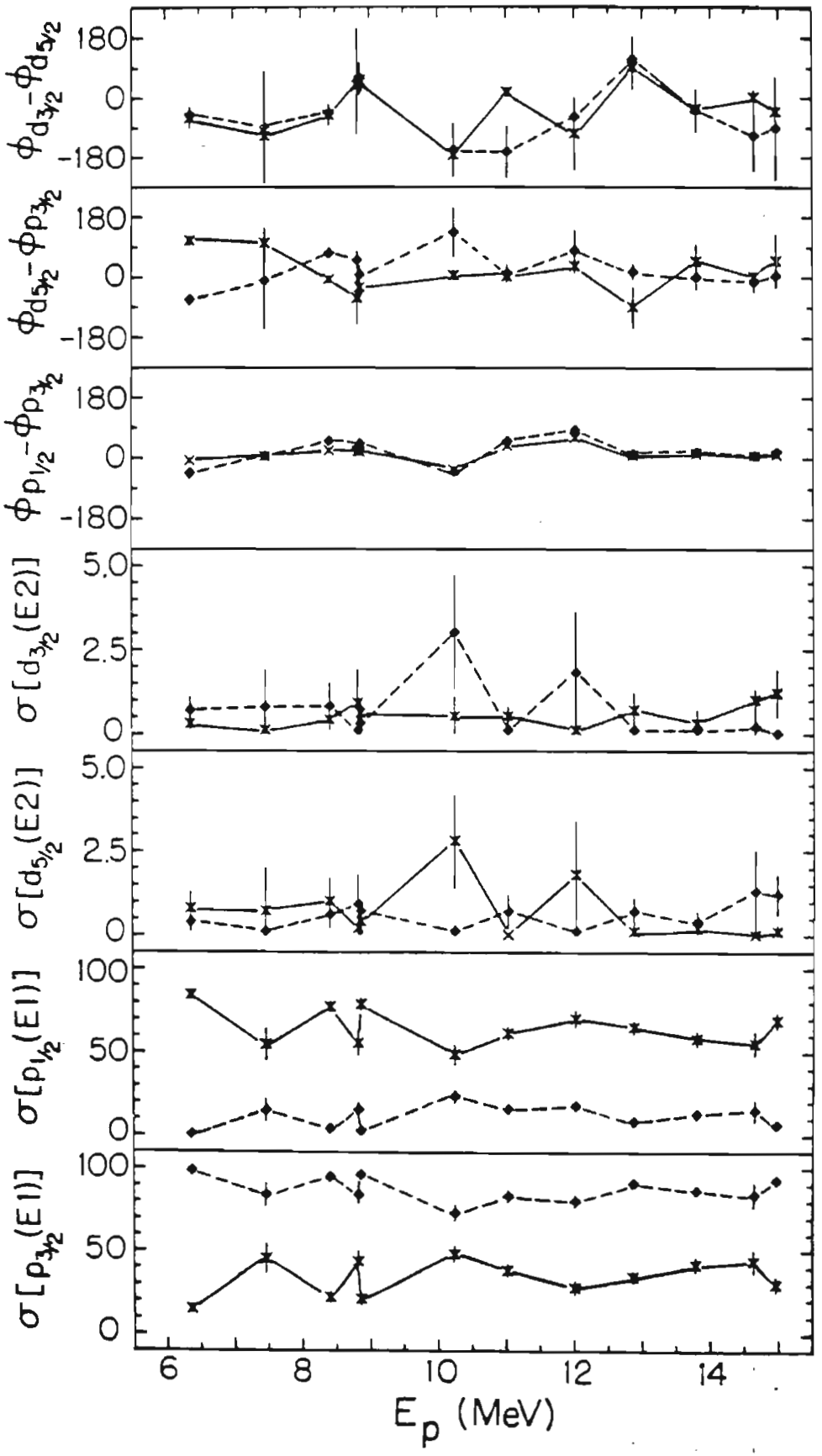
$\phi_{d_{3/2}}-\phi_{d_{5/2}}$
180
0
-180
$\phi_{d_{5/2}}-\phi_{p_{3/2}}$
180
0
-180
$\phi_{p_{1/2}}-\phi_{p_{3/2}}$
180
0
-180
$\sigma[d_{3/2}(E2)]$
5.0
2.5
0
$\sigma[d_{5/2}(E2)]$
5.0
2.5
0
$\sigma[p_{1/2}(E1)]$
100
50
0
$\sigma[p_{3/2}(E1)]$
100
50
0
6
8
10
12
14
E_p (MeV)

Table IX. The solutions obtained from an E1-E2 analysis of the third order fits to the angular distributions of the $^{30}Si(p,\gamma_0)^{31}P$ reaction.

E_p (MeV)	$\sigma[p_{3/2}(E1)]$ (%)	$\sigma[p_{1/2}(E1)]$ (%)	$\sigma[d_{5/2}(E2)]$ (%)	$\sigma[d_{3/2}(E2)]$ (%)	$\phi_{p_{1/2}} - \phi_{p_{3/2}}$ (deg)	$\phi_{d_{5/2}} - \phi_{p_{3/2}}$ (deg)	$\phi_{d_{3/2}} - \phi_{d_{5/2}}$ (deg)	χ^2
6.360	98.5± 0.8	0.5± 0.4	0.4± 0.3	0.7± 0.4	-45± 19	-68± 15	-52± 26	0.05
	14.7± 2.3	84.3± 2.5	0.8± 0.5	0.3± 0.2	-7± 3	109± 13	-60± 31	0.05
7.460	84.1± 7.2	15.0± 6.5	0.1± 0.3	0.8± 1.1	5± 3	-10±144	-88±168	0.02
	44.9± 8.9	54.3± 9.5	0.7± 1.3	0.1± 0.4	3± 2	99± 45	-118±107	0.02
8.400	94.9± 1.5	3.7± 1.2	0.6± 0.4	0.8± 0.7	48± 9	69± 16	-48± 21	0.11
	21.7± 3.1	77.0± 3.4	1.0± 0.7	0.4± 0.3	20± 3	-8± 8	-54± 32	0.11
8.810	43.5± 6.5	55.4± 7.3	0.2± 0.4	0.9± 1.0	18± 2	-65± 76	33± 89	0.03
	83.9± 5.0	15.1± 4.3	0.9± 0.9	0.1± 0.2	25± 3	48± 26	45±157	0.03
8.850	96.4± 0.1	2.7± 1.3	0.7± 0.3	0.3± 0.4	41± 12	5± 26	54± 46	0.03
	20.8± 3.7	78.3± 3.8	0.4± 0.5	0.6± 0.4	15± 4	-32± 38	48± 30	0.03
10.225	48.1± 4.9	48.6± 5.7	2.8± 1.4	0.5± 0.6	-36± 2	3± 16	-175± 46	3.74
	73.3± 5.0	23.5± 4.1	0.1± 0.2	3.0± 1.7	-43± 3	131± 73	-159± 80	3.75
11.010	83.3± 3.6	15.9± 3.1	0.7± 0.5	0.1± 0.3	48± 4	8± 26	-165± 77	0.01
	38.2± 4.0	61.3± 4.1	0.0± 0.0	0.5± 0.3	34± 2	0± 0	14± 13	0.26
12.000	28.0± 4.3	70.1± 5.1	1.8± 1.6	0.1± 0.2	58± 4	31± 21	-110±108	0.04
	80.3± 3.8	17.8± 2.9	0.1± 0.3	1.8± 1.8	82± 6	77± 60	-59± 51	0.04
12.850	91.0± 2.4	8.2± 2.1	0.7± 0.4	0.1± 0.2	10± 3	13± 22	114± 67	0.04
	34.3± 3.7	64.9± 3.9	0.1± 0.2	0.7± 0.5	6± 2	-92± 61	90± 66	0.04

Table IX. (continued)

E_p (MeV)	$\sigma[p_{3/2}(E1)]$ (%)	$\sigma[p_{1/2}(E1)]$ (%)	$\sigma[d_{5/2}(E2)]$ (%)	$\sigma[d_{3/2}(E2)]$ (%)	$\phi_{p_{1/2}} - \phi_{p_{3/2}}$ (deg)	$\phi_{d_{5/2}} - \phi_{p_{3/2}}$ (deg)	$\phi_{d_{3/2}} - \phi_{d_{5/2}}$ (deg)	χ^2
13.775	41.5± 4.4	58.1± 4.4	0.2± 0.3	0.3± 0.4	11± 1	44± 51	-36± 39	0.01
	86.5± 3.0	13.0± 2.9	0.4± 0.3	0.1± 0.3	17± 2	-2± 37	-41± 64	0.02
14.625	83.8± 7.5	14.8± 6.3	1.3± 1.2	0.2± 0.6	7± 3	-15± 30	-116±105	0.06
	43.6± 6.9	55.4± 7.0	0.0± 0.0	1.0± 0.3	5± 2	0± 0	0± 21	0.61
14.950	92.8± 2.4	6.0± 2.2	1.2± 0.6	0.0± 0.1	17± 5	2± 18	-93±154	0.01
	29.8± 4.3	69.0± 4.5	0.1± 0.2	1.2± 0.7	9± 3	47± 78	-42± 71	0.01

Figure 23. The solutions obtained from an E1-E2 analysis of the $^{30}Si(p,\gamma_0)^{31}P$ reaction. The a_k and b_k coefficients from the fourth order fits are fit with two E1 and two E2 amplitudes. The T-matrix elements are expressed in terms of the percentage of the cross section due to each amplitude and the relative phase. The solid lines connect the solutions found at each energy for which the $p_{1/2}$(E1) amplitude had its largest value, and the dashed lines indicate the solutions for which the $p_{3/2}$(E1) amplitude had its largest value. The error bars are discussed in the text. The results are tabulated in Table X.

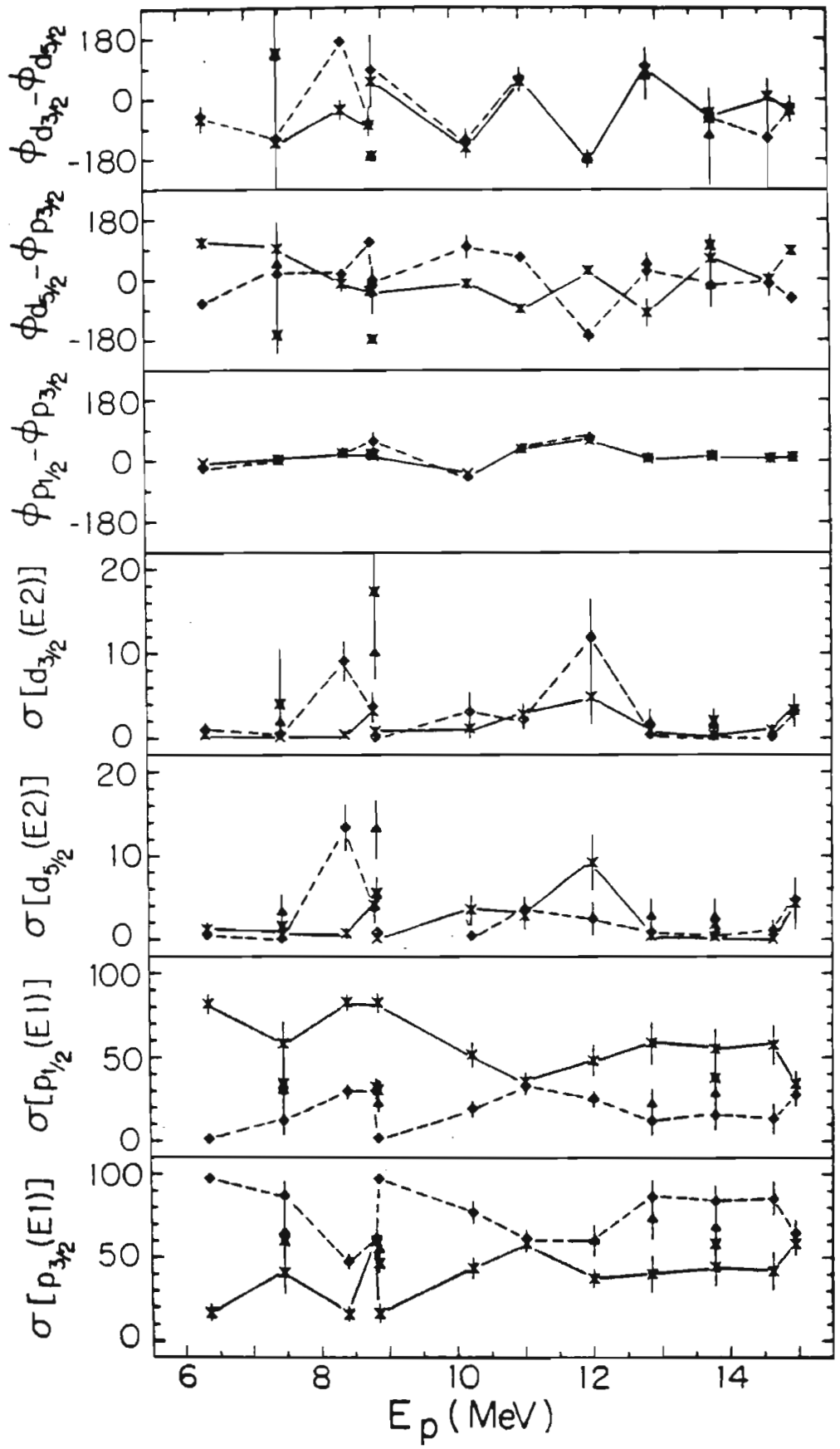
$\phi_{d_{3/2}} - \phi_{d_{5/2}}$
$\phi_{d_{5/2}} - \phi_{p_{3/2}}$
$\phi_{p_{1/2}} - \phi_{p_{3/2}}$
180
0
-180
$\sigma[d_{3/2}(E2)]$
$\sigma[d_{5/2}(E2)]$
20
10
0
$\sigma[p_{1/2}(E1)]$
$\sigma[p_{3/2}(E1)]$
100
50
0
6
8
10
12
14
E_p (MeV)

Table X. The solutions obtained from an E1-E2 analysis of the fourth order fits to the angular distributions of the $^{30}Si(p,\gamma_0)^{31}P$ reaction.

E_p (MeV)	$\sigma[p_{3/2}(E1)]$ (%)	$\sigma[p_{1/2}(E1)]$ (%)	$\sigma[d_{5/2}(E2)]$ (%)	$\sigma[d_{3/2}(E2)]$ (%)	$\phi_{p_{1/2}} - \phi_{p_{3/2}}$ (deg)	$\phi_{d_{5/2}} - \phi_{p_{3/2}}$ (deg)	$\phi_{d_{3/2}} - \phi_{d_{5/2}}$ (deg)	χ^2
6.360	16.9± 4.8	81.6± 5.4	1.2± 0.8	0.4± 0.4	-4± 3	112± 18	-62± 36	2.55
	97.5± 2.1	1.0± 1.2	0.5± 0.5	1.0± 0.7	-20± 17	-69± 14	-50± 31	2.54
7.460	65.2±14.2	29.8±20.5	3.2± 2.1	1.8± 8.7	4± 3	46±127	124±258	0.61
	60.3±10.4	34.1± 9.7	1.6± 2.2	4.0± 3.3	4± 3	-163± 55	134± 88	0.50
	41.3±12.7	58.1±12.9	0.5± 0.9	0.1± 0.4	3± 2	94± 54	-130± 86	0.85
	87.2± 8.3	12.2± 8.1	0.1± 0.3	0.5± 0.7	4± 3	18±126	-119±161	0.83
8.400	16.3± 4.4	82.6± 4.5	0.7± 0.6	0.4± 0.3	22± 4	-10± 23	-32± 29	3.20
	47.8± 4.9	29.6± 4.2	13.4± 2.7	9.1± 2.3	24± 4	18± 7	167± 12	8.08
8.810	61.6± 5.2	30.1± 4.9	3.7± 1.7	3.7± 1.7	21± 2	113± 15	-74± 29	2.17
	60.3± 5.2	32.3± 5.0	4.1± 1.6	3.2± 1.3	20± 2	-32± 16	-79± 33	2.18
8.850	54.9± 6.6	21.9± 4.1	13.2± 3.4	10.0± 3.0	17± 5	-1± 8	-170± 13	2.23
	46.7± 5.2	30.4± 5.5	5.5± 1.9	17.3± 4.5	16± 4	-176± 12	-170± 16	2.25
	16.7± 5.5	82.4± 5.5	0.1± 0.3	0.8± 0.5	17± 4	-29± 72	49± 61	1.53
	97.3± 1.2	1.7± 1.2	0.9± 0.4	0.1± 0.2	58± 27	0± 22	83±105	1.53
10.225	43.8± 6.2	51.6± 7.3	3.5± 1.7	1.1± 1.0	-36± 3	-10± 14	-144± 31	3.33
	77.2± 6.6	19.3± 5.0	0.4± 0.6	3.1± 2.2	-47± 6	99± 34	-122± 33	3.59
11.010	58.8± 5.2	35.6± 5.3	2.8± 1.5	2.8± 1.2	35± 3	-86± 14	50± 29	2.26
	61.5± 5.4	32.8± 4.9	3.6± 1.4	2.1± 1.0	36± 3	67± 14	57± 34	2.25

Table X. (continued)

E_p (MeV)	$\sigma[p_{3/2}(E1)]$ (%)	$\sigma[p_{1/2}(E1)]$ (%)	$\sigma[d_{5/2}(E2)]$ (%)	$\sigma[d_{3/2}(E2)]$ (%)	$\phi_{p_{1/2}} - \phi_{p_{3/2}}$ (deg)	$\phi_{d_{5/2}} - \phi_{p_{3/2}}$ (deg)	$\phi_{d_{3/2}} - \phi_{d_{5/2}}$ (deg)	χ^2
12.000	38.0± 5.4	48.0± 9.0	9.2± 3.3	4.8± 3.1	58± 6	28± 12	-176± 20	0.23
	60.2± 8.8	25.2± 4.6	2.6± 1.8	12.1± 4.3	68± 7	-166± 18	-175± 24	0.22
	60.7± 9.2	25.2± 4.8	2.4± 1.9	11.8± 4.4	69± 7	-165± 19	-178± 26	0.22
12.850	40.3±11.1	58.5±12.3	0.4± 0.7	0.9± 1.0	5± 2	-98± 42	86± 49	0.98
	73.4±11.8	22.1± 8.8	2.7± 2.1	1.8± 1.6	7± 2	50± 30	66± 67	0.66
	86.6± 9.8	12.1± 8.3	0.9± 1.0	0.4± 0.8	8± 3	25± 30	96± 55	0.97
13.775	58.5± 6.8	37.8± 7.8	1.8± 2.0	2.0± 1.4	12± 2	101± 32	-58± 67	0.18
	68.0± 9.5	28.1± 7.3	2.6± 2.2	1.4± 1.4	13± 2	-21± 59	-110±143	0.43
	44.4±11.1	55.0±11.6	0.3± 0.5	0.3± 0.6	12± 2	62± 58	-41± 49	0.92
	84.0± 9.1	15.3± 8.5	0.5± 0.7	0.2± 0.4	16± 4	-15± 40	-57± 80	0.90
14.625	41.9±11.2	57.3±11.4	0.0± 0.0	0.9± 0.6	5± 2	0± 0	6± 10	0.38
	85.5±10.0	13.4± 9.0	1.1± 1.2	0.1± 0.4	7± 4	-13± 35	-116±176	0.27
14.950	64.6± 7.7	27.6± 6.5	4.7± 2.4	3.2± 1.9	9± 3	-56± 15	-25± 34	0.05
	58.3± 7.2	34.1± 7.6	4.3± 3.0	3.3± 1.8	9± 3	86± 15	-31± 35	0.08

A comparison of Tables IX and X shows that the χ^2 values in Table X are often much larger. The finite a_4 and b_4 coefficients require a larger total E2 strength and the E2 amplitudes therefore contribute more to the interference terms in a_1, a_3, b_1, and b_3. M1 radiation also may contribute to a_1 and b_1 via E1-M1 interference; therefore, the analysis may be affected by the exclusion of M1 radiation. By ignoring a_1 and b_1, as Glavish et al. (1974) did in their analysis of the $^{31}P(\vec{p},\gamma_0)^{32}S$ reaction, the effect of excluding M1 radiation may be lessened, albeit at the expense of two degrees of freedom. The analysis of the a and b coefficients from the fourth order fits was repeated, but a_1 and b_1 were excluded from the calculation of chi-square. As before, the results of the grid searches and the minima from the previous analyses were used as starting points for the least squares minimization program. The results are given in Table XI and fig. 24. The χ^2 values obtained are considerably better than those given in Table X and fewer multiple solutions are obtained.

In an effort to determine how much M1 strength would be needed to account for the observed a_1 and b_1 coefficients, one of the possible M1 amplitudes may be introduced. There are two possibilities: $d_{3/2}(M1)$, which has the same phase as the $d_{3/2}(E2)$ amplitude (with the possible addition of 180°), and $s_{1/2}(M1)$. The latter seemed to fit the data better. As before, the results of the grid searches and the minima of the previous analyses were used as starting points. The results are given

Figure 24. The solutions obtained from an E1-E2 analysis of the $^{30}Si(p,\gamma_0)^{31}P$ reaction. The a_k and b_k coefficients from the fourth order fits are fit with two E1 and two E2 amplitudes. In order to make the analysis essentially independent of M1 strength, a_1 and b_1 were excluded from the chi-square minimization procedure. The T-matrix elements are expressed in terms of the percentage of the cross section due to each amplitude and the relative phase. The solid lines connect the solutions found at each energy for which the $p_{1/2}(E1)$ amplitude had its largest value, and the dashed lines indicate the solutions for which the $p_{3/2}(E1)$ amplitude had its largest value. The error bars are discussed in the text. The results are tabulated in Table XI.

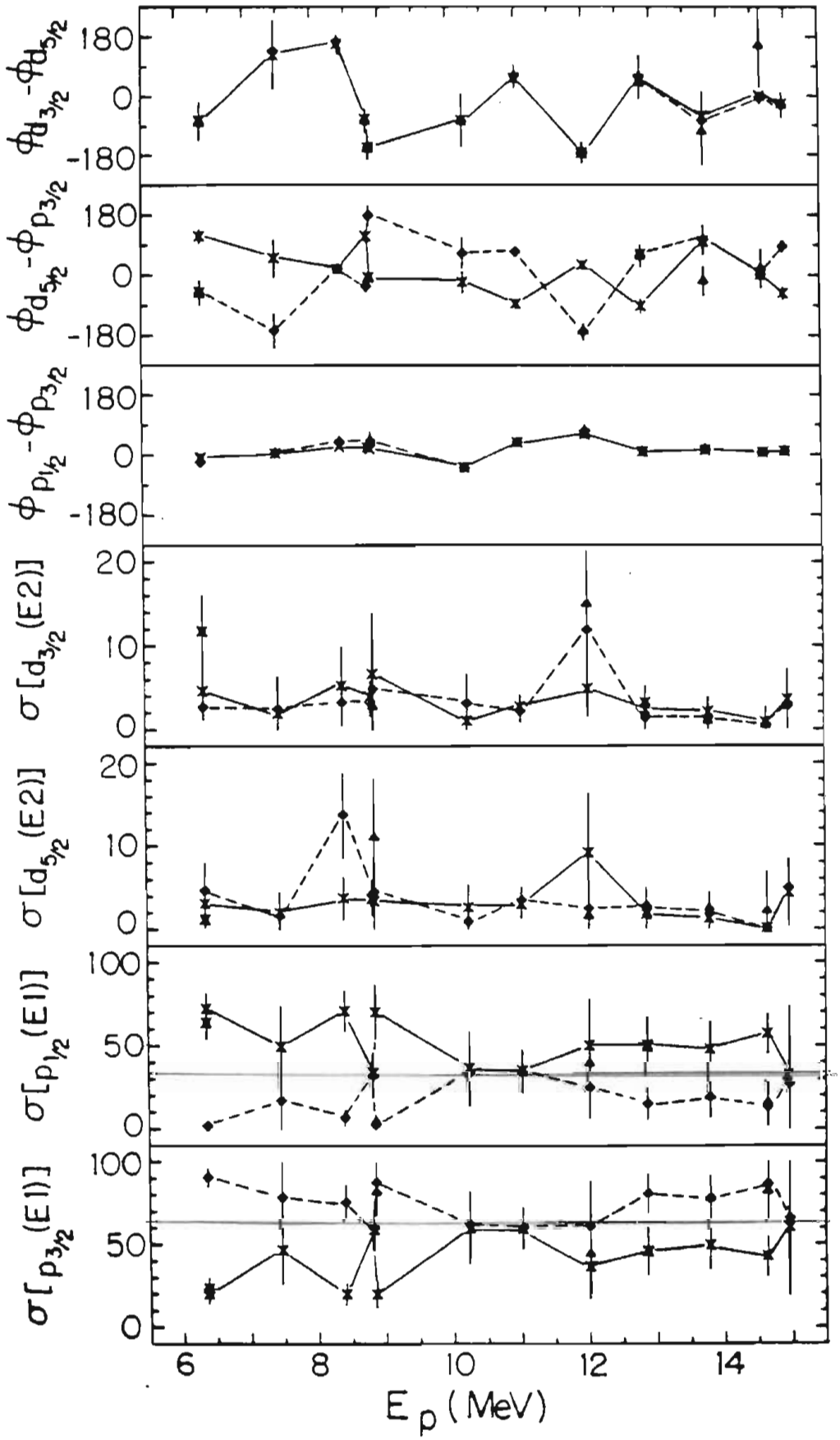
$\phi_{d_{3/2}} - \phi_{d_{5/2}}$
180
0
-180
$\phi_{d_{5/2}} - \phi_{p_{3/2}}$
180
0
-180
$\phi_{p_{1/2}} - \phi_{p_{3/2}}$
180
0
-180
$\sigma[d_{3/2}(E2)]$
20
10
0
$\sigma[d_{5/2}(E2)]$
20
10
0
$\sigma[p_{1/2}(E1)]$
100
50
0
$\sigma[p_{3/2}(E1)]$
100
50
0
6
8
10
12
14
E_p (MeV)

Table XI. The solutions obtained from an E1-E2 analysis of the fourth order fits, neglecting a_1 and b_1, to the angular distributions of the $^{30}Si(p,\gamma_0)^{31}P$ reaction.

E_p (MeV)	$\sigma[p_{3/2}(E1)]$ (%)	$\sigma[p_{1/2}(E1)]$ (%)	$\sigma[d_{5/2}(E2)]$ (%)	$\sigma[d_{3/2}(E2)]$ (%)	$\phi_{p_{1/2}} - \phi_{p_{3/2}}$ (deg)	$\phi_{d_{5/2}} - \phi_{p_{3/2}}$ (deg)	$\phi_{d_{3/2}} - \phi_{d_{5/2}}$ (deg)	χ^2
6.360	23.3± 6.6	64.0± 9.7	1.2± 1.0	11.7± 4.3	-6± 3	-51± 36	-74± 55	0.02
	90.6± 5.7	2.0± 2.1	4.7± 3.3	2.7± 1.5	-20± 12	-54± 33	-80± 53	0.00
	20.0± 6.0	72.3± 8.8	3.1± 1.9	4.6± 2.9	-6± 3	115± 19	-73± 53	0.00
7.460	46.7±20.4	49.4±24.2	2.0± 2.3	1.9± 4.4	4± 2	49± 55	124±104	0.01
	78.8±21.9	17.2±17.4	1.6± 2.8	2.5± 3.7	5± 3	-167± 51	136± 84	0.01
8.400	20.2± 6.6	70.9±11.8	3.7± 2.5	5.2± 4.6	23± 4	17± 12	156± 28	0.01
	75.9±11.0	7.1± 4.8	13.7± 5.1	3.2± 2.7	39± 13	16± 11	163± 18	0.01
8.810	58.9±12.5	33.6±12.5	3.6± 1.9	3.9± 1.9	20± 3	114± 15	-72± 29	1.97
	60.3±13.0	32.0±13.1	4.1± 1.8	3.2± 1.6	20± 3	-34± 16	-78± 33	1.93
8.850	20.1± 8.2	70.0±16.1	3.3± 3.0	6.6± 7.2	16± 4	-8± 17	-158± 34	0.01
	82.0±13.7	4.4± 4.4	11.0± 7.1	2.7± 3.6	33± 18	-10± 19	-162± 27	0.04
	87.9±12.8	2.8± 3.2	4.5± 5.5	4.8± 5.1	41± 26	176± 28	-157± 36	0.01
10.225	60.0±21.6	36.4±21.9	2.6± 2.7	1.0± 1.5	-38± 6	-22± 32	-75± 80	0.22
	62.7±20.1	33.4±19.4	0.9± 1.6	3.1± 3.5	-39± 7	64± 45	-78± 54	0.23
11.010	59.5±12.2	34.9±12.2	2.9± 1.6	2.7± 1.4	36± 4	-87± 14	50± 29	2.16
	60.8±12.1	33.7±12.0	3.4± 1.6	2.1± 1.2	36± 4	68± 15	57± 34	2.14
12.000	36.5±19.3	49.6±27.5	9.1± 7.2	4.8± 3.3	58± 7	29± 12	-173± 22	0.06
	44.6±23.7	39.0±25.6	1.5± 2.4	14.9± 4.3	61± 10	-171± 24	-172± 30	0.09
	61.3±27.5	24.6±18.1	2.4± 1.9	11.8± 9.5	69± 21	-171± 23	-172± 27	0.05

Table XI. (continued)

E_p (MeV)	$\sigma[p_{3/2}(E1)]$ (%)	$\sigma[p_{1/2}(E1)]$ (%)	$\sigma[d_{5/2}(E2)]$ (%)	$\sigma[d_{3/2}(E2)]$ (%)	$\phi_{p_{1/2}} - \phi_{p_{3/2}}$ (deg)	$\phi_{d_{5/2}} - \phi_{p_{3/2}}$ (deg)	$\phi_{d_{3/2}} - \phi_{d_{5/2}}$ (deg)	χ^2
12.850	46.1±14.5	49.0±16.8	1.7± 1.8	3.1± 2.0	6± 2	61± 26	41± 47	0.01
	81.0±11.9	15.0± 9.5	2.7± 2.2	1.3± 1.4	8± 3	56± 33	56± 66	0.01
	45.4±14.2	50.3±16.5	2.0± 2.4	2.3± 1.6	6± 2	-93± 20	47± 52	0.00
13.775	49.2±14.8	47.7±16.2	1.2± 1.9	2.0± 1.8	12± 2	99± 33	-60± 72	0.02
	78.3±13.5	18.8±11.9	1.7± 2.4	1.3± 1.6	15± 4	104± 43	-75± 85	0.00
	77.7±12.8	19.1±11.3	2.4± 2.0	0.9± 1.1	15± 4	-18± 43	-109± 98	0.08
14.625	42.4±11.9	56.8±11.6	0.0± 0.2	0.8± 1.3	5± 2	0± 0	0± 0	0.11
	82.0±18.8	15.5±13.7	2.1± 4.7	0.4± 2.2	7± 4	19± 57	152±126	0.02
	86.7± 8.2	12.8± 8.1	0.0± 0.0	0.5± 0.5	7± 4	0± 0	-6± 17	0.13
14.950	60.2±41.3	32.1±41.5	4.3± 4.0	3.5± 3.6	9± 4	-55± 18	-25± 35	0.04
	65.7±35.3	26.6±33.5	4.9± 3.4	2.7± 3.4	9± 5	85± 15	-29± 37	0.06

in Table XII and fig. 25. As in the last case, there are no degrees of freedom, thus the errors obtained are large. At some energies, only one solution is observed, with the $p_{3/2}$ amplitude being somewhat dominant.

These results may be converted to cross section by using the values of total cross section given in Table IV. For each solution, the total E1 and E2 strengths were obtained from the sums of the contributions of the amplitudes. The errors obtained are generally smaller than those observed for the individual amplitudes because of the correlation term obtained from the off-diagonal elements of the error matrix. The cross sections obtained from each solution are given in Table XIII. At each energy, the strengths and errors obtained were averaged and the results are shown in terms of the (γ,p_0) cross section in fig. 26.

The E2 cross section obtained from the third order fits is much smaller than that obtained from the fourth order fits; however, the different methods of analyzing the fourth order fits produce roughly similar results. The E2 cross section is observed to be strongest in the 15-16 MeV excitation region. The normalized fore-aft assymetry, as seen in fig. 15, is also peaked in that region. Above that region, the fore-aft asymmetry shows a gradual rise, suggesting that the E2 strength is smoothly increasing as the E1 strength decreases. This is consistent with the assumption that the E2 strength in the higher energy region is mostly direct. The E2 cross section (fig. 26)

Figure 25. The solutions obtained from an E1-E2-M1 analysis of the $^{30}Si(p,\gamma_0)^{31}P$ reaction. The a_k and b_k coefficients from the fourth order fits are fit with two E1, two E2 amplitudes, and one of the M1 amplitudes. The T-matrix elements are expressed in terms of the percentage of the cross section due to each amplitude and the relative phase. The solid lines connect the solutions found at each energy for which the $p_{1/2}$(E1) amplitude had its largest value, and the dashed lines indicate the solutions for which the $p_{3/2}$(E1) amplitude had its largest value. The error bars are discussed in the text. The results are tabulated in Table XII.

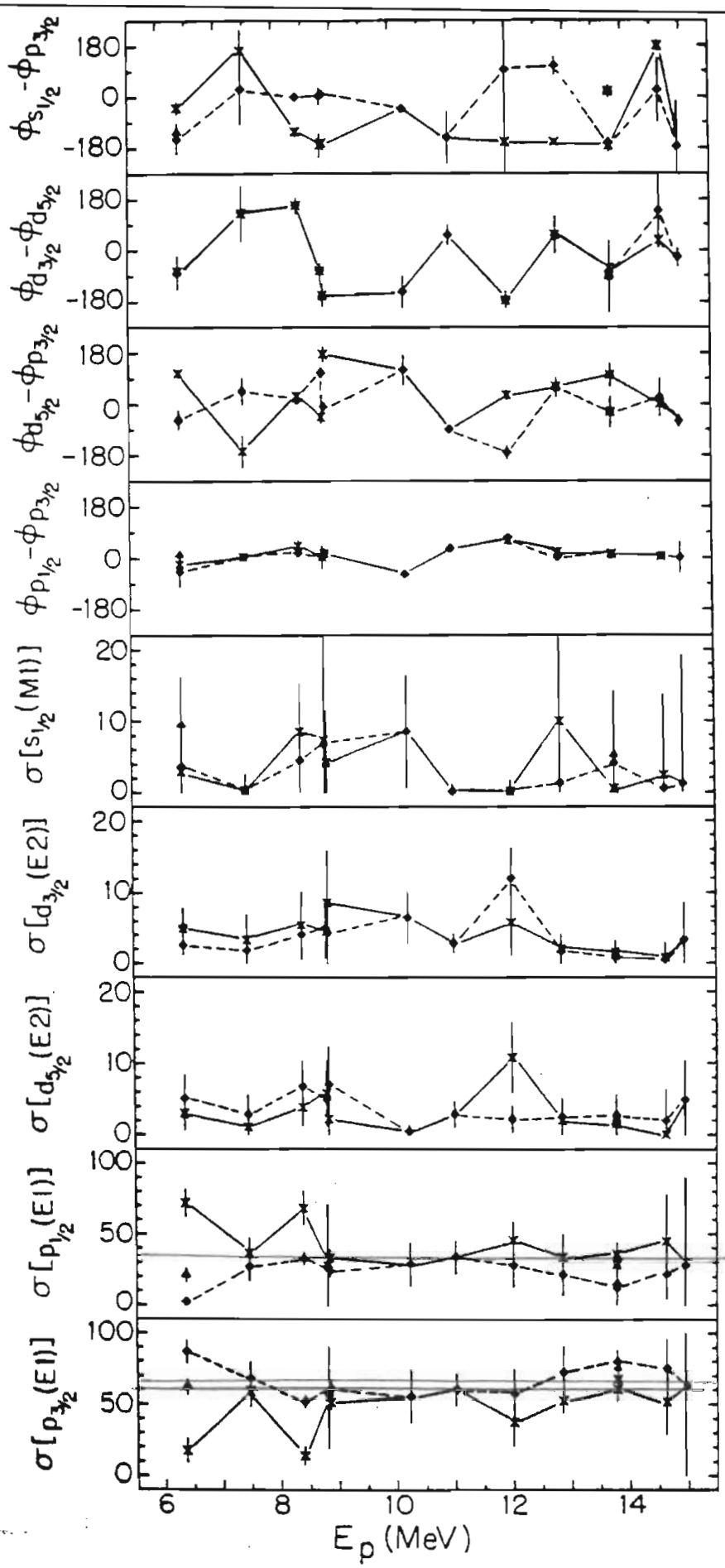

note diff with p. 84 — indicates danger in neglecting E2

Table XII. The solutions obtained from an E1-E2-M1 analysis of the fourth order fits to the angular distributions of the $^{30}Si(p,\gamma_0)^{31}P$ reaction.

E_p (MeV)	$\sigma[p_{3_2}(E1)]$ (%)	$\sigma[p_{1_2}(E1)]$ (%)	$\sigma[d_{5_2}(E2)]$ (%)	$\sigma[d_{3_2}(E2)]$ (%)	$\sigma[s_{1_2}(M1)]$ (%)	$\phi_{p_{1/2}} - \phi_{p_{3/2}}$ (deg)	$\phi_{d_{5/2}} - \phi_{p_{3/2}}$ (deg)	$\phi_{d_{3/2}} - \phi_{d_{5/2}}$ (deg)	$\phi_{s_{1/2}} - \phi_{p_{3/2}}$ (deg)	χ^2
6.360	61.7± 5.1	21.0± 4.8	2.7± 2.1	5.2± 2.2	9.5± 6.7	12± 13	-50± 30	-72± 53	-123± 25	0.00
	86.7± 8.2	2.0± 2.1	5.1± 3.3	2.6± 1.4	3.7± 4.9	-46± 54	-57± 30	-79± 56	-147± 54	0.00
	17.6± 8.3	71.8± 9.3	3.0± 2.1	4.8± 3.1	2.9± 5.4	-20± 16	107± 14	-72± 51	-38± 21	0.00
7.460	68.0±11.5	27.2±10.0	2.8± 2.8	1.8± 3.8	0.3± 2.0	3± 5	45± 47	134± 78	27±124	0.00
	59.0±10.4	36.3±11.1	1.1± 2.2	3.3± 3.7	0.3± 2.3	3± 7	-165± 55	129± 95	163± 71	0.00
8.400	14.2± 6.2	68.2±12.0	3.8± 2.4	5.4± 4.7	8.5± 6.8	43± 19	29± 12	156± 27	-123± 14	0.00
	51.9± 4.4	32.8± 4.4	6.7± 3.7	4.0± 3.4	4.5± 5.8	18± 5	13± 10	159± 24	-2± 10	0.00
8.810	56.4±26.1	26.9±43.4	4.9± 3.5	5.0± 3.7	6.8±28.6	5± 31	110± 18	-70± 24	0± 29	0.02
	55.2±35.7	27.5±43.3	5.8± 4.5	4.3± 3.5	7.3±32.4	3± 41	-45± 21	-71± 25	-172± 41	0.02
8.850	60.8± 6.1	24.1± 4.2	7.0± 5.3	4.2± 4.8	4.0± 7.0	18± 5	-9± 16	-160± 30	7± 12	0.00
	51.7± 5.0	33.3± 5.4	2.2± 2.8	8.6± 7.3	4.2± 7.2	16± 6	176± 25	-156± 38	-163± 10	0.00
10.225	55.7±18.1	28.9±15.2	0.4± 1.0	6.5± 3.7	8.5± 7.9	-56± 8	120± 52	-144± 54	-45± 8	1.80

Table XII. (continued)

E_p (MeV)	$\sigma[p_{3/2}(E1)]$ (%)	$\sigma[p_{1/2}(E1)]$ (%)	$\sigma[d_{5/2}(E2)]$ (%)	$\sigma[d_{3/2}(E2)]$ (%)	$\sigma[s_{1/2}(M1)]$ (%)	$\phi_{p_{1/2}} - \phi_{p_{3/2}}$ (deg)	$\phi_{d_{5/2}} - \phi_{p_{3/2}}$ (deg)	$\phi_{d_{3/2}} - \phi_{d_{5/2}}$ (deg)	$\phi_{s_{1/2}} - \phi_{p_{3/2}}$ (deg)	χ^2
11.010	60.2± 11.5	34.1±11.5	2.9± 1.8	2.8± 1.3	0.1± 1.0	34± 9	-88± 14	52± 34	-145± 89	2.12
12.000	37.5±16.3	45.8±13.1	10.8± 4.9	5.8± 4.7	0.1± 1.6	61± 17	31± 16	-175± 19	-160±221	0.00
	57.3±17.6	28.4±14.9	2.2± 1.9	12.0± 4.3	0.1± 1.2	69± 12	-170± 23	-172± 28	92±188	0.09
12.850	52.7± 8.4	33.5±16.8	2.0± 1.7	2.0± 2.1	9.9±18.9	21± 14	60± 32	54± 65	-160± 7	0.01
	72.9±18.1	21.7±14.4	2.5± 2.6	1.7± 1.2	1.3± 6.4	2± 14	57± 31	50± 58	107± 31	0.00
13.775	60.3± 8.1	36.0± 8.4	1.5± 2.1	1.6± 1.6	0.6± 2.6	14± 5	101± 33	-62± 74	-174± 19	0.01
	75.9±11.7	15.9±12.4	1.8± 2.4	1.3± 1.4	5.2± 8.4	10± 10	102± 41	-74± 86	18± 14	0.00
	67.4± 7.6	29.0± 7.1	2.0± 1.6	1.1± 1.1	0.5± 1.9	15± 5	-27± 53	-87±119	16± 21	0.01
	80.2± 8.0	12.2±11.6	2.8± 2.8	0.8± 0.8	4.1±10.1	10± 9	-27± 54	-94±122	-165± 19	0.01
14.625	51.8±22.5	45.1±32.8	0.0± 0.0	0.8± 0.6	2.4±11.3	5± 2	0± 0	-6± 20	178± 16	0.13
	75.2±20.9	21.7±17.0	2.0± 4.3	0.5± 2.4	0.6± 5.4	6± 6	24± 66	137±163	22±111	0.00
14.950	62.4±72.1	28.1±61.8	4.9± 5.5	3.3± 5.3	1.2±18.0	2± 55	-59± 19	-24± 32	-176±159	0.01

Figure 26. The E1-E2-M1 cross sections obtained from a T-matrix analysis of the $^{30}Si(p,\gamma_0)^{31}P$ reaction. The cross section has been converted to (γ,p_0) by detailed balancing. The points and the errors shown are the averages of the cross sections obtained from the multiple solutions at each energy. The methods of analysis used are:

A. Analysis of third order fits

B. Analysis of fourth order fits

C. Analysis of fourth order fits, a_1 and b_1 excluded

D. Analysis of fourth order fits with one M1 amplitude

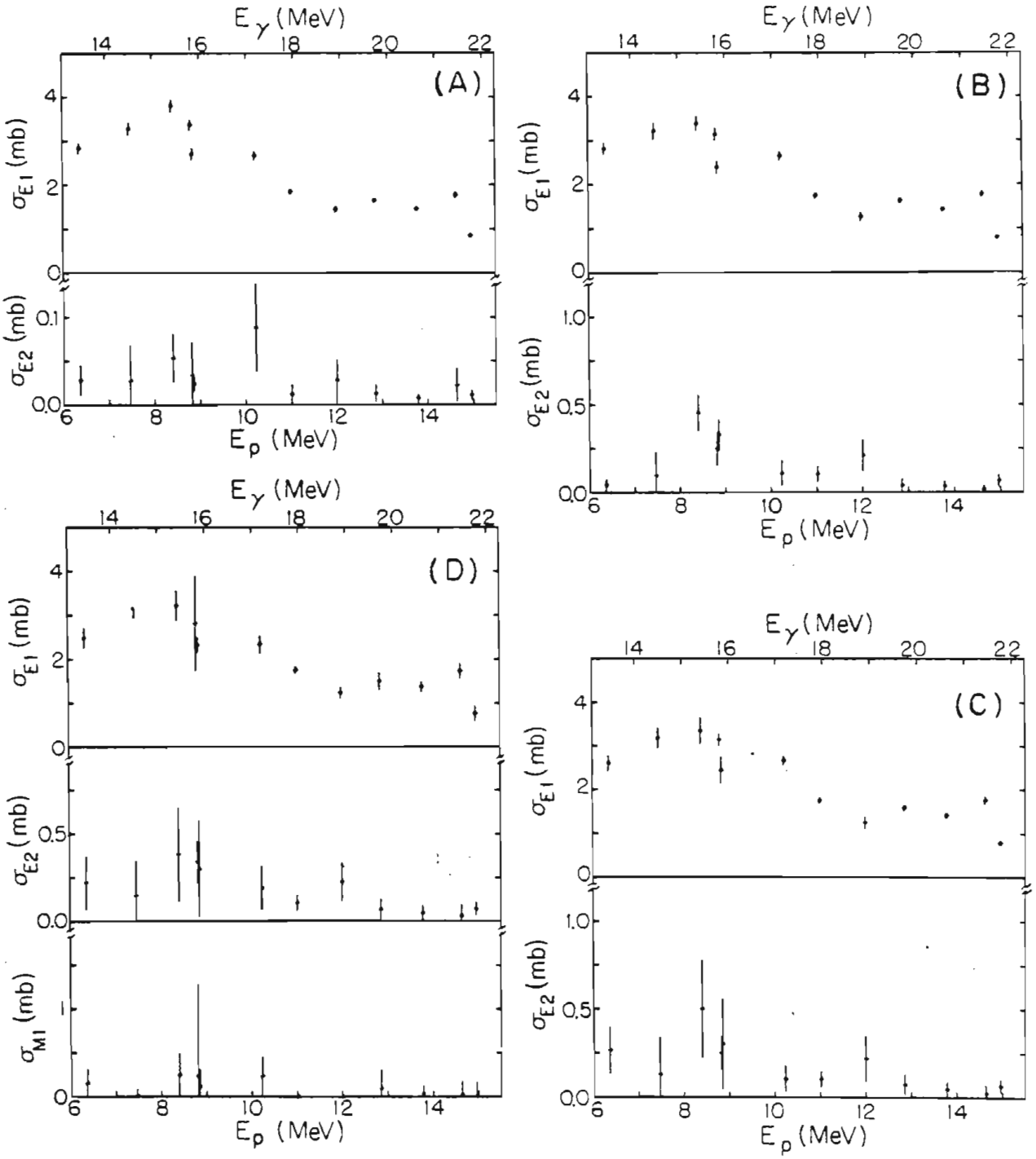
(A)
(B)
(C)
(D)
E_γ (MeV)
E_p (MeV)
σ_{E1} (mb)
σ_{E2} (mb)
σ_{M1} (mb)

Table XIII.
The E1 and E2 detailed balanced cross sections obtained from a T-matrix analysis of the third order fits to the angular distributions of the $^{30}Si(p,\gamma_0)^{31}P$ reaction.

E_p (MeV)	σ(E1) (mb)	σ(E2) (mb)
6.360	2.84±0.13	0.029±0.017
	2.84±0.13	0.029±0.017
7.460	3.29±0.14	0.030±0.040
	3.29±0.14	0.027±0.040
8.400	3.80±0.15	0.054±0.027
	3.80±0.15	0.054±0.027
8.810	3.37±0.11	0.037±0.041
	3.37±0.11	0.031±0.034
8.850	2.71±0.12	0.025±0.008
	2.71±0.12	0.025±0.008
10.225	2.67±0.10	0.091±0.050
	2.68±0.10	0.086±0.050
11.010	1.85±0.05	0.015±0.017
	1.86±0.05	0.009±0.006
12.000	1.45±0.06	0.028±0.024
	1.45±0.06	0.028±0.024
12.850	1.65±0.05	0.013±0.010
	1.65±0.05	0.013±0.010
13.775	1.46±0.04	0.007±0.004
	1.46±0.04	0.007±0.004
14.625	1.76±0.07	0.027±0.032
	1.77±0.06	0.018±0.005
14.950	0.85±0.03	0.011±0.005
	0.85±0.03	0.011±0.005

Table XIII. (continued)
The E1 and E2 detailed balanced cross section obtained from a T-matrix analysis of the fourth order fits to the angular distributions of the $^{30}Si(p,\gamma_0)^{31}P$ reaction.

E_p (MeV)	σ (E1) (mb)	σ (E2) (mb)
6.360	2.82±0.13	0.043±0.032
	2.82±0.13	0.046±0.034
7.460	3.15±0.33	0.166±0.302
	3.13±0.22	0.186±0.179
	3.30±0.14	0.020±0.023
	3.30±0.14	0.020±0.020
8.400	3.81±0.15	0.042±0.019
	2.99±0.21	0.867±0.184
8.810	3.15±0.14	0.252±0.096
	3.15±0.14	0.252±0.096
8.850	2.11±0.19	0.635±0.167
	2.11±0.19	0.627±0.169
	2.71±0.12	0.027±0.011
	2.71±0.12	0.027±0.011
10.225	2.64±0.11	0.127±0.072
	2.67±0.11	0.094±0.072
11.010	1.76±0.06	0.105±0.045
	1.76±0.06	0.106±0.045
12.000	1.27±0.10	0.206±0.090
	1.26±0.10	0.217±0.087
	1.26±0.10	0.209±0.090
12.850	1.64±0.05	0.022±0.027
	1.59±0.07	0.075±0.060
	1.64±0.05	0.022±0.030
13.775	1.41±0.05	0.056±0.037
	1.41±0.07	0.059±0.051
	1.45±0.04	0.010±0.012
	1.45±0.04	0.010±0.013
14.625	1.78±0.07	0.016±0.011
	1.77±0.07	0.022±0.029
14.950	0.79±0.05	0.068±0.035
	0.79±0.05	0.065±0.036

Table XIII. (continued)
The E1 and E2 detailed balanced cross sections obtained from a T-matrix analysis of the fourth order fits, neglecting a_1 and b_1, to the angular distributions of the $^{30}Si(p,\gamma_0)^{31}P$ reaction.

E_p (MeV)	σ (E1) (mb)	σ (E2) (mb)
6.360	2.50±0.18	0.367±0.147
	2.66±0.17	0.212±0.124
	2.65±0.17	0.221±0.124
7.460	3.19±0.24	0.129±0.199
	3.18±0.25	0.133±0.209
8.400	3.51±0.30	0.343±0.266
	3.20±0.31	0.655±0.286
8.810	3.15±0.14	0.252±0.096
	3.15±0.14	0.248±0.096
8.850	2.47±0.29	0.271±0.271
	2.36±0.30	0.375±0.244
	2.48±0.30	0.255±0.244
10.225	2.67±0.11	0.100±0.069
	2.66±0.11	0.108±0.077
11.010	1.76±0.06	0.105±0.045
	1.76±0.06	0.103±0.045
12.000	1.27±0.15	0.205±0.145
	1.23±0.10	0.242±0.082
	1.26±0.15	0.209±0.154
12.850	1.59±0.07	0.080±0.060
	1.60±0.07	0.067±0.057
	1.59±0.07	0.072±0.058
13.775	1.42±0.06	0.045±0.041
	1.42±0.06	0.042±0.041
	1.42±0.06	0.048±0.044
14.625	1.78±0.07	0.014±0.011
	1.75±0.14	0.045±0.122
	1.78±0.07	0.009±0.009
14.950	0.79±0.05	0.067±0.035
	0.79±0.05	0.066±0.038

Table XIII. (continued)
The E1, E2, and M1 detailed balanced cross sections obtained from a T-matrix analysis of the fourth order fits to the angular distributions of the $^{30}Si(p,\gamma_0)^{31}P$ reaction.

E_p (MeV)	σ(E1) (mb)	σ(E2) (mb)	σ(M1) (mb)
6.360	2.37±0.17	0.227±0.115	0.272±0.192
	2.54±0.24	0.218±0.127	0.106±0.141
	2.56±0.24	0.224±0.210	0.083±0.155
7.460	3.16±0.21	0.153±0.199	0.010±0.066
	3.16±0.20	0.146±0.189	0.010±0.076
8.400	3.17±0.51	0.355±0.266	0.328±0.262
	3.27±0.17	0.413±0.266	0.173±0.224
8.810	2.83±0.99	0.340±0.113	0.231±0.973
	2.81±1.14	0.340±0.116	0.248±1.103
8.850	2.32±0.16	0.304±0.274	0.110±0.192
	2.33±0.16	0.296±0.277	0.115±0.197
10.225	2.34±0.20	0.191±0.122	0.235±0.218
11.010	1.76±0.07	0.106±0.047	0.002±0.019
12.000	1.23±0.16	0.243±0.136	0.001±0.024
	1.26±0.10	0.209±0.083	0.001±0.018
12.850	1.43±0.29	0.067±0.058	0.165±0.315
	1.58±0.09	0.068±0.060	0.022±0.107
13.775	1.41±0.05	0.045±0.043	0.009±0.038
	1.35±0.14	0.044±0.041	0.076±0.123
	1.41±0.05	0.045±0.038	0.007±0.028
	1.35±0.19	0.051±0.048	0.060±0.148
14.625	1.74±0.21	0.014±0.011	0.043±0.202
	1.73±0.11	0.045±0.120	0.011±0.097
14.950	0.78±0.16	0.070±0.036	0.010±0.154

is smaller at the higher energies, and does not suggest any peaking, though it does fluctuate somewhat. The E2 cross section for the reaction $^{31}P(p,\gamma_0)^{32}S$ (Glavish et al., 1974) is observed to vary more smoothly, varying from 2.5 μb to 5 μb in strength [(p,γ_0) cross section]. If the E2 cross section in this mass region contains as much fine structure as the total (p,γ_0) cross section, then the variation in the observed E2 cross section for ^{31}P may be expected, while the thick target used in the $^{31}P(p,\gamma_0)^{32}S$ experiment would have washed out the fine structure.

C. Comparison to Sum Rules

The classical dipole sum rule is given by the equation (Hayward, 1970)

$$\int \sigma_{E1}(\gamma,x) = 60\,\frac{NZ}{A}$$

The total cross section in the $^{30}Si(p,\gamma_0)^{31}P$ reaction may be converted to (γ,p_0) cross section by detailed balancing. The results are given and compared to the sum rule in Table XIV. The total integrated cross section was obtained from the 90° excitation function for γ_0 by assuming an average value of 0.8 for a_2 and 0.0 for a_4. Above E =16.4 MeV, the values of A_0 given in Table IV were used. The E2 strength, which as seen in the last section is at most a few percent of the total cross

Table XIV. The energy integrated cross sections compared with the dipole sum rule.

	$\int \sigma_{E1}(\gamma,x)dE$ (mb-MeV)	% of Sum Rule	Energy Range (E_γ MeV)
$\frac{60NZ}{A}$	465		
$^{31}P(\gamma,n)^{30}P$[a]	120	25.8	13.6-23.0
$^{31}P(\gamma,n_o)^{30}P$[a]	25	5.4	13.6-23.0
$^{31}P(\gamma,p_o)^{30}Si$	16	3.4	12.0-35.0
$^{31}P^*(\gamma_1,p_o)^{30}Si$	35	7.5	10.8-33.8

[a] Gellie et al., 1973

section, was not subtracted. The 90° excitation function for γ_1 was converted to total cross section and integrated by assuming that both a_2 and a_4 have an average value of 0; above E =16.4 MeV, the values of A_0 given in Table VII were used. The integrated yields are also given for the $^{31}P(\gamma,n_0)^{30}P$ and $^{31}P(\gamma,n)^{30}P$ reaction (Gellie et al., 1973), where the angular distribution were assumed to behave as $\sin^2\theta$ for (γ,n_0) and the (γ,n) reaction was assumed to be isotropic. The results show that only a small fraction of the sum rule is seen in the ground state proton channel, and only slightly more strength is observed in the ground state neutron channel. The strength observed in the (p,γ_1) channel is for a separate resonance, the resonance built upon the first excited state of ^{31}P.

Separate E2 sum rules are given for $\Delta T=0$ and $\Delta T=1$ transitions. They are (Gell-Mann and Teleqdi, 1953):

$$\Delta T=0: \quad \int \frac{\sigma_{E2}(\gamma,x)}{E^2}\,dE = 2.2\times10^{-4}\,\frac{Z^2}{A^{1/3}}\,\frac{mb}{MeV}$$

$$\Delta T=1: \quad \int \frac{\sigma_{E2}(\gamma,x)}{E^2}\,dE = 2.2\times10^{-4}\,\frac{NZ}{A}\,\frac{mb}{MeV}$$

$$Total: \quad \int \frac{\sigma_{E2}(\gamma,x)}{E^2}\,dE = 2.2\times10^{-4}\,Z\,A^{2/3}\,\frac{mb}{MeV}\,.$$

The average E2 strength obtained from the T-matrix analysis of

the previous section and shown in fig. 26 is integrated and compared to the sum rules in Table XV. The fraction of the sum rule obtained from the minimum and from the maximum values of the E2 cross section obtained for each energy are also given. The analysis of the third order fits yields only 3% of the total sum rule, which is comparable to the observed dipole strength, while the fourth order fits yield roughly 18% of the total sum rule. While the latter number is comparable to the result (25%) obtained by Glavish et al. (1974) for ^{32}S, it is quite large in comparison to the amount of the dipole sum seen in the ground state channel.

Bohr and Mottelson (1975) have predicted the existence of an isoscalar giant quadrupole resonance (GQR) near $Ex=58A^{1/3}$ = 18.5 MeV for ^{31}P. In this mass region, the isoscalar GQR has been reported to have been observed near the predicted location by inelastic scattering. In an inelastic proton scattering experiment on ^{27}Al, Lewis and Bertrand (1972) reported the existence of a resonance at Ex=19.5±0.8 MeV, Γ=3-4 MeV. Youngblood et al. (1976) have studied ^{32}S via inelastic alpha scattering and they report a resonance at Ex=18.4±0.3 MeV, Γ=7.1±0.5 MeV. In a more recent alpha particle inelastic scattering experiment, Kiss et al. (1976) used higher bombarding energies to study $^{24,25,26}Mg$ and ^{27}Al. They obtain a centroid of 18.5 MeV, Γ=7.6 MeV, for the GQR of ^{27}Al. The resonance is observed to decrease slowly on the high energy side, and the peak of the resonance is actually somewhat below

Table XV. The E2 integrated cross section compared with the quadrupole sum rules. The maximum, average, and minimum results from the solutions for each method are given.

Method	(μb/MeV)	% of Sum Rules ΔT=0	ΔT=1	Total
A.	1.1±0.3	7± 2	7± 2	3± 1
	1.0±0.3	6± 2	6± 2	3± 1
	1.0±0.3	6± 2	6± 2	3± 1
B.	7.1±1.2	45± 8	42± 7	22± 4
	4.5±0.8	29± 5	28± 5	14± 2
	2.0±0.4	13± 3	12± 2	6± 1
C.	7.5±1.7	47±11	45±10	23± 5
	6.1±1.7	39±11	36±10	19± 5
	5.1±1.6	32±10	30±10	16± 5
D.	6.3±1.7	40±11	38±10	19± 5
	6.0±1.7	38±11	36±10	18± 5
	5.8±1.7	37±11	35±10	18± 5
$^{32}S(\gamma,p_0)^{31}P$[a]				~25
Sum Rule (μb/MeV)		15.8	16.8	32.6

Methods:
A. Analysis of third order fits
B. Analysis of fourth order fits
C. Analysis of fourth order fits, a_1 and b_1 excluded
D. Analysis of fourth order fits with one M1 amplitude

[a]Glavish et al., 1974, energy range: 15-20 MeV

the centroid. Direct E2 strength is expected to rise smoothly with energy through the region of the GDR; however, the E2 cross section obtained from the T-matrix analysis shows an excess of strength in the region from 14.5 to 19 MeV excitation energy. Since the work of Kiss et al. suggests that the GQR may be peaked somewhat below the predicted location of the centroid ($Ex=58/A^{1/3}$), the results of the present experiment suggest that the isoscalar giant quadrupole resonance has been observed near 17 MeV.

Chapter VI

THE ISOVECTOR QUADRUPOLE RESONANCE

A. Theoretical Predicitions and Historical Background

Bohr and Mottelson (1975) have predicted the existence of the isovector component of the giant quadrupole resonance (GQR) centered at an excitation energy of $135/A^{1/3}$ MeV for A~100. A collective resonance was first observed in this energy region by inelastic electron scattering on ^{90}Zr at 28 MeV excitation (Fukuda and Torizuka, 1972) and ^{208}Pb at 22 MeV (Nagao and Torizuka, 1973). Inelastic electron scattering, however, does not lead to a unique multipole assignment; the resonance could be either E2 or E0. Snover et al. (1974) have used radiative proton capture on ^{208}Pb to study the region above the giant dipole resonance of ^{209}Bi. They measured the E1-E2 interference as obtained from the fore-aft asymmetry of the cross section and observed an interference effect which was consistent with a quadrupole resonance at 22.9 MeV. This was said to be in agreement with the resonance occuring in ^{208}Pb, leading to an E2 multipole assignment, since E0 cannot be observed in the proton capture reaction. The results of a recent radiative capture experiment, $^{88}Sr(p,\gamma_0)^{89}Y$ (Ledford, 1976), suggest the

existence of an E2 resonance at an excitation energy of 28.8 MeV in ^{89}Y. This results is in reasonable agreement with the observation of a resonance at 28±1 MeV in ^{89}Y by inelastic electron scattering (Buskirk et al., 1976). All of these resonance energies fall within the range of $125\text{-}135/A^{1/3}$ and are consistent with the theoretical prediction. Thus, it is reasonable to investigate the possibility of an isovector quadrupole resonance in ^{31}P. If the location of the GQR is assumed to scale for light nuclei as the GDR energy does, then the predicted location of the resonance will be at $130(63/80)A^{1/3}$ MeV, about 33 MeV for ^{31}P.

B. Analysis of Data

As discussed in Chapter V, A, the fore-aft asymmetry, and A_o, the total cross section, were measured via three point angular distributions of cross sections of the $^{30}Si(p,\gamma_1)^{31}P$ reaction at E =16.8 MeV and in 1 MeV steps from 18 to 27 MeV. Although there was too little yield in the γ_o channel to allow the analysis of the ground state resonance, it was possible to extract the γ_1 yield and analyze the resonance built upon the first excited state of ^{31}P. By describing the resonance in terms of observed gamma ray energy, which is equivalent to the excitation above the first excited state, the results of the following analysis may be directly compared to the theoretical prediction given above.

A simple analysis of the total cross section and fore-aft asymmetry, suggested in part by the work of Snover et al. (1974), provides evidence of the existence of the isovector giant quadrupole resonance in ^{31}P. Following the notation of Snover et al., the E1 amplitudes are written

$$D(\ell_j)\, exp\left[i\, \phi_0 (\ell_j) \right]$$

where l and j are the orbital and total angular momentum in the incoming channel. The E2 amplitudes are

$$E(\ell_j)\, exp\left[i\, \phi_E (\ell_j) \right] + \frac{F(\ell_j)\, exp\left[i\, \phi_F (\ell_j) \right]\, i\, \Gamma/2}{E_p - E_R + i\, \Gamma/2}$$

where E represents the non-resonant amplitudes and F represents a collective resonance which is assumed to have a Breit-Wigner shape of width Γ and resonant energy E_R. The total cross section, A_0, is obtained from the sum of the squares of these amplitudes

$$A_0 = \sum_{\ell, j} \left[D^2(\ell_j) + E^2(\ell_j) + F^2(\ell_j)\ \frac{(\Gamma/2)^2}{(E_p - E_R)^2 + (\Gamma/2)^2} \right].$$

The summation is over all incoming channels that may decay to the first excited state by emission of a gamma ray. The statistical factors have been included in the amplitudes.

The fore-aft asymmetry, A, is made up of the interference terms that are contained in A_1 and A_3 and is written as

$$A = \sum_{l_j l'_{j'}} \Big[C(l_j l'_{j'})\, D(l_j)\, E(l'_{j'}) \cos\Delta\varphi_{DE} + C(l_j l'_{j'})\, D(l_j)\, F(l'_{j'}) \frac{\cos(\Delta\varphi_{DF} - \theta)}{\left((E_p - E_R)^2 + \Gamma^2/4\right)^{1/2}}$$

where

$$\theta = \tan^{-1}\left(\frac{E_p - E_R}{\Gamma/2}\right)$$

and is described as the resonance phase. The C's represent angular momentum coupling coefficients.

The first excited state of ^{31}P has $J = 3/2^+$, and there are three E1 amplitudes and 4 E2 amplitudes possible. Thus, even if polarized beam were available at these energies, it would still be impossible to solve for all of the amplitudes and phases. Therefore, to perform the analysis, all of the E1 amplitudes are represented by a single amplitude and phase. Similarly, the direct E2 and resonance E2 terms must each be combined into single terms. Then

$$A_o = N_1 e^{-N_6 E_p} + N_2 \frac{\Gamma^2/4}{(E_p - E_R)^2 + \Gamma^2/4} .$$

Here the E1 cross section is represented by a decaying exponential and the E2 cross section is represented by a resonance. The direct E2 cross section is assumed to contribute only a few percent to A_o and has not been separately indicated here. N_1 and N_2 are the strengths of the E1 and E2 cross resonance cross sections, repectively. The fore-aft asymmetry, normalized by dividing by A_o, is expressed as

$$A/A_o = (N_3 E_p + N_4) + \frac{N_5 (N_1 e^{-N_6 E_p})^{1/2} \left(\frac{N_2 \Gamma^2/4}{(E_p - E_R)^2 + \Gamma^2/4}\right)^{1/2} \cos(\Delta\phi_{DF} - \theta)}{A_o} .$$

Here, a linear term is used to describe the interference between the E1 and non-resonant E2 amplitudes. The second term comes from the interference between the E1 and resonance E2 amplitudes. N_5 represents the angular momentum coupling coefficients. $\Delta\phi_{DF}$ is the relative E1-E2 phase and is suggested by the data to be about 90°. Therefore $\cos(\Delta\phi_{DF} - \theta)$ becomes $\sin(\theta)$, where, again, θ is the resonance phase.

C. Results

The measured normalized fore-aft asymmetry, A/A_o, and the total cross section, A_o, were fit to the above equations by a chi-square minimization procedure (Rosenbrock, 1960), where Γ, E_R, and the parameters labeled N_i were the fitting parameters. The data and the fits are shown in fig. 27. The resonance is evident both in the fit to the cross section and in the interference effect observed in the fore-aft asymmetry. The exponentially decaying E1 strength and the E2 resonance are shown separately as well as summed together in the fit to the cross section. The straight line in the upper portion of the figure represents the linear term which arises from the interference of the E1 and non-resonant E2 amplitudes. The resonance is centered at the point where the fit to the asymmetry crosses the line; this energy, 30.8 MeV excitation, is somewhat lower than the predicted value of 33 MeV. The width obtained from the fits was 7.3 MeV. The other parameters were $N_1 = 115 \mu b$, $N_2 = 0.31 \mu b$, $N_3 = 0.024$ MeV^{-1}, $N_4 = -0.0049$, $N_5 = 0.418$, and $N_6 = 0.195$ (MeV)$^{-1}$.

The resonance may be integrated and compared to the $\Delta T=1$ E2 energy weighted sum rule (see Chapter V). The integrated strength is 0.84 μb/MeV, which corresponds to 5% of the sum rule. This strength is comparable to the percentage of the dipole sum seen in this reaction. If the collective isovector quadrupole strength is assumed to be distributed in various

Figure 27. The cross section and fore-aft asymmetry of the reaction $^{30}Si(p,\gamma_1)^{31}P$ in the region of the isovector giant quadrupole resonance. The curves in the lower portion of the figure show the fitted resonance and the exponentially decaying E1 cross section separately as well as added together. In the upper portion, the straight line indicates the asymmetry obtained from the interference of the E1 and non-resonant E2 backgrounds, while the curve shows the total fit to the asymmetry. The fitting procedure is described in the text. The error bars indicate the statistical error associated with the data points.

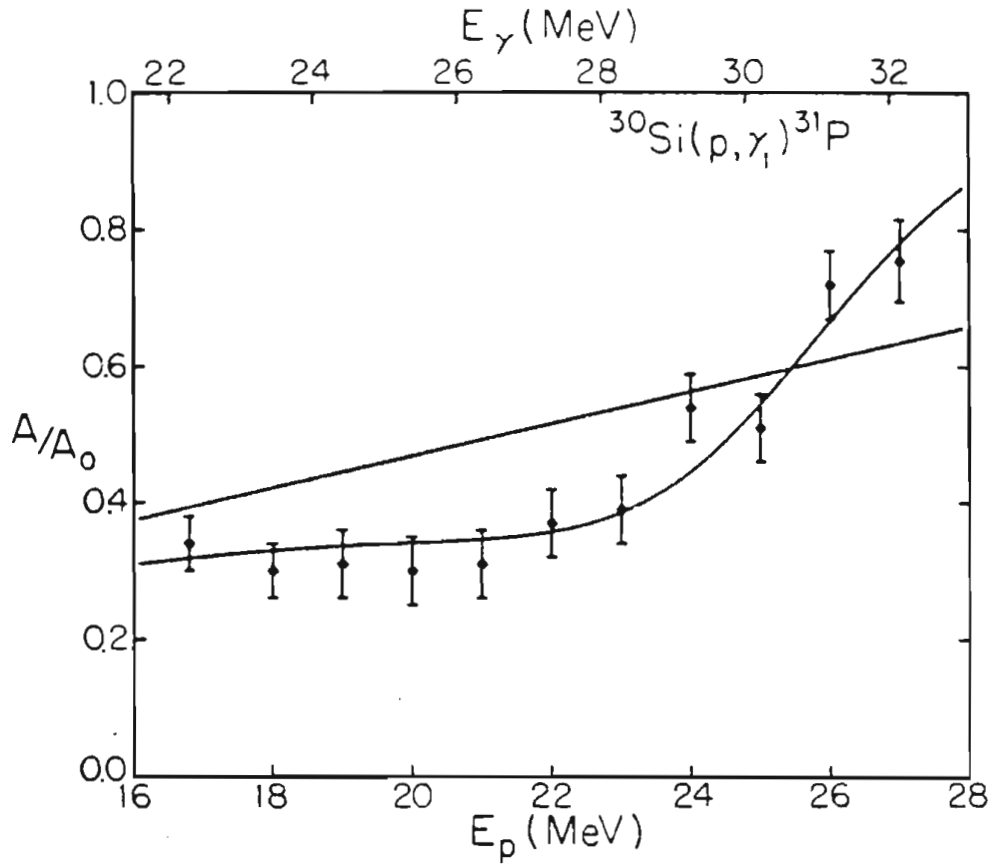
E_γ (MeV)
22
24
26
28
30
32
1.0
0.8
0.6
0.4
0.2
0.0
A/A_0
$^{30}Si(p,\gamma_1)^{31}P$
16
18
20
22
24
26
28
E_p (MeV)

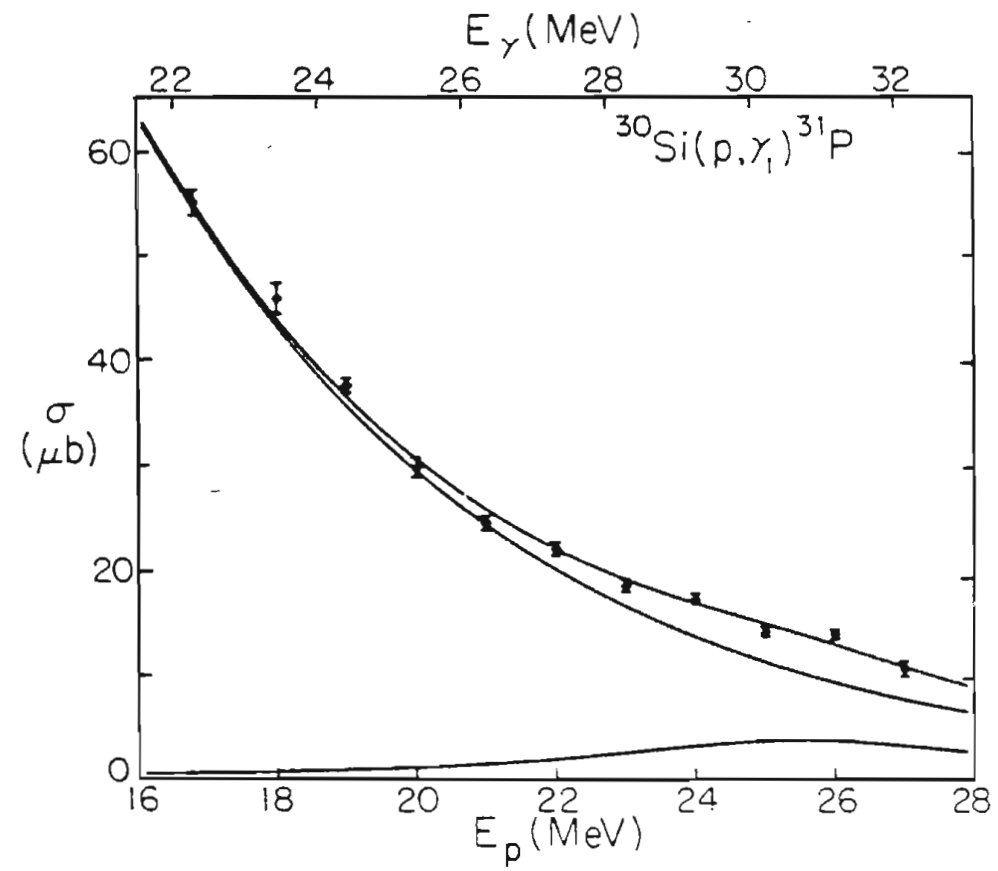
E_γ (MeV)
22
24
26
28
30
32
60
40
20
0
σ (μb)
$^{30}Si(p,\gamma_1)^{31}P$
16
18
20
22
24
26
28
E_p (MeV)

channels in the same proportion as the dipole strength, then the magnitude as well as the shape of the observed strength strongly suggests the existence of the isovector giant quadrupole resonance in ^{31}P.

Chapter VII

SUMMARY OF RESULTS AND CONCLUSIONS

The giant dipole resonance region of ^{31}P has been studied with the $^{30}Si(p,\gamma_0)^{31}P$ reaction. The fraction of the classical dipole sum rule observed in the energy region studied is 5.4%. A comparison of the excitation function of $^{31}P(p,\gamma_0)^{30}Si$ with the excitation function of the $^{31}P(\gamma,n_0)^{30}P$ reaction (Gellie et al., 1973) qualitatively supports the predictions of the theory of isospin splitting. A comparison of the excitation functions as well as the a_k and b_k coefficients obtained from angular distributions of cross section and analyzing power of the reactions $^{30}Si(p,\gamma_0)^{31}P$ and $^{31}P(p,\gamma_0)^{32}S$ (Dearnaley et al., 1965 and Glavish et al., 1974) suggests that the resonances are quite similar in behavior. This is consistent with the assumption that the major difference between the resonances of ^{31}P and ^{32}S is a spectator $s_{1/2}$ hole. In both ^{31}P and ^{32}S, there is a region of strength observed below 16 MeV excitation which seems to be due to some phenomenon other than the giant dipole resonance.

The E2 cross section was obtained from a transition matrix analysis of the angular distributions of cross section and

analyzing power of the $^{30}Si(p,\gamma_0)^{31}P$ reaction. Depending upon whether a_4 and b_4 are included in the fits or are taken to be zero, the cross section obtained accounts for about 3% or 18% of the total energy weighted quadrupole sum rule. The E2 strength is observed to be strongest in the region below 17 MeV excitation, which is somewhat below the predicted location of the isoscalar giant quadrupole resonance. The results of an inelastic alpha particle scattering experiment on ^{27}Al (Kiss et al., 1976) show that the GQR of ^{27}Al is peaked somewhat below the predicted location, thus leading to the conclusion that the E2 strength observed in the present experiment is consistent with the observation of the isoscalar giant quadrupole resonance. The fore-aft asymmetry is also peaked near 17 MeV and is observed to rise gradually above that point, suggesting that the strength in the higher energy region is mostly direct. The E1 amplitudes obtained from the T-matrix analysis are fairly constant over the region of the giant dipole resonance although there may be a crossing of the two solutions obtained near 17.5 MeV.

The giant resonance that is built upon the first excited state of ^{31}P was also studied through the detection of γ_1. The fraction of the classical dipole sum rule observed in the energy region studied is 7.5%. The T-matrix analysis of the E1 amplitudes showed that the spin-flip amplitude could not be neglected, as was possible in previous works (see Appendix B); however, a set of solutions was obtained for which the contri-

bution of the spin-flip amplitude was small. These results showed that the E1 amplitudes remained fairly constant over the region of the GDR.

The behavior of the E2 strength in the region above the GDR, as observed in the $^{30}Si(p,\gamma_1)^{31}P$ reaction, was deduced from the fore-aft asymmetry. The asymmetry is observed to rise gradually through the region of the giant dipole resonance, suggesting that the origin of the E2 radiation in that region is mostly direct. Above the GDR, however, a strong interference effect is observed in the asymmetry. This effect was shown to be consistent with the observation of the isovector giant quadrupole resonance near 31 MeV excitation. From the total cross section data, the resonance observed was shown to account for 5% of the $\Delta T=1$ energy weighted quadrupole sum rule.

Appendix A

TARGET PREPARATION

The silicon dioxide targets were prepared by evaporation of enriched (>95%) $^{30}SiO_2$, obtained from Oak Ridge National Laboratory. Trial and error showed that the thickest targets could be made by evaporation directly onto mounted carbon foils; thick self-supporting foils could not be floated from the glass slides. The technique for preparing self-supporting foils has been described previously (Hilko, 1974).

The silicon dioxide was mixed with carbon powder to reduce the silicon dioxide to silicon monoxide during evaporation. As indicated in Chapter II, the targets did not seem to have been reduced as much as expected. The carbon powder was scraped with a metal spatula from a good quality graphite block. Before mixing with the carbon, the small silicon dioxide crystals were crushed into fine powder. In order to avoid the loss of isotope, the crystals were placed in an empty isotope bottle and were crushed with a metal spatula. The isotope was weighed on weighing papers and mixed in the amount of 170 mg silicon dioxide with 90 mg of carbon. The mixture was then placed in a watch glass and further ground with a pestle. The mixture was

repeatedly broken up and mixed with the spatula and further ground with the pestle. A mortar was not used since experience showed that too much of the mixture stuck to the surface of the mortar.

When the mixture was converted to a very fine powder, it was ready to be placed in the boat. The boat was made from a 3 cm long, 10 mil wall, 0.25" O.D. tempered tantalum tube. A hole was drilled in the center of the tube with a no. 68 bit. One end of the boat was then crimped tightly closed perpendicular to the axis of the hole, and the mixture was transferred into the tube. A weighing paper was useful for transferring the mixture. The other end of the tube was then crimped closed. The length of the crimped area was about 0.5 cm. The drill bit was inserted into the hole again to insure that the hole was not blocked.

The target rings used were of the standard TUNL design with a 7 mm hole, but were made from aluminum. These rings have holes which are tapered. The side of the ring which has the smaller hole was sanded lightly and cleaned with alcohol. An approximately 10$\mu g/cm^2$ carbon foil was then floated onto the roughened side of the ring. No adhesive was used since the carbon foils stick nicely when dry. Foils which were not flat and free of defects were discarded.

Before placing the boat and mounted carbon foils in the evaporator, the evaporator was thoroughly cleaned and dried with alcohol. The boat was fastened tightly into the elec-

trodes; if the entire end of the boat was not in good contact with the electrode, local heating took place at the end of the boat. The short electrodes were used with the boat fastened to the tip of one electrode and to the side of the other. The target rings were placed in a holder 2.5 cm above the top of the boat with the foil side pointed away from the boat. An array of target rings was put in place, with one mounted directly above the hole in the boat. The center foil received most of the evaporation product.

The evaporation procedure required several hours to perform. The evaporation current had to be raised slowly or sudden temperature changes and poor vacuum caused the targets to break. Starting at 50 A, the current was raised in 10 A steps, with the pressure maintained below 10^{-5} Torr. At about 180 A, or 1350°C, the pressure rose as the evaporation began. The temperature of the center of the boat was monitored with an optical pyrometer. The current was then raised in 1 to 2 A steps, with the pressure maintained below 10^{-4} Torr. These steps required about 15 minutes each. It is not possible to precisely describe the point at which the evaporation was stopped. As the evaporation ended, increasing the current did not increase the pressure. For one of the targets made, the temperature was raised to 1525°C (215 A). At that time, two of the foils mounted to the side of the center target broke. The temperature was then lowered by about 15 A over the next few seconds. When the other target was being made, three of the side foils

broke at 1475°C (195-200 A). Again, the current was lowered about 15A over the next few seconds. In both cases, the current was then lowered slowly, taking about an hour to reach 50 A, and then turned to zero. The assembly was allowed to cool for a couple of hours, and then the evaporator was let up to atmospheric pressure with dry argon gas.

As indicated, the side foils tended to break at the high temperatures. It may be luck that the center foils survived, or it may be that stress built up in the side foils due to the nonuniform distribution of evaporated material. In any case, extreme care should be taken at high temperatures. Some practice with natural silicon dioxide is recommended first, although it does not behave in precisely the same way as the pure isotope.

Appendix B

GIANT RESONANCES IN ^{55,57,59}Co USING POLARIZED PROTON CAPTURE

Giant dipole resonances in ^{55,57,59}Co using polarized proton capture

C. P. Cameron, N. R. Roberson, D. G. Rickel, and R. D. Ledford
Duke University and Triangle Universities Nuclear Laboratory, Duke Station, Durham, North Carolina 27706*

H. R. Weller† and R. A. Blue
University of Florida† and Triangle Universities Nuclear Laboratory, Duke Station, Durham, North Carolina 27706*

D. R. Tilley
North Carolina State University and Triangle Universities Nuclear Laboratory, Duke Station, Durham, North Carolina 27706*

(Received 8 January 1976)

The angular distributions of cross sections and analyzing powers have been measured for the ^{54,56,58}Fe$(\vec{p},\gamma_0)$ reactions throughout the giant dipole resonance regions of ^{55,57,59}Co. In addition, the 90° yield curve has been measured for the ^{58}Fe$(p,\gamma_0)^{59}$Co reaction for E_p from 5.0 to 16.0 MeV in 100 keV steps. The data are analyzed to deduce the amplitudes and phases of the T matrix elements involved. The preferred solution indicates that the major change occurring in crossing the giant dipole resonance occurs in the relative phase between the $d_{5/2}$ and $g_{9/2}$ amplitudes. The implications of these results are discussed *vis à vis* the isospin splitting of the giant dipole resonance.

[NUCLEAR REACTIONS ^{54}Fe$(\vec{p},\gamma_0)$, ^{56}Fe$(\vec{p},\gamma_0)$, ^{58}Fe$(\vec{p},\gamma_0)$; measured $\sigma(\theta)$ and $A(\theta)$, E_p=8.0–15.0 MeV, E_p=8.0–14.5 MeV, and E_p=7.6–15.0 MeV, respectively. ^{58}Fe(p,γ_0) measured $\sigma(90°)$, E_p=5.0–16.0 MeV. Deduced T-matrix amplitudes and phases in all three cases. Discussed isospin splitting.]

I. INTRODUCTION

The giant dipole resonance (GDR) regions of ^{55,57}Co have been previously studied by means of the ^{54,56}Fe(p,γ_0) reactions.[1] In this previous work it was observed that the a_4 coefficients obtained from the measured angular distributions were, in general, positive at the low energy side of the GDR and negative at the high energy side. It was suggested that this behavior was probably correlated with the fact that the GDR of the Co isotopes might be expected to be split[2] into two isospin components ($T_<$ and $T_>$). Isospin splitting of the giant dipole resonance has been reported in a number of nuclei[3–6]; however, the problem of clearly identifying the $T_>$ and $T_<$ components of the GDR as two possibly overlapping peaks (envelopes of strength) in the excitation function is as yet unsolved. Indeed, as an alternative example, deformation splitting, as calculated with the hydrodynamic model, also leads to a prediction of two peaks of strength.[7] In addition, the spreading of one or both components could be so severe as to make any attempt to define a centroid, or centroids, meaningless.

The utility of polarized proton capture in studying the GDR region of nuclei has been previously demonstrated.[5,8] In the present work, angular distributions of cross sections and analyzing powers have been measured for polarized proton capture on the three targets ^{54}Fe, ^{56}Fe, and ^{58}Fe at energies which encompass the GDR. The measurements of $\sigma(\theta)$ and $A(\theta)$ were made at five angles: 50°, 70°, 90°, 110°, and 130°. In addition, $\sigma(90°)$ was measured for ^{58}Fe$(p,\gamma_0)^{59}$Co in 100 keV steps from 5.0 to 16.0 MeV.

The compound nuclei studied all have ground state spins of $\frac{7}{2}^-$ and so the GDR can have J^π of $\frac{5}{2}^+$, $\frac{7}{2}^+$, or $\frac{9}{2}^+$. The angular distribution and asymmetry data are analyzed to deduce the relative amplitudes and phases of the three contributing T-matrix elements in this problem. As one crosses the GDR region the major change in these parameters occurs in the relative phase between the $d_{5/2}$ and $g_{9/2}$ amplitudes. The fact that the relative amplitudes are essentially constant suggests that the configurations of the GDR as seen in the (γ,p_0) channel are not changing drastically.

II. EXPERIMENTAL DETAILS

The experimental details of the present work are basically identical to those described in a previous paper.[9] Only the essential and unique features of the present work will be described here.

The γ rays were detected using a 25.4 cm × 25.4 cm NaI crystal assembly which incorporates a plastic anticoincidence shield. In the present work, the shield gain was set high so as to reject the major portion of the escape peaks. In addition, signals from a light emitting diode (LED) light pulser were collected by the on-line computer and

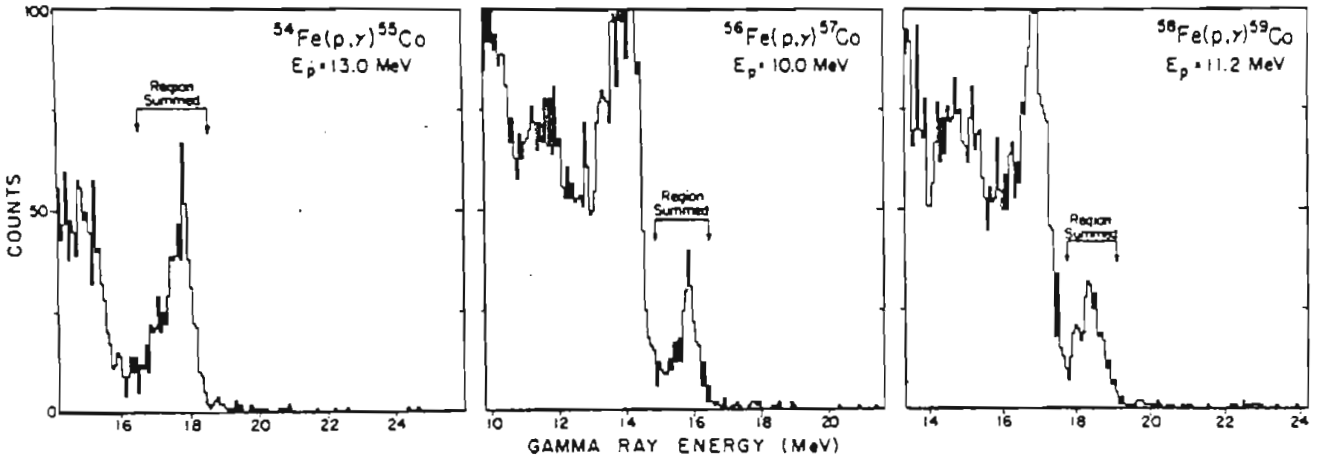

FIG. 1. Typical γ-ray spectra obtained with the NaI spectrometer.

utilized to gain stabilize the spectrometer. The front face of the crystal was positioned 56 cm from the target which corresponds to a total angular acceptance of 18°. Typical spectra for the three isotopes studied (^{55}Co, ^{57}Co, and ^{59}Co) are shown in Fig. 1. The region summed to obtain the γ_0 yield is shown for each case.

The Fe targets for these measurements were prepared at Oak Ridge National Laboratories.[10] The ^{54}Fe target was 4.0 mg/cm^2 thick (97.12% enrichment) and contained 2.88% ^{56}Fe. The ^{56}Fe target was 3.9 mg/cm^2 (99.93% enrichment). For the case of ^{58}Fe, the 4.0 mg/cm^2 thick target was 82.5% ^{58}Fe, 15.8% ^{56}Fe, and 0.5% ^{54}Fe. These target thicknesses correspond to a proton energy loss of about 120 keV for 10 MeV protons. The target thicknesses reported by Oak Ridge were found to be accurate to within 10% by means of elastic scattering measurements.[11] These target thicknesses were combined with the measured detection efficiency[9] and the solid angle to determine the absolute cross sections reported in this work. The error in the ^{58}Co absolute cross sections reported here is estimated as being ±15%.

The asymmetry data were measured with protons from the Lamb-shift polarized-ion source[12] at the Triangle Universities Nuclear Laboratory (TUNL). The polarization of the protons, determined at 20 min intervals by the quench-ratio technique,[13] was found to be essentially constant during the course of a run with a typical value of 0.80 ± 0.02. The beam current on target was in the 40–80 nA range. Measurements were obtained by running the beam alternately in the spin up and spin down modes.

III. ANALYSIS OF DATA

Since the γ ray peaks corresponding to the (p,γ_0) transitions were resolved and essentially free of background, the spectra were readily processed by summing the regions shown in Fig. 1. The angular distributions were fitted using a least squares criterion by an expansion in terms of Legendre polynomials

$$\sigma(\theta) = a_0\left[1 + \sum_k \frac{a_k}{a_0} Q_k P_k(\cos\theta)\right],$$

with the proper statistical errors, geometrical correction factors (Q_k) resulting from the finite detector size, and center of mass corrections taken into account.

The asymmetry measurements are presented in terms of the quantity $\sigma(\theta)A(\theta)/a_0$, where

$$A(\theta) = \left(\frac{N_+ - N_-}{N_+ + N_-}\right)\frac{1}{P}.$$

N_+ and N_- are the number of counts obtained for the spin up and spin down measurements, respectively. The quantity P denotes the beam polarization. The product of the analyzing power and the cross section was fitted by an expansion in associated Legendre polynomials

$$A(\theta)\sigma(\theta)/a_0 = \sum_k b_k Q_k P_k^1(\cos\theta).$$

The statistical errors, the geometrical factors Q_k, the geometrical effects due to the azimuthal angular range, and the center of mass corrections were all taken into account.

Each set of data was fit including one, two, three, and four terms (i.e., up to and including P_3 and P_4^1, respectively). The normalized χ^2 values obtained from these fits indicated that for the cross section data the highest order term required at all but one of the energies studied was $P_2(\cos\theta)$, while for the asymmetry measurements the highest order term which was found to be statistically justified was $P_3^1(\cos\theta)$.

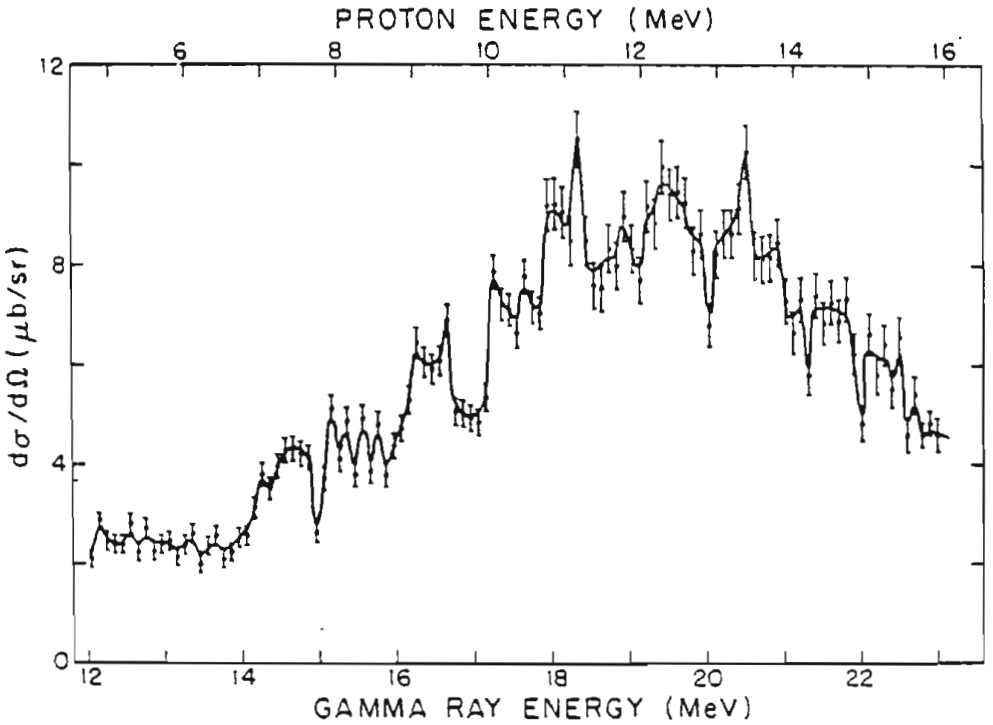

FIG. 2. The 90° yield curve for ^{58}Co$(\gamma,p_0)^{58}$Fe obtained by the principle of detailed balance from the ^{58}Fe$(p,\gamma_0)^{59}$Co reaction. The error bars represent the statistical error associated with the data points. The solid curve is a smooth line drawn through the data points. The energies given are the center of target energies.

IV. RESULTS

The yield curve measured at 90° for ^{58}Fe$(p,\gamma_0)^{59}$Co is shown in Fig. 2. The 90° yield curves for the ^{54}Fe$(p,\gamma_0)^{55}$Co and ^{56}Fe$(p,\gamma_0)^{57}$Co experiments have been previously reported in Ref. 1. The present data are plotted in Fig. 3 along with the data from Ref. 1 for comparison; all three cases have been averaged over a 500 keV interval. The locations of the division between the $T_<$ and $T_>$ components, as suggested in Ref. 1, are identified with an arrow for ^{55}Co and ^{57}Co. The first visible difference in the three cases is the width of the entire resonance envelope. It is seen that the distribution of strength as a function of E_γ tends to increase in width from ^{55}Co to ^{59}Co.

The theory of isospin splitting of the giant dipole resonance has been developed by Fallieros and others.[14-17] Simple expressions are given[17] for the relative strengths and splittings of the $T_<$ and $T_>$ components of the GDR. The estimate of the relative strengths is

$$\frac{S(T_0+1)}{S(T_0)} \cong \frac{1}{T_0}\left[\frac{1-\frac{3}{2}(T_0/A^{2/3})}{1+\frac{3}{2}(1/A^{2/3})}\right],$$

where T_0 is the isospin of the ground state of the nucleus, and the estimate of the splitting between the $T_<$ and $T_>$ components[15] is

$$\Delta E = \frac{60(T_0+1)\ \text{MeV}}{A}.$$

This splitting can also be compared to the deformation splitting[7] which is calculated from the experimentally determined ground state quadrupole moments[19,20] and from the expressions[18]

$$\frac{E_b}{E_a} = 0.911\frac{a}{b} + 0.089,$$

where E_a and E_b are the resonance energies corresponding to the long and short axes a and b, and

$$Q_0 = \tfrac{3}{5}(r_0)^2 A^{2/3} Z \frac{d^2-1}{d^{2/3}},$$

where $d = a/b$. One can also consider the results of the isospin Clebsch-Gordan coefficients alone, as in Ref. 1. If it is assumed that the (γ,n) and (γ,p) reactions take up all of the reaction cross section then, for the (γ,p) reaction, the ratio of $T_>$ to $T_<$ strengths is given by

$$\frac{S(T_>)}{S(T_<)} = \frac{4T_0+3}{T_0(2T_0+1)}.$$

The evaluation of these expressions is summarized in Table I.

The results of Table I indicate that we should expect to see the isospin splitting increase as we go from ^{55}Co to ^{59}Co while, at the same time, the relative strength of $T_<$ component should increase dramatically. The splitting allowed by the data could be imagined to increase (see Fig. 3), since the GDR spreads out as we go from ^{55}Co to ^{59}Co.

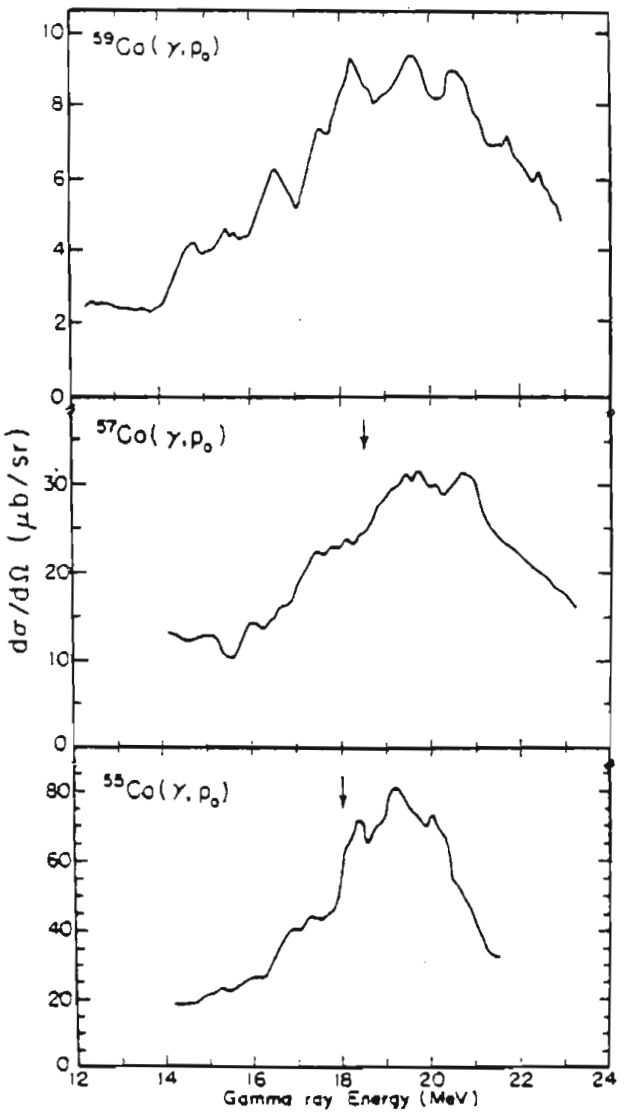

FIG. 3. The 90° yield curves for the ^{54,56,58}Fe(p,γ) reactions after averaging over a 500 keV interval. The arrows indicate the energy of the splitting between the $T_<$ and $T_>$ components of the GDR as suggested in Ref. 1.

The strengths, however, do not appear to follow the behavior suggested in Table I in any quantitative way. What appears to be more reasonable is to acknowledge the possibility that the $T_>$ and $T_<$ components are largely mixed and overlapping in these nuclei. The values obtained from the hydrodynamic model do not rule out the possibility that deformation splitting may be observed in the data of Fig. 3. Although this model does not account for the trend towards greater spreading in ^{58}Co, it does predict that the upper region should contain twice as much strength as the lower region.[7] This prediction of relative strength is in better accord with the data than the predictions of relative strengths due to isospin splitting.

Another test for isospin splitting can be made by comparing the (γ,p) and (γ,n) data.[2,21] This is done for ^{59}Co in Fig. 4 where the present ^{59}Co(γ,p_0) data are shown with the previously measured ^{59}Co(γ,n) data.[22] In this case, as in the case of ^{60}Ni discussed by Paul,[2] while some suggestion of a favored population of the $T_>$ states in the (γ,p_0) data may be present, no clear indication of isospin splitting is obvious. Of course, the fact that the (γ,n) data includes all outgoing neutrons complicates this comparison.

Another suggestion made in Ref. 1 was that the observed behavior of the a_2 coefficient might be correlated with the isospin splitting in ^{55}Co and ^{57}Co. Specifically, it was observed that a_2 went from a positive to a negative number near the energy where one might expect the $T_<$ and $T_>$ components to be divided. It would seem plausible to assume that if one could show that the amplitudes of the T-matrix elements involved in the capture process changed, it could indicate a structural change which might be associated with the isospin quantum number. As is shown below, however, the behavior of a_2, when combined with the polarization data, can be explained without any significant abrupt change in the amplitudes which contribute to the capture process.

The data of Fig. 2 and Ref. 1 can also be examined to see what fraction of the classical $E1$ sum rule $\int\sigma(\gamma,x)dE = (60NZ/A)$ mb MeV is exhausted in the three nuclei. The results are: ^{55}Co, 0.64%; ^{57}Co, 0.35%; and ^{59}Co, 0.09%. The results for ^{55}Co and ^{57}Co are taken from Ref. 1. The results for ^{59}Co were obtained by integrating our 90° yield curve over the energy range studied, modulated by the ratio of integrated cross section to $\sigma(90°)$ obtained from the angular distribution measurements. A comment on why these values are especially small has been presented in Ref. 1.

TABLE I. Summary of the predicted relative strengths and splitting of the GDR. The expressions in column 1 are defined in the text.

	^{55}Co	^{57}Co	^{59}Co
$\frac{S(T_>)}{S(T_<)}$ [a]	5.0	1.5	0.87
$\frac{S(T_0+1)}{S(T_0)}$ [b]	1.7	0.62	0.33
ΔE (MeV)	1.64	2.63	3.56
$\frac{E_b}{E_a}$		1.22	1.15
(E_b-E_a) (MeV)		3.9 [c]	2.9 [d]

[a] Reference 1.
[b] Reference 17.
[c] If $E_a = 17.5$ MeV.
[d] If $E_a = 18.0$ MeV.

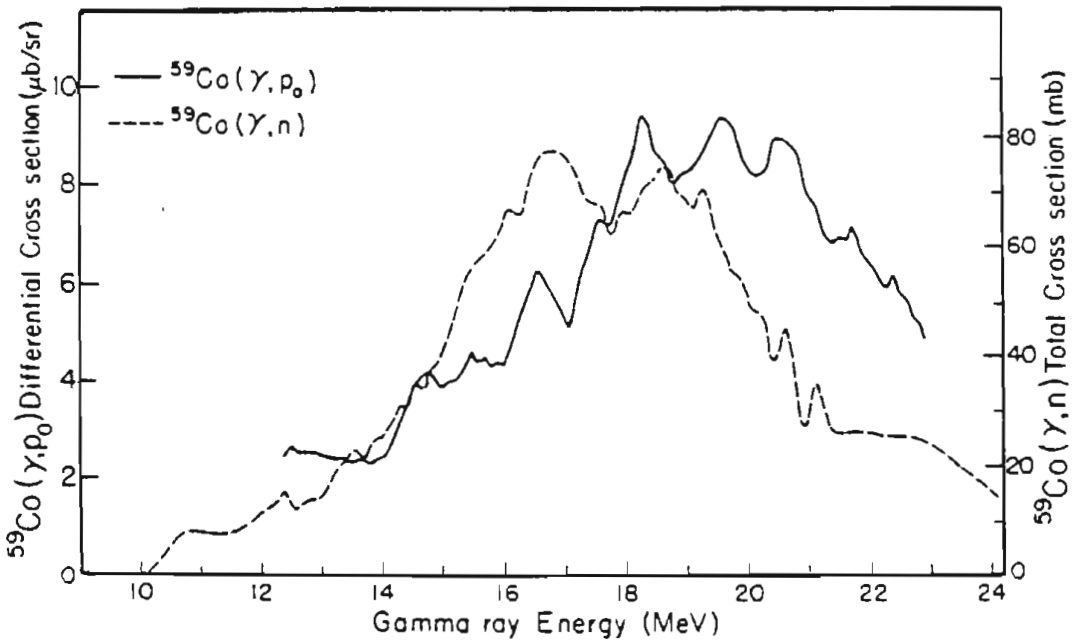

FIG. 4. The present (averaged) data for the ^{58}Fe$(p,\gamma_0)^{59}$Co reaction [shown as ^{59}Co$(\gamma,p_0)^{58}$Fe via detailed balancing] and the ^{59}Cp$(\gamma,n)^{58}$Co data of Ref. 22.

We would like to comment on the relative strengths seen in the three nuclei. Two obvious effects can be considered here: proton penetrabilities and the different target isospins. The penetrabilities were calculated from

$$P_l = \frac{kr}{F_l^2 + G_l^2},$$

where F_l and G_l are the regular and irregular Coulomb wave functions. If we anticipate the results of the T-matrix analysis discussed below, we may take the cross section to be due 50% to $l=2$ capture and 50% to $l=4$ capture as a representative case. The effects of the Q values (5.06 MeV, 6.02 MeV, and 7.38 MeV, respectively, for proton capture to ^{55}Co, ^{57}Co, and ^{59}Co) as seen in the proton penetrabilities is to diminish the cross section as we go from ^{54}Fe+p to ^{58}Fe+p. In addition, we can consider the effects of the different target isospins. The simplest consideration, the isospin Clebsch-Gordan coefficients, indicate that the relative strength of the $T_>$ component is given by $1/(2T_0+2)$. This implies that as T increases, the relative $T_>$ strength will decrease. If we also make the additional assumption that we are integrating mainly $T_>$ strength (which would be expected to be less spread out than the $T_<$ strength), then we would expect the integrated yield to go as $1/(2T_0+2)$. The results of these considerations are summarized in Table II. The experimental results were obtained by integrating the yield curves over the region of the main resonance for each isotope. These simple considerations agree remarkably well with the general trend of the data.

A sample of our angular distribution and asymmetry data is shown in Fig. 5, where we have presented $\sigma(\theta)/a_0$ and $A(\theta)\sigma(\theta)/a_0$ for three different energies and three different targets. Data were taken over the range of ~8 to ~15 MeV at five angles for each of the three targets. (The solid curves are the results of fitting these data

TABLE II. The relative experimental cross sections for the three isotopes studied compared with predictions based on penetrabilities and isospin.

	$\langle P_l \rangle$	$\frac{1}{2T_0+2}$	$\frac{\langle P_l \rangle}{2T_0+2}$	Cross section[a] (experimental)	Energy range integrated E_γ (MeV)
^{54}Fe+p	4.54	0.333	1.00[b]	1.00[b]	16.4–21.7
^{56}Fe+p	4.13	0.200	0.55	0.81	16.0–23.4
^{58}Fe+p	3.41	0.143	0.32	0.21	14.0–23.0

[a] Integrated over energy and angle.
[b] Normalized so that ^{54}Fe+p=1.0.

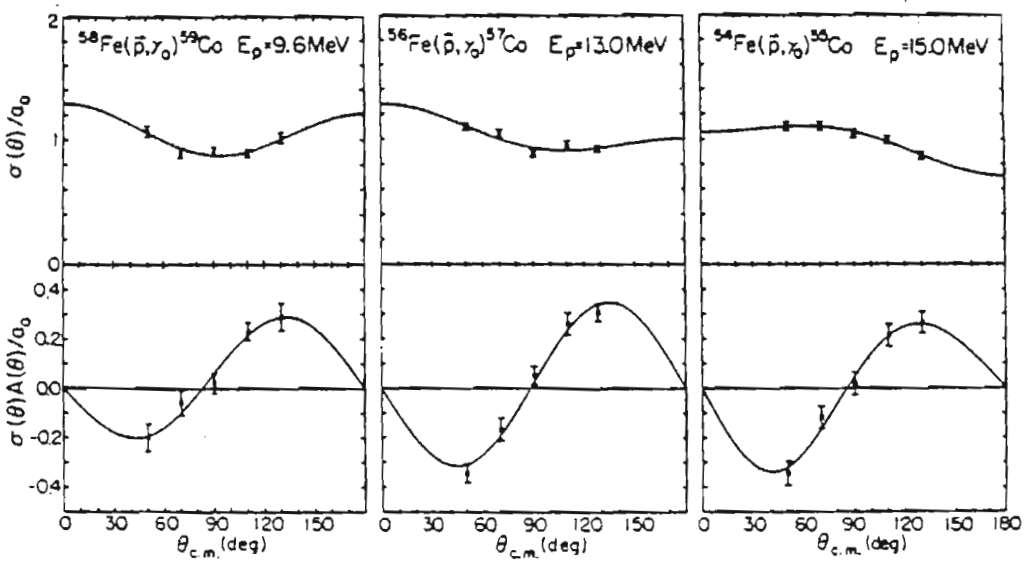

FIG. 5. Typical data at three energies for the quantities $\sigma(\theta)/a_0$ and $\sigma(\theta)A(\theta)/a_0$. The error bars represent the statistical errors associated with the data points. The solid curves are the result of fitting the data as described in the text.

TABLE III. The a and b coefficients obtained from least square fits to the data as described in the text. Higher order coefficients are given only when the criterion of normalized χ^2 justified the use of higher order terms.

E_p (MeV)	a_1/a_0	a_2/a_0	a_3/a_0	b_1	b_2	b_3
			^{54}Fe($\vec{p}$,γ_0)^{55}Co			
8.0	0.26 ± 0.06	0.11 ± 0.11		−0.03 ± 0.05	0.00 ± 0.04	−0.02 ± 0.04
9.0	0.20 ± 0.05	0.09 ± 0.10		−0.07 ± 0.04		
10.0	0.25 ± 0.04	0.03 ± 0.07		0.02 ± 0.03	−0.09 ± 0.02	
11.0	0.10 ± 0.03	0.24 ± 0.05		0.03 ± 0.02	−0.07 ± 0.02	
12.1	0.27 ± 0.05	0.18 ± 0.04	0.18 ± 0.07	0.01 ± 0.01	−0.12 ± 0.01	
13.0	0.01 ± 0.03	−0.09 ± 0.05		0.03 ± 0.02	−0.15 ± 0.01	
14.0	0.07 ± 0.03	0.0 ± 0.05		−0.02 ± 0.02	−0.16 ± 0.02	−0.02 ± 0.02
15.0	0.18 ± 0.03	−0.12 ± 0.06		0.01 ± 0.02	−0.20 ± 0.02	−0.03 ± 0.02
			^{56}Fe($\vec{p}$,γ_0)^{57}Co			
8.0	0.27 ± 0.06	0.03 ± 0.12		0.08 ± 0.05	−0.01 ± 0.04	
9.0	0.07 ± 0.04	−0.04 ± 0.08		−0.05 ± 0.03	−0.06 ± 0.02	−0.03 ± 0.02
10.0	0.08 ± 0.03	0.24 ± 0.06		0.05 ± 0.02	−0.08 ± 0.02	−0.02 ± 0.02
11.5	0.03 ± 0.03	0.20 ± 0.05		−0.08 ± 0.03	−0.09 ± 0.02	
13.0	0.14 ± 0.03	0.15 ± 0.05		0.02 ± 0.02	−0.22 ± 0.02	−0.03 ± 0.02
14.5	0.14 ± 0.04	−0.34 ± 0.08		0.10 ± 0.03	−0.21 ± 0.02	−0.04 ± 0.02
			^{58}Fe($\vec{p}$,γ_0)^{57}Co			
7.6	0.19 ± 0.05	0.19 ± 0.09		0.04 ± 0.03	−0.02 ± 0.03	
9.2	0.12 ± 0.04	0.28 ± 0.07		0.01 ± 0.03	−0.11 ± 0.02	
9.6	0.04 ± 0.04	0.26 ± 0.07		0.06 ± 0.02	−0.17 ± 0.02	
10.5	0.12 ± 0.04	0.15 ± 0.06		0.04 ± 0.02	−0.17 ± 0.02	0.04 ± 0.02
11.2	0.16 ± 0.04	0.09 ± 0.06		0.08 ± 0.02	−0.18 ± 0.02	
11.9	0.18 ± 0.05	−0.14 ± 0.09		0.03 ± 0.03	−0.20 ± 0.03	−0.04 ± 0.03
12.7	0.13 ± 0.05	−0.25 ± 0.09		0.07 ± 0.03	−0.23 ± 0.02	
13.5[a]	0.08 ± 0.09	−0.28 ± 0.09	0.00 ± 0.14	0.06 ± 0.03	−0.22 ± 0.02	
14.0[a]	0.14 ± 0.09	−0.47 ± 0.08	0.00 ± 0.13	0.08 ± 0.03	−0.20 ± 0.02	−0.04 ± 0.02
15.0[a]	0.08 ± 0.10	−0.29 ± 0.08	0.00 ± 0.15	0.10 ± 0.03	−0.23 ± 0.02	−0.03 ± 0.02

[a] The criterion of normalized χ^2 did not clearly indicate that a fit which included $P_3(\cos\theta)$ was statistically justified for these energies. The error given for a_1 and a_2 reflects this uncertainty.

as previously described.) The a and b coefficients obtained from the fits and tabulated in Table III exhibit three important features. First, the a_2 and b_2 coefficients are relatively significant as may be expected, since only these coefficients may be finite if there is pure $E1$ radiation. Second, almost all coefficients a_k and b_k, with $k>2$, are either zero or very small, which indicates that only dipole radiation is significant in the energy range studied. Third, the quantity and quality of the present data and the resulting knowledge of the coefficients a_3, a_4, and b_3, b_4 implies that only an $E1$ analysis is warranted.

Since the ground state spin of the three Co isotopes considered is $\frac{7}{2}^-$, there are three different J^π values which can decay by $E1$ radiation to the ground state: $\frac{5}{2}^+$, $\frac{7}{2}^+$, and $\frac{9}{2}^+$. Each of these decays may be represented by a transition matrix element labeled by the total angular momentum brought in by the proton. Since these T-matrix elements are complex, each will have an amplitude and a phase which we denote by $d_{5/2}$, $g_{7/2}$, and $g_{9/2}$, and $\phi(d_{5/2})$, $\phi(g_{7/2})$, and $\phi(g_{9/2})$, respectively.

We can now write down the expressions for the a_0, a_2, and b_2 coefficients:

$$a_0 = 3|d_{5/2}|^2 + 4|g_{7/2}|^2 + 5|g_{9/2}|^2 ,$$

$$a_2 = -0.42|d_{5/2}|^2 + 0.86|d_{5/2}|\,|g_{7/2}|\cos(d_{5/2},g_{7/2}) + 5.7|d_{5/2}|\,|g_{9/2}|\cos(d_{5/2},g_{9/2}) + 1.9|g_{7/2}|^2 - 1.26|g_{7/2}|\,|g_{9/2}|\cos(g_{7/2},g_{9/2}) - 1.66|g_{9/2}|^2 ,$$

$$b_2 = -1.0|d_{5/2}|\,|g_{7/2}|\sin(d_{5/2},g_{7/2}) + 1.9|d_{5/2}|\,|g_{9/2}|\sin(d_{5/2},g_{9/2}) - 1.9|g_{7/2}|\,|g_{9/2}|\sin(g_{7/2},g_{9/2}) ,$$

where $(d_{5/2}, g_{7/2})$ stands for $\phi(d_{5/2}) - \phi(g_{7/2})$, $(g_{7/2}, g_{9/2}) = \phi(g_{7/2}) - \phi(g_{9/2})$, and $(d_{5/2}, g_{9/2}) = \phi(d_{5/2}) - \phi(g_{9/2})$.

The solutions to these equations that are in agreement with the experimentally determined coefficients were found by a computer search over the amplitude and phase parameters. The $g_{9/2}$ and $g_{7/2}$ amplitudes were incremented through 20 approximately equal steps over their allowed range while the $d_{5/2}$ amplitude was determined by requiring that $a_0 = 1$. The phase differences $[\phi(g_{7/2}) - \phi(g_{9/2})]$ and $[\phi(d_{5/2}) - \phi(g_{9/2})]$ were stepped in increments of 10° from 0° to 360°. The values of a_2 and b_2 were calculated from each set of parameters and the parameters were accepted as a solution if the calculated a_2 and b_2 coefficients were within the errors of the experimental values. In addition, the value of χ^2 was calculated for each solution using the expression

$$\chi^2 = \left(\frac{a_2(\text{exp}) - a_2(\text{calc})}{\delta a_2(\text{exp})}\right)^2 + \left(\frac{b_2(\text{exp}) - b_2(\text{calc})}{\delta b_2(\text{exp})}\right)^2 ,$$

where the differences between the experimental (exp) and calculated (calc) coefficients have been divided by the error (δ) in the value of the experimental coefficients.

The results of this search are shown in Fig. 6 at three representative energies for ^{58}Fe + p. The accepted solutions are plotted as the phase differences and percentage of the cross section (i.e., the fraction of a_0) due to each amplitude as a function of the percentage due to the $g_{9/2}$ amplitude. Since we have five unknowns (one phase can be

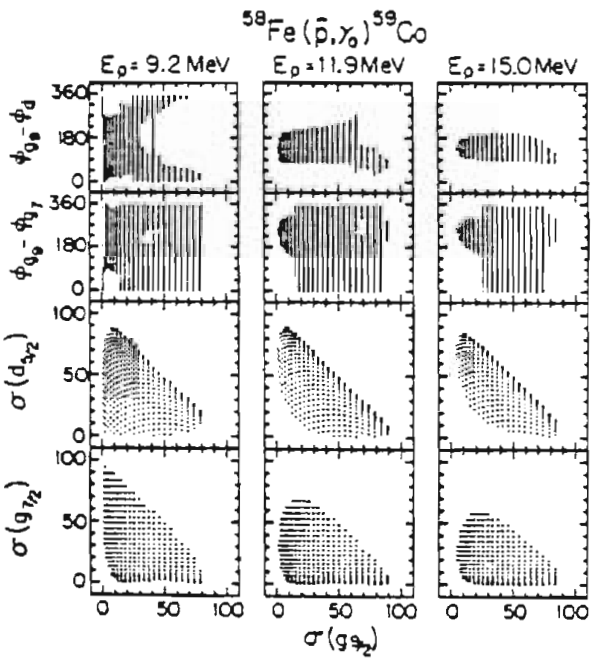

FIG. 6. The solutions at three representative energies for ^{58}Fe + p. Each solution, as represented by a solid dot, is plotted for those parameters for which the values of a_0, a_2, and b_2 obtained from the equations in the text agreed with the measured coefficients within experimental errors. The transition matrix element amplitudes are expressed in terms of the percent of the integrated cross section due to that amplitude.

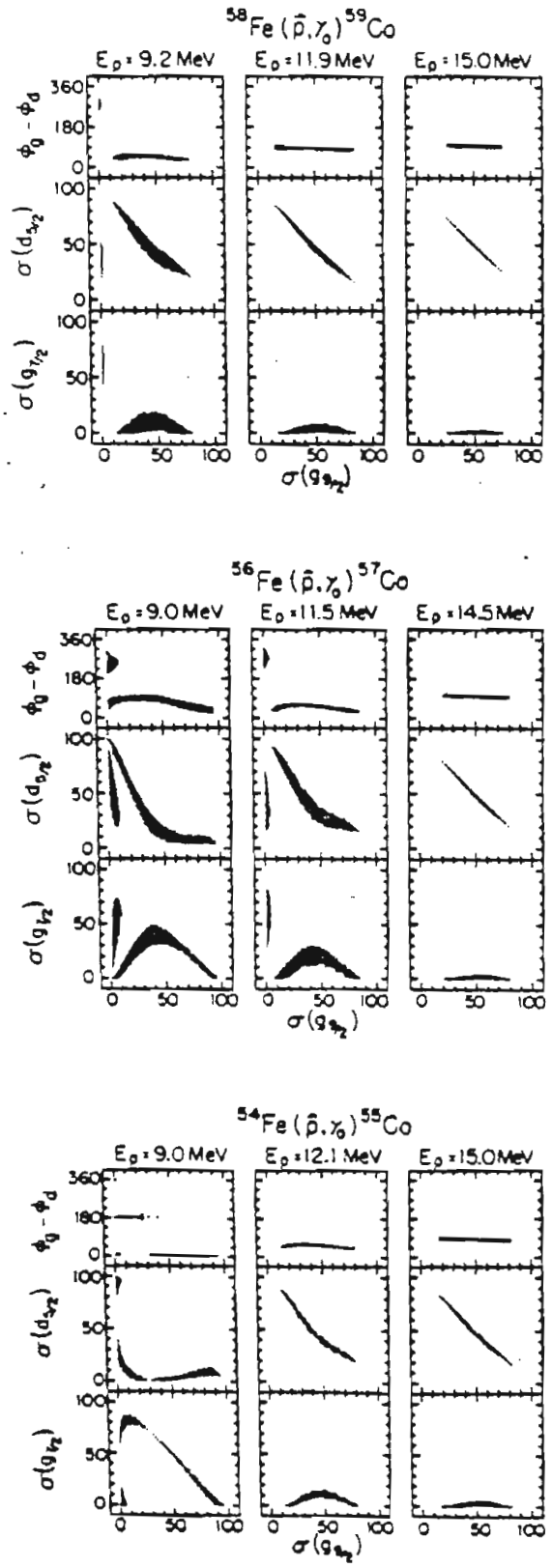

FIG. 7. The solutions at three representative energies for each of the three reactions studied. These solutions were obtained under the restriction that $\phi(g_{7/2}) - \phi(g_{9/2}) = 0°$.

chosen arbitrarily) and three equations, the solutions are rather ambiguous.

In order to obtain a more defined set of solutions we made use of the results of a recent study of elastic-proton scattering from ^{56}Fe with polarized protons[23] which indicated that the elastic phase

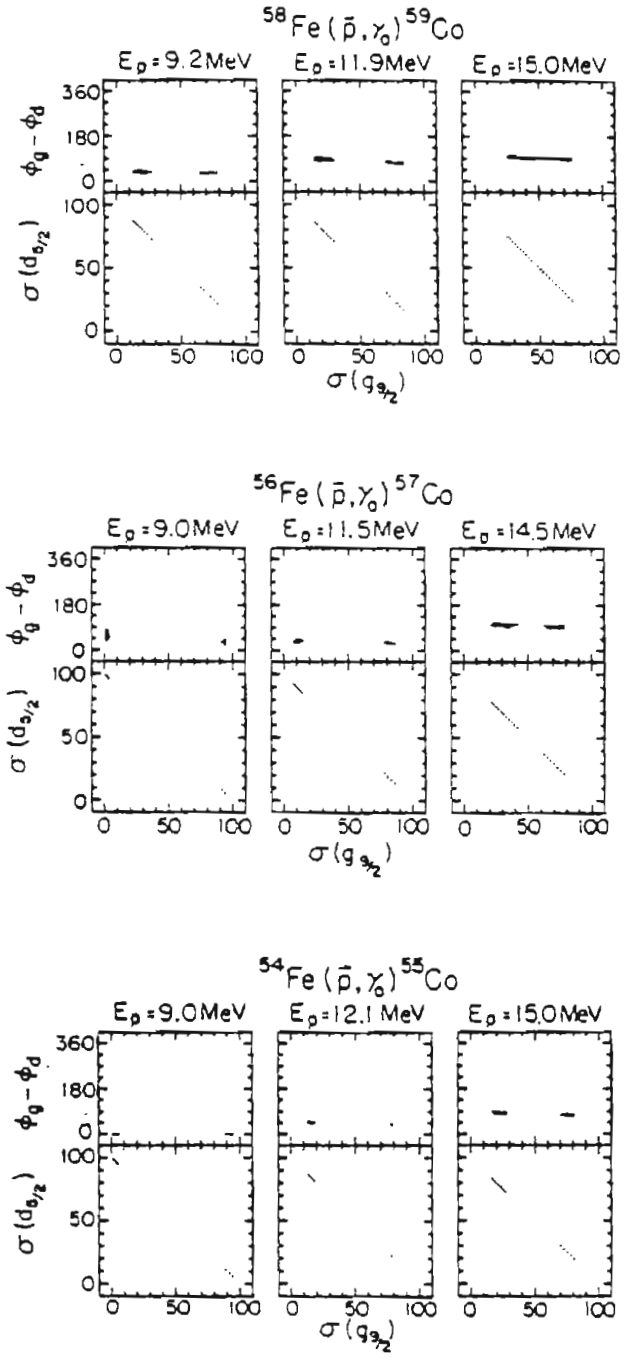

FIG. 8. The solutions at three representative energies for each of the three reactions studied. These solutions were obtained under the assumption that the $g_{7/2}$ amplitude was zero.

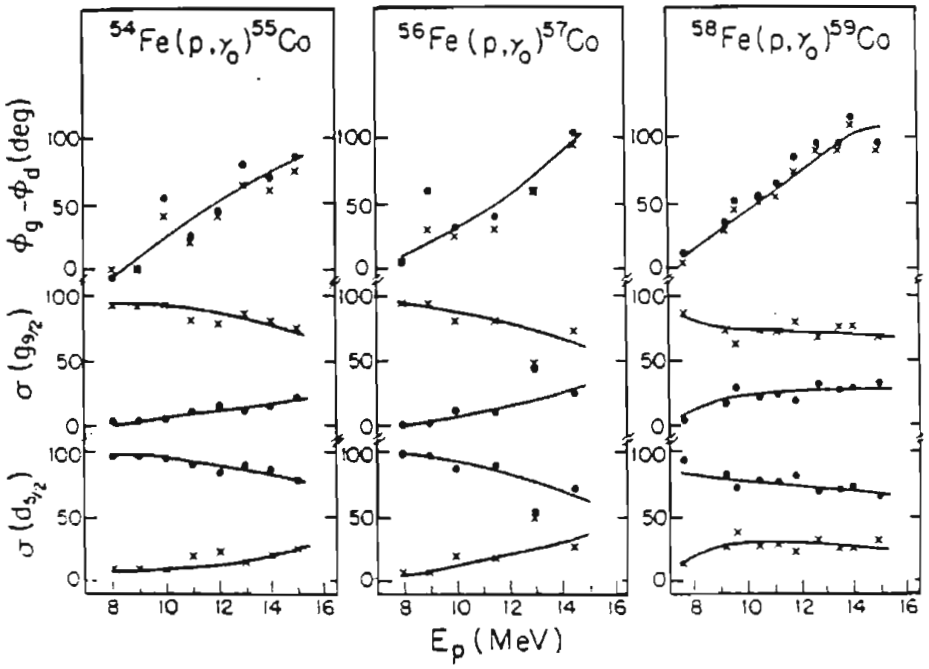

FIG. 9. A plot of the percent cross section due to each T-matrix element as a function of energy for each target studied. The relative d to g phase is also shown. These solutions were obtained under the assumption that the $g_{7/2}$ amplitude equaled zero (see Fig. 8). The solid lines are smooth curves drawn through the points which correspond to the solutions having the best χ^2 values.

shift difference between the $g_{7/2}$ and $g_{9/2}$ partial waves was less than 4° at the present energies. New solutions were then obtained with $\phi(g_{7/2}) - \phi(g_{9/2}) = 0$. For these latter searches, the amplitudes were incremented through 50 steps, and the phase difference $[\phi(d_{5/2}) - \phi(g_{9/2})]$ was stepped in increments of 5°. Results at three energies spanning the measured range are shown for each isotope in Fig. 7. With this phase restriction, we obtain a much more defined set of solutions. At the lower energies below the region of the main giant dipole resonance peak, two solutions are apparent; one in which the $g_{7/2}$ strength is dominant with little $g_{9/2}$ strength, and one in which there can be considerable $g_{9/2}$ strength. At the higher energies, only the latter solution is observed. At these higher energies (above 16.5 MeV excitation in ^{55}Co, 17.5 MeV in ^{57}Co, and 16.5 MeV in ^{59}Co), a maximum of 15% of the strength was found to be due to the $g_{7/2}$ amplitude, decreasing to less than 6% at the highest energies measured, while the d to g phase smoothly increased from about 45° to 90°. A simple 1p-2h shell model picture for a $\frac{7}{2}^+$ level would be a $(g_{7/2}, f_{7/2}^{-2})$ configuration, suggesting that, in the absence of appreciable mixing, this spin-flip transition would indeed be very weak.

The preceding results indicate that the $g_{7/2}$ T-matrix amplitude is small in the GDR of these Co isotopes in the (p,γ_0) reaction. If we set this amplitude to zero and again search for solutions which satisfy our experimentally determined coefficients, we obtain results such as those shown in Fig. 8. We now see that there are basically two solutions; one is predominantly $d_{5/2}$ while the other is predominantly $g_{9/2}$, with the phase differences being about the same for both solutions. These results are summarized in Fig. 9. The solutions shown correspond to the best χ^2 value, as defined above. The most dramatic change is seen in the relative phase between the $d_{5/2}$ and $g_{9/2}$ amplitudes which increases fairly smoothly from about 0° to about 95°. The amplitudes do not change dramatically, showing only somewhat more mixing at higher energies. At 13 MeV in ^{56}Fe+p, only one solution is found which contains approximately equal strengths for each amplitude. While one might suppose this to be a crossing of solutions, the relationship between phases (the relative phase for the predominantly $d_{5/2}$ solution is always larger than the relative phase for the predominantly $g_{9/2}$ solution) and the systematic behavior of ^{54}Fe+p and ^{58}Fe+p would seem to make this supposition unlikely. The results of this experiment would appear to imply that no significant change in configuration occurs as we pass through

the GDR. Although no direct evidence for isospin splitting has been observed in these nuclei, a picture in which the $T_>$ strength is centered somewhat above the $T_<$ strength, but in which the two strengths strongly overlap, cannot be ruled out.

The authors wish to thank Mr. G. Rochau for his help in obtaining and analyzing these data. We are also indebted to Dr. T. B. Clegg for his generous help and advice in operating the TUNL polarized ion source.

---

*Partially supported by the U.S. Energy Research and Development Administration.
†Partially supported by the Southern Regional Education Board and Research Corporation.
‡Partially supported by the National Science Foundation.

[1]J. V. Maher, L. Meyer-Schutzmeister, E. L. Sprenkel-Segel, D. von Ehrenstein, R. J. Nemanich, G. C. Klang, J. F. Tonn, and R. E. Segel, Phys. Rev. C 9, 1440 (1974).
[2]P. Paul, in *Proceedings of the International Conference on Photonuclear Reactions and Applications, Asilomar, 1973*, edited by B. L. Berman (Lawrence Livermore Laboratory, Univ. of California, 1973), p. 407; and references therein.
[3]E. M. Diener, J. F. Amann, P. Paul, and J. D. Vergados, Phys. Rev. C 7, 705 (1973).
[4]P. Paul, J. F. Amann, and K. A. Snover, Phys. Rev. Lett. 27, 1013 (1971).
[5]M. Hasinoff, G. A. Fisher, H. M. Knan, and S. S. Hanna, Phys. Lett. 30B, 337 (1969).
[6]D. F. Measday, A. B. Clegg, and P. S. Fisher, Nucl. Phys. 61, 269 (1965).
[7]M. Danos, Nucl. Phys. 5, 23 (1958).
[8]H. F. Glavish, S. S. Hanna, R. Avida, R. N. Boyd, C. C. Chang, and E. Diener, Phys. Rev. Lett. 28, 766 (1972); S. S. Hanna *et al.*, Phys. Lett. 40B, 631 (1972).
[9]H. R. Weller, N. R. Roberson, D. Rickel, C. P. Cameron, R. D. Ledford, and T. B. Clegg, Phys. Rev. Lett. 32, 177 (1974); Phys. Rev. C 13, 922 (1976).
[10]Oak Ridge National Laboratories, Isotopes Sales, Oak Ridge, Tennessee.
[11]J. Benveniste, A. C. Mitchell, and C. B. Fulmer, Phys. Rev. 133, B317 (1964).
[12]T. B. Clegg, G. A. Bissinger, W. Haeberli, and P. A. Quin, in *Polarization Phenomena in Nuclear Reactions*, edited by H. H. Barschall and W. Haeberli (Univ. of Wisconsin Press, Madison, 1970), p. 835.
[13]T. A. Trainor, T. B. Clegg, and P. W. Lisowski, Nucl. Phys. A220, 533 (1974).
[14]E. Hayward, B. F. Gibson, and J. S. O'Connell, Phys. Rev. C 5, 846 (1972).
[15]R. O. Akyuz and S. Fallieros, Phys. Rev. Lett. 27, 1016 (1971).
[16]R. Leonardi and E. Lipparini, Phys. Rev. C 11, 2073 (1975).
[17]A. Fallieros and B. Goulard, Nucl. Phys. A147, 593 (1970).
[18]Evans Hayward, in *Nuclear Structure and Electromagnetic Interactions*, edited by N. McDonald (Plenum, New York, 1965), p. 141.
[19]L. Nieseen and W. J. Huiskamp, Physica 57, 1 (1972).
[20]T. R. Fisher, A. R. Poletti, and B. A. Watson, Phys. Rev. C 8, 1837 (1973).
[21]E. M. Diener, J. F. Amann, P. Paul, and S. L. Blatt, Phys. Rev. C 3, 2303 (1971).
[22]B. L. Berman, At. Data Nucl. Data Tables 15, 345 (1975).
[23]H. R. Weller, J. Szucs, J. A. Kuehner, G. D. Jones, and D. T. Petty, Phys. Rev. C 13, 1055 (1976).

LIST OF REFERENCES

R. O. Akyuz and S. Fallieros, Phys. Rev. Lett. 27 (1971) 1016.

F. D. Becchetti, Jr. and G. W. Greenlees, Phys. Rev. 182 (1969) 1190.

P. R. Bevington, Data Reduction and Error Analysis for the Physical Sciences (McGraw Hill, Inc., 1969).

A. Bohr and B. R. Mottelson, Nuclear Structure, Vol. 2 (W. A. Benjamin, Inc., Reading, Mass., 1975).

F. R. Buskirk, Private Communication (1976)

T. B. Clegg, G. A. Bissenger, W. Haerberli, and P. A. Quin, Polarization Phenomena in Nuclear Reactions ed. H. H. Barschall and W. Haeberli, (Univ. of Wisconsin Press, Madison, Wis., 1970).

M. Danos, Nucl. Phys. 5 (1958) 23.

G. Dearnaley, D. S. Gemmell, B. W. Hooton, and G. A. Jones, Nucl. Phys. 64 (1965) 177.

A. Fallieros and B. Goulard, Nucl. Phys. A147 (1970) 593.

S. Fukuda and Y. Torizuka, Phys. Rev. Lett. 29 (1972) 1109.

R. W. Gellie, K. H. Lokan, and N. K. Sherman, Proceedings of the International Conference on Photonuclear Reactions and Applications, Asilomar, 1973 ed. B. L. Berman, (Lawrence Livermore Laboratory, Univ. of California, 1973) 171.

M. Gell-Mann and V. L. Telegdi, Phys. Rev. 91 (1953) 169.

H. F. Glavish, Proceedings of the Fifth Symposium on the Structure of Low-medium Mass Nuclei, 1972 ed. J. P. Davidson and B. D. Kern, (The University Press Of Kentucky, Lexington, Kentucky, 1973) 233.

H. F. Glavish, J. R. Calarco, S. S. Hanna, E. Kuhlmann, and D. G. Mavis, unpublished progress report, Physics Department, Stanford University, (1974) 41.

H. F. Glavish, S. S. Hanna, R. Avida, R. N. Boyd, C. C. Chang, and E. Diener, Phys. Rev. Lett. 28 (1972) 766.

S. S. Hanna, H. F. Glavish, R. Avida, J. R. Calarco, E. Kuhlmann, and R. LaCanna, Phys. Rev. Lett. 32 (1974) 114.

S. S. Hanna, H. F. Glavish, E. M. Diener, J. R. Calarco, C. C. Chang, R. Avida, and R. N. Boyd, Phys. Lett. 40B (1972) 631.

O. Hausser, T. K. Alexander, A. B. McDonald, and W. T. Diamond, Nucl. Phys. A175 (1971) 593.

E. Hayward, Nat. Bur. Stand. (U.S.) Monograph, 1970.

R. A. Hilko, unpublished Ph.D. thesis, Duke University, 1974.

A. Kiss, C. Mayer-Boricke, M. Pogge, P. Turek, and S. Wiktor, Phys. Rev. Lett. 37 (1976) 1188.

R. D. Ledford, unpublished Ph.D. thesis, Duke University, 1976.

M. B. Lewis and F. E. Bertrand, Nucl. Phys. A196 (1972) 337.

J. V. Maher, L. Meyer-Schutzmeister, E. L. Sprenkel-Segel, D. von Ehrenstein, R. I. Nemanich, G. C. Kiang, J. F. Tonn, and R. E. Segel, Phys. Rev. C9 (1974) 1440.

F. B. Malik and M. G. Mustafa, Proceedings of the Fifth Symposium on the Structure of Low-medium Mass Nuclei, 1972 ed. J. P. Davidson and P. D. Kern, (The University Press Of Kentucky, Lexington, Kentucky, 1973) 124.

R. E. Mans, E. G. Adelberger, K. A. Snover, and M. D. Cooper, Phys. Rev. Lett. 35 (1975) 202.

R. C. McBroom, unpublished Ph.D. thesis, University of Florida, 1977.

L. Meyer-Schutzmeister, Z. Vager, R. E. Segel, and P. P. Singh, Nucl. Phys. A108 (1968) 180.

M. Nagao and Y. Torizuka, Phys. Rev. Lett. 30 (1972) 1068.

D. A. Outlaw, G. E. Mitchell, and E. G. Bilpuch, Nucl. Phys. A269 (1967) 99.

P. Paul, Proceedings of the International Conference on Photonuclear Reactions and Applications, Asilomar, 1973 ed. B. L. Berman, (Lawrence Livermore Laboratory, Univ. of California, 1973) 407.

C. M. Perey and F. G. Perey, Atom. Data Nucl. Data Tables 13 (1974) 293.

F. O. Purser, H. W. Newson, N. R. Roberson, E. G. Bilpuch, and R. L. Walter, Fifth International Cyclotron Conference ed. R. W. Mellray, (1969) 13.

H. H. Rosenbrock, Comput. J. 3 (1960) 175.

D. G. Rickel, C. P. Cameron, P. D. Ledford, N. R. Roberson, H. P. Weller, and D. R. Tilley, Phys. Rev. C14 (1976) 338.

P. P. Singh, R. E. Segel, L. Meyer-Schutzmeister, S. S. Hanna, and R. G. Allas, Nucl. Phys. 65 (1965) 577.

K. A. Snover, K. Ebisawa, D. R. Brown, and P. Paul, Phys. Rev. Lett. 32 (1974) 317.

M. Suffert, W. Feldman, J. Mahieux, and S. S. Hanna, Nucl. Inst. and Methods 63 (1968) 1.

T. A. Trainor, T. B. Clegg, P. W. Lisowski, A220 (1974) 533.

H. R. Weller, R. A. Blue, N. R. Roberson, D. G. Rickel, S. Maripuu, C. P. Cameron, P. D. Ledford, and D. R. Tilley, Phys. Rev. C13 (1976) 922.

H. R. Weller, N. R. Roberson, D. Rickel, C. P. Cameron, R. D. Ledford, and T. B. Clegg, Phys. Rev. Lett. 32 (1974) 177.

D. H. Youngblood, J. M. Moss, C. M. Rozsa, J. D. Bronson, A. D. Bacher, and D. R. Brown, Phys. Rev. C13 (1976) 994.

BIOGRAPHY

CHRISTOPHER PAUL CAMERON

PERSONAL: Born May 5, 1950, Boston, Massachusetts
Single

EDUCATION: B. S. in Physics
Alma College (1972)

POSITION: Research Assistant, Duke University (1972)
Teaching Assistant, Duke University (1972-1973)
Research Assistant, Duke University (1973-1977)

MEMBERSHIPS: Omicron Delta Kappa, American Physical Society

PUBLICATIONS:

1. A Position-Sensitive Proportional-Counter For Use in the Enge Split-Pole Spectrograph (with L. R. Greenwood, J. C. Stolzfus, K. Katori, and T. H. Braid) Argonne National Laboratory Physics Division, Informal Report PHY-1972B.

2. Evidence for E2 and M1 Radiation in the Giant-Dipole-Resonance Region of ^{15}N (with H. R. Weller, N. R. Roberson, D. G. Rickel, R. D. Ledford, and T. B. Clegg) Phys. Rev. Lett. 32 (1974) 177.

3. Measurements of γ-ray Angular Distributions and Linear Polarizations in ^{48}V (with D. G. Rickel, N. R. Roberson, R. D. Ledford, S. G. Buccino, and D. R. Tilley) Nucl. Phys. A256 (1976) 152.

4. Mean Lifetimes in ^{55}Co (with R. O. Nelson, J. R. Williams, D. R. Tilley, D. G. Rickel, N. R. Roberson, S. Maripuu, and R. D. Ledford) Nucl. Phys. A261 (1976) 427.

5. Giant Resonance Region of ^{15}N Studied by Polarized and Unpolarized Proton Capture Measurements (with H. R. Weller, R. A. Blue, N. R. Roberson, D. G. Rickel, S. Maripuu, R. D. Ledford, and D. R. Tilley) Phys. Rev. C13 (1976) 922.

6. Comment on "E1 Excitations in A=15 Nuclei" (with H. R. Weller, N. R. Roberson, D. G. Rickel, R. D. Ledford, and D. R. Tilley) Phys. Rev. C13 (1976) 2062.

7. The Giant Dipole Resonance Region in ^{56}Fe Observed via (p,γ_0) and (α,γ_0) Reactions (with D. G. Rickel, R. D. Ledford, N. R. Roberson, H. R. Weller, and D. R. Tilley) Phys. Rev. C14 (1976) 553.

8. The Giant Dipole Resonances in $^{55, 57, 59}Co$ Using Polarized Proton Capture (with N. R. Roberson, D. G. Rickel, R. D. Ledford, H. R. Weller, R. A. Blue, and D. R. Tilley) Phys. Rev. C14 (1976) 553.

9. Polarized Beam Angular Correlation Measurements in ^{41}Ca (with C. R. Gould, D. R. Tilley, R. D. Ledford, N. R. Roberson, and T. B. Clegg) Proceedings of the Fourth International Symposium on Polarization Phenomena in Nuclear Reactions, ed. W. Gruebler and V. Konig (Birkhauser Verlag Basel und Stuttgart, Switzerland, 1976) 807.

10. A Study of the Giant Dipole Resonance Region in Co Isotopes Using Polarized Proton Capture Measurements (with H. R. Weller, R. A. Blue, G. Rochau, R. McBroom, N. R. Roberson, D. G. Rickel, and R. D. Ledford) Proceedings of the Fourth International Symposium on Polarization Phenomena in Nuclear Reactions, ed. W. Gruebler and V. Konig (Birkhauser Verlag Basel und Stuttgart, Switzerland, 1976) 757.

11. A Study of the Giant Resonance Region of ^{55}Co, ^{57}Co, and ^{59}Co Using Polarized Proton Capture and Elastic Scattering Measurements (with H. R. Weller, N. R. Roberson, D. G. Rickel, R. D. Ledford, D. R. Tilley, J. Szucs, J. A. Kuehner, G. D. Jones, and D. T. Petty) Proceedings of the Symposium on Nuclear Structure: Coexistence of Single Particle and Collective Type Excitation, Balatonfrued, Hungary, 1975. To be published.

ABSTRACTS:

1. Evidence for E2 and M1 Radiation in the Giant Dipole Resonance Region of ^{15}N (with N. R. Roberson, D. G. Rickel, R. D. Ledford, T. B. Clegg, and H. R. Weller) Bull. Am. Phys. 18 (1973) 1387.

2. Study of Giant Dipole Resonances in the Co Isotopes Using Proton Capture and Polarized Proton Capture Measurements (with H. R. Weller, R. A. Blue, D. Griggs, N. R. Roberson, D. G. Rickel, R. D. Ledford, J. D. Turner, and D. R. Tilley) Bull. Am. Phys. Soc. 19 (1974) 988.

3. The Giant Resonance Region of ^{56}Fe from (p,γ_0) and (α,γ_0) Reactions (with D. G. Rickel, N. R. Roberson, R. D. Ledford, D. R. Tilley, H. R. Weller, and R. A. Blue) Bull. Am. Phys. Soc. 20 (1975) 1156.

4. The Giant Dipole Resonance of ^{31}P (with R. D. Ledford, D. G. Rickel, J. D. Turner, N. R. Roberson, D. R. Tilley, R. D. Ledford, D. G. Rickel, J. D. Turner, N. R. Roberson, D. R. Tilley, R. C. McBroom, R. A. Blue, and H. R. Weller) Bull. Am. Phys. Soc. 21 (1976) 556.

5. Investigations of the $3/2^+$ Analogue State in ^{89}Y at E_x =14.62 MeV using the $^{88}Sr(p,\ )^{89}Y$ Reaction (with R. D. Ledford, D. G. Rickel, J. D. Turner, N. R. Roberson, D. R. Tilley, R. McBroom, and H. R. Weller) Bull. Am. Phys. Soc. 21 (1976) 581.

6. Study of the Giant Dipole Resonance Region of ^{89}Y (with N. R. Roberson, R. D. Ledford, D. G. Rickel, J. D. Turner, D. R. Tilley, R. McBroom, and H. R. Weller, Bull. Am. Phys. Soc. 21 (1976) 516.

7. The $^3H(p,\gamma_0)^4He$ Reaction for $17 \leq E \leq 30$ MeV (with R. McBroom, H. R. Weller, N. R. Roberson, D. G. Rickel, J. D. Turner, R. D. Ledford, and D. R. Tilley) Bull. Am. Phys. Soc. 21 (1976) 534.

8. Search for Collective Resonances Above the Giant Dipole Resonance (with R. D. Ledford, J. D. Turner, N. R. Roberson, H. R. Weller, R. A. Blue, R. McBroom, and D. R. Tilley) Bull. Am. Phys. Soc. 21 (1976) 996.

9. Evidence for $J^{\pi}=2^{+}$ States in ^{4}He (with R. McBroom, H. R. Weller, N. R. Roberson, J. D. Turner, R. D. Ledford, and D. R. Tilley, Bull. Am. Phys. Soc. 21 (1976) 997.